

Seismological Indicators of Geologically Inferred Fault Maturity

Huiyun Guo¹, Thorne Lay¹, and Emily E Brodsky²

¹University of California Santa Cruz

²University of California, Santa Cruz

December 7, 2022

Abstract

Variations in fault maturity have intermittently been invoked to explain variations in some seismological observations for large earthquakes. However, the lack of a unified geological definition of fault maturity makes quantitative assessment of its importance difficult. We evaluate the degree of empirical correlation between field measurements indicative of fault zone maturity and remotely measured seismological source parameters of 34 large shallow strike-slip events. Metrics based on fault segmentation, such as number of primary rupture segments and surface rupture azimuth, correlate best with seismic source attributes and the correlations with cumulative fault slip are somewhat weaker. Average rupture velocity shows the strongest correlation with metrics of maturity, followed by relative aftershock productivity. Mature faults have relatively lower aftershock productivity and higher rupture velocity. A more complex relation is found with moment-scaled radiated energy. There appears to be distinct behavior of very immature events with no prior mapped fault and < 1 km cumulative slip, which radiate modest seismic energy, while moderately mature faults have events with higher moment-scaled radiated energy and very mature faults with increasing cumulative slip tend to have events with reducing moment-scaled radiated energy. We also explore qualitative and composite assessments of maturity and arrive at similar trends. This empirical approach establishes that there are relationships between remote seismological observations and fault system maturity that can help to understand variations in seismic hazard among different fault environments and to assess the relative maturity of blind fault systems for which direct observations of maturity are very limited.

Hosted file

essoar.10512874.1.docx available at <https://authorea.com/users/564077/articles/611075-seismological-indicators-of-geologically-inferred-fault-maturity>

Seismological Indicators of Geologically Inferred Fault Maturity

Huiyun Guo¹, Thorne Lay¹, and Emily E. Brodsky¹

¹*Department of Earth and Planetary Sciences, University of California Santa Cruz, Santa Cruz, CA, USA 95064.*

Correspondence to: H. Guo (hguo23@ucsc.edu)

Key Points:

- Strike-slip fault zone relative maturity is inferred from cumulative fault slip and from individual event surface rupture segment geometry.
- Maturity measures are compared with relative aftershock productivity, rupture velocity, and moment-scaled radiated energy.
- Less mature faults have higher relative aftershock productivity and lower rupture velocity than mature faults.
- Moment-scaled radiated energy is low for very new faults, increases with modest maturation, and then decreases for very mature faults.

Abstract

Variations in fault maturity have intermittently been invoked to explain variations in some seismological observations for large earthquakes. However, the lack of a unified geological definition of fault maturity makes quantitative assessment of its importance difficult. We evaluate the degree of empirical correlation between field measurements indicative of fault zone maturity and remotely measured seismological source parameters of 34 large shallow strike-slip events. Metrics based on fault segmentation, such as number of primary rupture segments and surface rupture azimuth, correlate best with seismic source attributes and the correlations with cumulative fault slip are somewhat weaker. Average rupture velocity shows the strongest correlation with metrics of maturity, followed by relative aftershock productivity. Mature faults have relatively lower aftershock productivity and higher rupture velocity. A more complex relation is found with moment-scaled radiated energy. There appears to be distinct behavior of very immature events with no prior mapped fault and < 1 km cumulative slip, which radiate modest seismic energy, while moderately mature faults have events with higher moment-scaled radiated energy and very mature faults with increasing cumulative slip tend to have events with reducing moment-scaled radiated energy. We also explore qualitative and composite assessments of maturity and arrive at similar trends. This empirical approach establishes that there are relationships between remote seismological observations and fault system maturity that can help to understand variations in seismic hazard among different fault environments and to assess the relative maturity of blind fault systems for which direct observations of maturity are very limited.

Plain Language Summary

Faults evolve from irregular fracture networks that progressively localize and accumulate slip on growing segments with increasing total fault displacement. Roughness of the boundary smooths with accumulating slip and gouge and damage zones accumulate. Fault zone maturity is an assessment of where a fault zone lies in this process. Earthquakes occurring on evolving faults are influenced by the geological features, and it is plausible that seismological attributes of individual large events may be indicative of the degree of maturation of the fault system. This is tested by empirical comparison of geological and geometrical aspects of strike-slip fault zones and surface ruptures of large events on them with seismological attributes of the events. While there is no agreed upon measure of fault zone maturity, we consider cumulative slip of shallow strike-slip faults and field observations of number of fault segments, step-over offsets between segments, and changes in angle between segments for a given rupture as maturity indicators. These are compared with relative aftershock productivity, rupture velocity, and moment-scaled radiated energy measures that can be made for all large earthquakes. Less mature faults have higher relative aftershock productivity and lower rupture velocity. Radiated energy is relatively low for newly forming faults, increases with modest cumulative slip and then decreases as maturity further increases. These relationships help elucidate seismic hazard for fault systems of different maturity and can indicate maturity for fault systems not exposed at the surface.

1. Introduction

Understanding how earthquake dynamic rupture process is affected by complex fault geometry and distinguishing this from frictional complexity and rheological properties of the fault is an important frontier in earthquake science (e.g., Klinger et al., 2018; Thomas et al., 2017; Wibberley et al., 2008). The complexity of the fault geometry reflects whether the fault network is mature or immature in terms of structural evolution. The structural maturity of the fault zone has been related to the seismic activity rate inferred from modern, historical and ancient seismic data (e.g., Cowan et al., 1996; Wesnousky, 1988; Wibberley et al., 2008) and plausibly may have significant impact on individual earthquake characteristics, such as the distribution of slip, rupture velocity, and number of ruptured segments (Perrin et al., 2021). Mature fault zones in strike-slip tectonic settings may serve as highly anisotropic permeability channels through the brittle crust making some regions more likely to produce slow events than immature fault zones (Thakur et al., 2020), while immature fault zones may exhibit more complex ruptures and distributed coseismic damage that can be observed seismologically.

Surface rupturing events provide important, albeit incomplete, characterizations of the fault systems producing large earthquakes for which seismic source parameters can be determined. For example, the 2019 M_W 7.1 Ridgecrest earthquake involved an immature surface-rupturing fault system with small cumulative slip (< 70 m) and multiple segments that could be mapped in the field at many

scales (e.g., DuRoss et al., 2020; Hudnut et al., 2020; Rodriguez-Padilla et al., 2022). Various seismic source attributes of the 2019 Ridgecrest mainshock have also been determined, indicating overall slow average rupture velocity, low moment-scaled radiated seismic energy, and relatively high aftershock productivity (e.g., Goldberg et al., 2020; Liu et al., 2019; Ross et al., 2019). These seismological characteristics contrast with the rupture of mature, large cumulative slip faults, such as those that produced the Kunlun (Tibet) earthquake in 2001 and the Denali (Alaska) earthquake in 2002. The latter ruptures include long, well-localized faults with high rupture velocity, including intervals of supershear rupture (Bhat et al., 2007; Bouchon & Vallée, 2003; Dunham & Archuleta, 2004; Perrin, Manighetti, Ampuero, et al., 2016; Vallée & Dunham, 2012; Walker & Shearer, 2009; Wang, Mori, et al., 2016), low aftershock productivity (especially in the supershear regions, e.g., Bouchon & Karabulut, 2008), and relatively high moment-scaled radiated energy overall.

Fault maturity is variably defined on different scales and may relate to the evolution of the fault core, the damage zone and the shear deformation zone, which reflect the regions controlled by wear processes (Perrin et al., 2021). A qualitative definition of fault maturity can also be the degree of evolution of its macroscopic structural properties, which may be related to the fault age, slip rate, and total accumulated slip, as adopted in various studies (Dolan & Haravitch, 2014; Manighetti et al., 2007; Perrin, Manighetti, Ampuero, et al., 2016). In this study, our usage refers to the general tendency for fault systems to evolve from complex fracture systems into localized through-going faults as displacement accumulates. Evolving faults intrinsically have variable amounts of slip, and hence maturity, along their length, being most mature near the middle of the fault length and least mature at the ends (e.g., Perrin et al., 2016); no single measure of maturity is valid over the entire fault. Persistence of fault segmentation even for large cumulative displacements may reflect controls of crustal thickness and geological structures that compete with the tendency to progressively localize onto a single surface (e.g., Klinger, 2010; Jiao et al., 2021). Thus, maturation is not self-evidently linear with time or cumulative slip. Broadening of damage zones around faults may saturate at relatively modest displacements (e.g., Savage & Brodsky, 2011). Related tendencies to have or lack shallow slip deficit and afterslip may indicate varying degrees of fault maturity (e.g., Li et al., 2020), but surficial sediments may obscure the degree of deeper localization for a wide range of fault maturity.

In this study, we explore the extent to which remotely observable source parameters of large shallow strike-slip earthquakes, specifically relative aftershock productivity, rupture velocity, and moment-scaled radiated elastic energy, are influenced by and indicative of the maturity of the fault system that hosted the event. We focus on shallow continental strike-slip faults with well-documented context and assemble data on several geological candidate metrics for measuring maturity: cumulative displacement, segment number, azimuth change and stepover offset. We then compare the correlation between each of these geological and geometric variables to the seismological ones for both the full dataset and

subsets with the most robust geological data. After identifying some preliminary trends, we then explore the power of a more heuristic assessment of maturity as well as a composite measure. In the end, we conclude that some seismological variables, such as rupture velocity and to a lesser degree aftershock productivity, are correlated with maturity metrics that include information about segmentation, especially number of segments or azimuth change. Seismic radiated energy has a more complex and potentially non-monotonic relationship to maturity.

2. Data

Continental earthquakes provide geological information that can not be as well observed for oceanic earthquakes. Specifically, shallow continental earthquakes with magnitudes larger than 6 are often quantitatively characterized by geological and seismological studies. Shallow crustal strike-slip earthquakes in particular provide field and geophysical observations that allow the maturity of the associated fault system to be evaluated. Detailed studies of continental strike-slip events with $M_W \geq 6.0$ over the past few decades provide multiple examples of ruptures with well-determined source parameters in tandem with an observational field study basis for evaluating the maturity of their fault system. For example, the segmented rupture determined for the $M_W 6.5$ Idaho earthquake in 2020 occurred on immature faults that were not previously mapped and lack large cumulative displacement (Yang et al., 2021). Recognizing the challenge of defining and measuring fault maturity with the available data, we assembled summary fault zone properties for regions hosting recorded large ($M_W \geq 6.0$) shallow strike-slip earthquakes to provide a preliminary basis for defining relative maturity. In total, we select the 34 strike-slip earthquakes shown in Figure 1. Except for the Ridgecrest sequence, which includes both the $M_W 6.4$ foreshock and the $M_W 7.1$ mainshock, all other utilized earthquakes are single events.

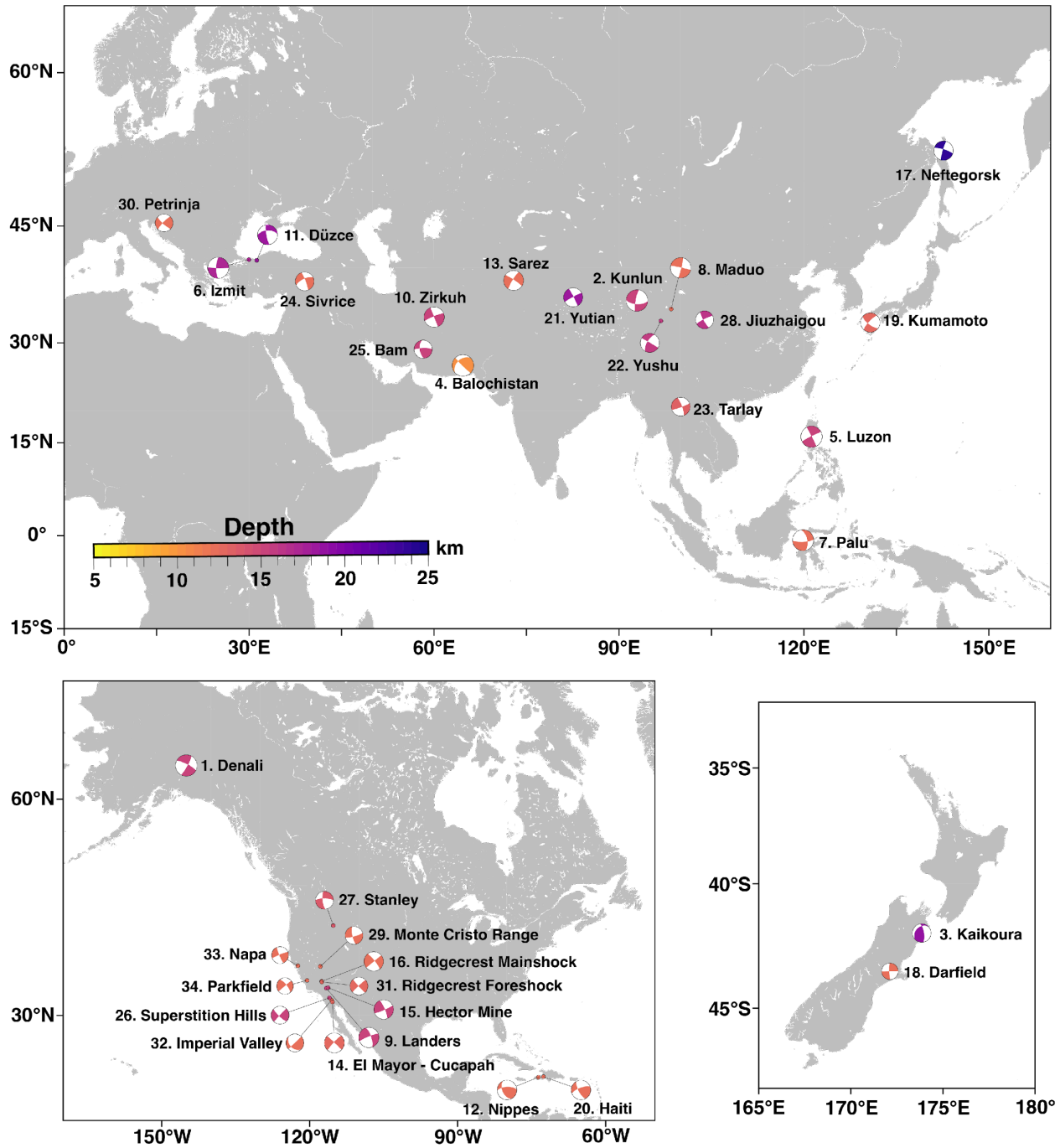


Figure 1. Maps showing locations and focal mechanisms of the 34 selected shallow strike-slip earthquakes, with the focal mechanisms color-coded by hypocen-

tral depth. Events are sorted by magnitude and labeled with numbers used as their event ID (Table 1) in the following discussion.

2.1 Geological and Geometric Measurements

Maturity is a qualitative property of fault systems and a basic challenge for this study is to establish field-based attributes of fault systems that provide a consistent assessment of relative maturity. The properties considered in this study include the total slip along the fault and segmentation related measurements (Figure 2).

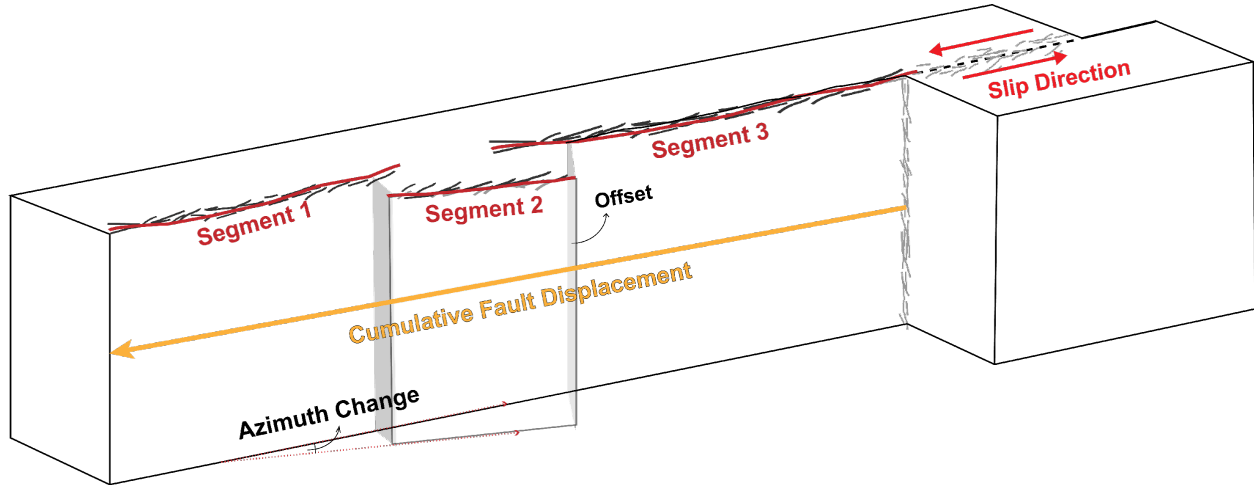


Figure 2. Schematic model of some geologic field measurements for a surface-rupturing fault, including cumulative fault displacement and fault segmentation related parameters such as number of primary segments and surface stepover offsets between segments.

2.1.1 Slip-based measures of maturity

A key issue for maturity is total slip of the fault involved in a particular rupture, related to both the slip rate and the fault age. If the fault has large cumulative displacement (from hundreds to thousands of kilometers), it can be considered overall mature, in terms of localization, gouge accumulation, etc., but maturity varies along the fault, so local properties where a rupture occurs are also important. Immature faults have small cumulative displacement (from hundreds of meters to a few tens of kilometers). We compile estimates of cumulative fault displacement in the literature for each of the faults in our study; these sometimes span a large range for a given fault due to observational limitations (Table 1).

Another potential candidate metric of maturity is the ratio of surface slip to slip at depth on a fault. Surface fault slip during earthquakes is often smaller than the slip at depth determined from geodetic and seismologic data (e.g., Thatcher & Bonilla, 1989; Xu et al., 2016; Liu et al., 2021). Recent studies show

that the zone of maximum co-seismic slip in continental strike-slip earthquakes commonly occurs at about 3–6 km depth while the surface coseismic slip is often lower and afterslip and distributed deformation often do not add up to match the deep slip. Li et al. (2020) argue that a shallow slip deficit and lack of early afterslip indicates that the fault system is immature. We then expect a complex rupture geometry with distributed coseismic failure in the uppermost part of the brittle crust during the fault zone development. As faults mature, they straighten, develop a localized fault zone core, and the shallow slip deficit tends to diminish. Fault structural maturity and the percentage of total surface displacement that occurs on narrow zones of surface rupture relative to more distributed deformation have been revealed to have a consistent correlation (Dolan & Haravitch, 2014). Specifically, structurally immature fault zones (~ 25 km of total displacement) have lower percentage of the total surface deformation in earthquakes than mature faults. Although shallow slip deficit is potentially a useful factor for assessing maturity, the common lack of slip measurements and dependence on the estimates of slip at depth make it hard to quantify this property. Therefore, shallow slip deficit is ultimately not utilized in our set of geological measurements for all events, but it can provide extra assessment for some events when the data constraints are suitable.

2.1.2 Segmentation-based measures of maturity

Geological faults are segmented at large scale, and this is a property independent of the slip mode (Manighetti et al., 2007; 2021). As a fault grows with time, linkage between its large-scale segments increases and the geometry of the fault zone simplifies and becomes more continuous. The inter-segment zones commonly involve distributed, disorganized, secondary fissuring and faulting and therefore, can have higher overall strength on young, immature faults, and lower strength on mature features (Ben-Zion & Sammis, 2003). Earthquake ruptures on mature faults have been observed to have the ability to overcome the resistance of large scale stepovers while for immature faults, it is relatively harder for the earthquake to propagate across the disorganized, high-strength inter-segment zones (e.g., Gong et al., 2022; King & Nábělek, 1985; Liu et al., 2019; Sibson, 1985). Advances in fault mapping techniques have provided increasing details and more reliable rupture models, helping to characterize recent large earthquakes for the coseismic time-varying slip distribution of multiple fault segments involved in each rupture. For example, the 2019 Ridgecrest strike-slip earthquake sequence is a component of a developing large-scale fault system in the Eastern California shear zone (Goldberg et al., 2020; Liu et al., 2019; Ross et al., 2019; Shelly, 2020 and many others). The field attributes determined for the Ridgecrest mainshock indicate the rupture of a highly segmented immature fault zone that is not yet strongly localized. The degree of small-scale segmentation may influence seismological properties due to high fracture energy consumption, imposing slow average rupture velocity due to rupture hiatus as stepovers are negotiated, and high number of aftershocks due to stress concentration near segment transitions.

We therefore compile observations of field observations of surface ruptures in the

literature for each of the events in our study using multiple metrics based on segmentation (Figure 2). For instance, strike azimuth changes and stepovers are common features used to define segment boundaries along strike-slip ruptures (Bilham & Williams, 1985). Minor variation in the fault azimuth can produce significant rupture limitations while small stepovers of up to several kilometers do not necessarily prevent through-going rupture whereas stepovers larger than 5 km often do (Wesnousky, 1988; King et al., 2005; Klinger, 2010). In addition, the total number of segments is potentially an important aggregate measure of maturity.

Segmentation measures are, however, challenging to evaluate as the observed rupture must be long enough to capture the general features of the fault segmentation during an earthquake rupture without being biased by multiple segments located at the ends of the rupture (Klinger, 2010). Detailed and accurate rupture mapping is needed for resolution of the degree of segmentation. Our selected events are all large continental strike-slip events, most of which have well-documented surface ruptures. However, reported segmentation measures vary for each event due to different strategies in field mapping and counting of fault segments on a variety of scales.

A semi-automatic procedure with uniform criteria and scale can provide additional self-consistent segmentation measures to supplement our compiled results from prior studies. Therefore, we use a dataset compiled by Natural Hazards Risk and Resiliency Research Center (NHR3) that contains the digitized primary surface rupture of 21 earthquakes among our selected 34 events. The Sarez earthquake (earthquake ID13 in Figure 1) is an additional large earthquake that occurred in recent years and has well mapped surface rupture traces. We include this earthquake together with the 21 events from NHR3 to perform a systematic segmentation analysis to provide self-consistent constraints on segmentation of these local fault systems.

We follow the segmentation method described in Klinger (2010) to parameterize the earthquake surface rupture. This method is based on an l_1 trend filtering which performs a piecewise linear fit achieved by minimizing the equation, $\frac{1}{2} \sum_{i=1}^n (y_i - x_i)^2 + \lambda \sum_{i=2}^{n-1} |x_{i-1} - 2x_i + x_{i+1}|$, where y represents the data, x represents the model and n is the number of points. We follow the same strategy as Klinger (2010) by consistently resampling the surface rupture data to 1pt/100m to smooth the data to avoid biases caused by local minor wiggles and secondary strands along the rupture trace. This method is sensitive to fault azimuth changes and therefore can be a robust and useful tool in large-scale fault segmentation. The parameter λ controls the smoothness of the model and therefore affects the fit error between the data and model and the number of segments determined. Figure 3 shows the suite of possible combinations of RMS-misfit and number of segments with each point on this graph corresponding to a different choice of λ . The RMS-misfit drops drastically when the number of segments is lower than a threshold, therefore we select the preferred segment number as the minimum number of segments for which misfit no longer drops rapidly. As

a secondary criterion, we also consider a direct manual count from the rupture maps and verify that the semi-automatic method is consistent with visual inspection of the map (See Figures S1-S22 for direct visualization of the maps). The estimated number of segments is only for the main surface rupture while distributed ruptures or minor branches are not considered, so the segmentation measure is intrinsically a conservative one. Figures S1-S22 only present one possible realization of this semi-automatic segmentation method corresponding to the chosen l_1 . As Klinger (2010) points out, the specific segmentation is not unique, and we include uncertainty estimates on the number of segments.

We also use the segmentation on the NHR3 maps (Figures S1-S22) to determine maximum azimuth change and segment offset. Once again, we compare the results to published values in the literature for the specific earthquake where possible and report the full range of estimates as the range of possible values for the parameter in Table 1.

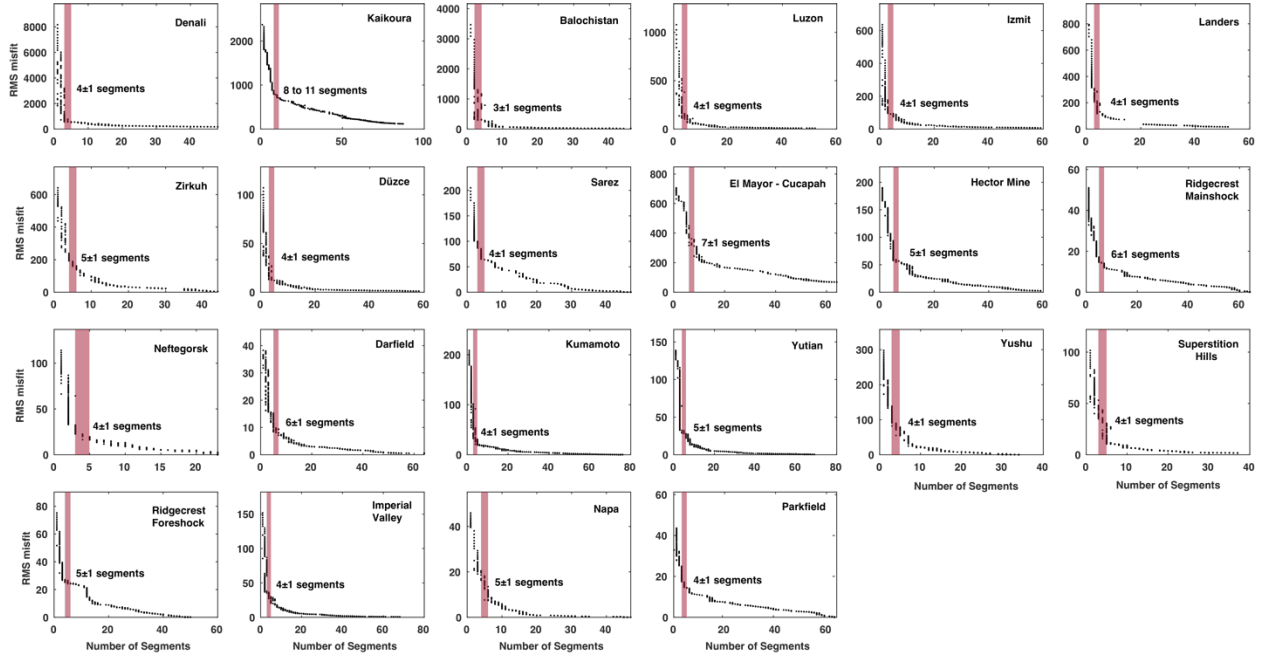


Figure 3. The l_1 trend filtering analyses for events with digitized surface rupture data. The number of segments listed in the figure is determined from the main surface rupture following the systematic segmentation method, and distributed branches are not counted. Figures S1-S22 present the final parameterizations for the number of segments for each event.

2.2 Seismic Source Attributes

Prior studies have suggested that geophysically determined earthquake characteristics, such as rupture velocity, stress drop, ground motion amplitude, and

slip distribution may be related to structural maturity of the local fault system (e.g., Dolan & Haravitch, 2014; Perrin et al., 2021; Stirling et al., 1996). We usually cannot robustly analyze the structural complexity of a blind fault but seismic source characteristics can be determined if it experiences a large earthquake. Seismology and geodesy now provide systematic characterizations of faulting for large earthquakes around the world, a subset of which do rupture the surface in fault zones for which we can estimate overall fault maturity. If we can establish relationships between the observed maturity of a fault and the seismic source attributes of earthquakes that rupture it, this would contribute to understanding variations in seismic hazard among different fault environments and could provide a probe of maturity of blind fault systems that are not exposed at the surface and cannot otherwise be characterized.

Among the 34 events in this study, only two well-studied and documented earthquakes, the 1979 Imperial Valley earthquake and the 1987 Superstition Hills earthquake, occurred earlier than 1990. We focus on events after 1990 because they have both more extensive field investigations and higher completeness of the main seismic parameter attributes that we consider: relative aftershock productivity, rupture velocity, and moment-scaled radiated elastic wave energy.

2.2.1 Aftershock Productivity

Aftershock productivity adjusted for scaling relative to mainshock magnitude has been related to both geological setting and focal mechanism (Dascher-Cousineau et al., 2020; Page et al., 2016; Tahir et al., 2012; Wetzler et al., 2016) and provides a measure of the distributed deformational process associated with an earthquake. For continental strike-slip events at shallow depth, we explore whether variability in aftershock productivity is influenced by fault zone maturity.

We use the ratio between the observed and predicted aftershock productivity as a readily measurable source parameter. Considering the variation in the completeness of magnitude for catalogs in different regions, the observed aftershock productivity (NA_{obs}) for each selected earthquake is determined using a fixed 45-day time window for aftershocks with magnitude 4.5 in the ANSS Comprehensive Earthquake Catalog (Comcat). A magnitude-dependent spatial search is used, which involves a circular search for shallow events centered on the mainshock epicenter with radius $R = 2 \times 10^{-2.44+0.59*M}$ by twice the empirical rupture length from Wells & Coppersmith (1994), following Ye et al. (2016). Here, M is the magnitude of the mainshock.

Ye et al. (2020) found a general relation for the predicted aftershock productivity for globally shallow major earthquakes with magnitude 7.0 using the same space-time window. The overall predicted productivity (NA_{pred}) is $NA_{pred} = 10^{0.99M-5.83}$, which specifies a typical aftershock productivity for each magnitude. The ratio between NA_{obs} and NA_{pred} provides a consistent measurement for each selected large strike-slip earthquake with a given magnitude (Table 1). Other clustering methods for identifying aftershocks can be used (e.g., Dascher-

Cousineau et al., 2020; Wetzler et al., 2022), and specific values vary, but the procedure here is simple and reproducible using global catalogs with a moderate magnitude of completeness. It is sufficient for our purpose of exploring basic relationships with fault zone maturation.

2.2.2 Rupture Velocity

Both observations and dynamic rupture simulations have shown that faster rupture velocity and the potential for supershear transition on faults surrounded by damaged zones are more likely on mature, well-localized and relatively straight segments of shallow faults (Huang et al., 2016; Perrin et al., 2016; Thakur & Huang, 2021; Zhang & Chen, 2006). Less mature segmented faults with offsets tend to experience rupture hiatus and slowing of average rupture speed (Bruhat et al., 2016; Goldberg et al., 2020; Hetland & Hager, 2006). Therefore, earthquake rupture velocity is a possible source property indicative of fault maturity.

The determination of rupture velocity requires very good regional seismic and geodetic constraints on the finite-fault rupture model for smaller events augmented by high-frequency back projections and surface wave measurements for larger events. Observations after 1990 tend to be more comprehensive for these measurements, but resolution varies regionally. We compile estimates of the average rupture velocity for each event from prior literature and present the information in Table 1.

2.2.3 Radiated Energy

Earthquakes occurring on immature (low cumulative displacement) faults are more likely to have more roughness at short fault wavelengths and, hence, may radiate more short-period energy per unit of moment than earthquakes occurring on smoother, more mature faults. But the radiated energy budget is in tension with fracture energy consumed in propagating the rupture along the rough surface, with plastic yielding and other dissipative processes consuming some of the available potential energy, particularly for newly emerging fault zones. As a fault matures it localizes and accumulates gauge, which may lower its strength and fracture energy (Perrin, Manighetti, & Gaudemer, 2016), with radiated energy being relatively high. While routine measures of radiated energy are routinely available from seismic recordings of our large events, as listed in Table 1, any plausible relationship to maturity is uncertain.

3. Correlations Between Each Maturity Measure and Seismological Parameters

We combine information from both the previous literature (including rupture velocity, cumulative fault displacement and segmentation results) and our systematic segmentation analysis (number of rupture segments, maximum azimuth changes, offsets of stepover between segments) and list the ranges of these parameters in Table 1. The large ranges indicated for some parameters reflect a mix of measurement procedures and uncertainty in the measurements.

Table 1. Estimated Parameters of the 34 Utilized Earthquakes

Event ID	Earthquake Information	NA_{obs}	Rupture Velocity (NA_{pred}) (km/s)	Radiated Energy (J), Moment scaled (km)	Cumulative Fault Displacements (km)	Number of Segments	Maximum Azimuth Change (Degrees)	Stepover (km)	Reference
	/11/03 M_W 7.9 Denali (United States)	0.56	-3.5	$\times 10^{16}$, 1.57×10^{-5}	-250	-6	-48	-4.2	Amand, 1957; Frankel, 2004; Grantz, 1967; Haeussler et al., 2004; Ozacar & Beck, 2004

/11/14 M_W 7.8 Kun- lun (China)	0.28	-3.6	$\times 10^{15}$, -150 8.88×10^{-6}	-5	-35	-10	Der Wo- erd et al., 2002; Fu et al., 2005; Gau- der- mer et al., 1989; Ozacar & Beck, 2004; Wen et al., 2009; Xu et al., 2006
/11/13 M_W 7.8 Kaik- oura (New Zealand)	1.76	-2	$\times 10^{16}$, -19 2.85×10^{-5}	-17	~90	-4	Cesca et al., 2017; Litch- field et al., 2018; Nicol et al., 2018; Stir- ling et al., 1996; Xu et al., 2018

/09/24	0.35	-4	$\times 10^{15}$, -460 1.54×10^{-5}	-4	-20	-1.3	Avouac et al., 2014; Valdiya & San- wal, 2017; Wang et al., 2016; Zinke et al., 2014
M_W							Barrier et al., 1991; Klinger, 2010; Ve- lasco et al., 1996
7.7							
Balochis- tan (Pak- istan)							
/07/16	2.51	-3.5	$\times 10^{16}$, -200 6.49×10^{-5}	-5	-10	NA	
M_W							
7.7							
Lu- zon (Philip- pine)							
/08/17	0.57	-4.8	$\times 10^{15}$, -88 1.11×10^{-5}	-5	-29	-0.5	Akbayram et al., 2016; Bou- chon et al., 2001; Lan- gridge et al., 2002; Sunal & Ertu- raç, 2012; Tibi et al., 2001
M_W							
7.6							
Izmit (Turkey)							

/09/28 M_W 7.5 Palu (Indonesia)	1.42	-4.3	$\times 10^{15}$, -250 1.65×10^{-5}	-4	-15	-5	Bao et al., 2019; Natawidjaja et al., 2021; Socquet et al., 2019
/05/21 M_W 7.3 Maduo (China)	1.00	-3.5	$\times 10^{15}$, ~50 1.25×10^{-5}		-17	~2	Ren et al., 2022; Yuan et al., 2022; Yue et al., 2022
/06/28 M_W 7.3 Landers (United States)	1.88	-2.9	$\times 10^{15}$, -40 1.43×10^{-5}	-7	-30	-3	Cohee & Beroza, 1994; Dreger, 1994; Jachens et al., 2002; Klinger, 2010; Wesnousky, 2006

/05/10	0.76	-3.5	$\times 10^{15}$, -105	-7	-30	-2.8	Ansari, 2021;
M_W			2.94×10^{-5}				Berberian et al., 1999;
7.3							Marchan- don et al., 2018;
Zirkuh							Tan et al., 2019;
(Iran)							Walker & Jack- son, 2004
/11/12	0.60	-4.8	$\times 10^{15}$, -88	-5	-25	-2	Akbayram et al., 2016;
M_W			1.26×10^{-5}				Birgören et al., 2004;
7.2							Bou- chon et al., 2001;
Duzce							Du- man et al., 2005;
(Turkey)							Sunal & Ertu- raç, 2012

/08/14 M_W 7.2 Nippes (Haiti)	0.65	NA	NA, NA	-12.8	-5	-10	NA	Maurer et al., 2022; Prentice et al., 2010; Saint Fleur et al., 2020
/12/07 M_W 7.2 Sarez (Tajik- istan)	1.21	-5	$\times 10^{15}$, 2.77×10^{-5}	-100	-5	-22	-2	Elliott et al., 2020; Met- zger et al., 2017; Rutte et al., 2017; Sangha et al., 2017
/04/04 M_W 7.2 El Mayor- Cucapah (United States)	1.56	-2.5	$\times 10^{15}$, 1.89×10^{-5}	-5	-8	-85	-3	Fletcher et al., 2014; Teran et al., 2015; Uchide et al., 2013; Wei et al., 2011

/10/16 M_W 7.1 Hec- tor Mine (United States)	1.33	-2.2	$\times 10^{15}$, -3.4 5.33×10^{-5}	-9	-60	-2	Jachens et al., 2002; Ji et al., 2002; Kave- rina et al., 2002; Treiman et al., 2002
/07/06 M_W 7.1 Ridge- crest Main- shock (United States)	2.09	-2	$\times 10^{14}$, -0.1 8.54×10^{-6}	-12	-90	-1.7	Amos et al., 2013; DuRoss et al., 2020; Gold- berg et al., 2020; Liu et al., 2019; Thomp- son Jobe et al., 2020
/05/27 M_W 7.1 Nefte- gorsk (Rus- sia)	1.01	-2.1	$\times 10^{15}$, -50 3.91×10^{-5}	-7	-15	-1.3	Arefiev et al., 2000; Fournier et al., 1994; Kraeva, 2004

/09/03	3.02	-2.5	$\times 10^{15}$, NA	-7	-35	-0.95	Elliott et al., 2012; Quigley et al., 2012; Quigley et al., 2019
M_W			2.51×10^{-5}				
7.0							
Darfield (New Zealand)							
/04/15	3.42	-2.5	$\times 10^{15}$, -1.4	-10	-50	-1.2	Asano & Iwata, 2016; Kobayashi et al., 2017; Scott et al., 2018; Toda et al., 2016
M_W			4.52×10^{-5}				
7.0							
Ku- mamoto (Japan)							
/01/12	4.85	-3.3	$\times 10^{15}$, -10	-5	-20	~5	Koehler et al., 2013; Meng et al., 2012; Mercier de Lépinay et al., 2011; Prentice et al., 2010; Saint Fleur et al., 2020
M_W			1.00×10^{-4}				
7.0							
Haiti (Haiti)							

/02/12 M_W 6.9 Yu- tian (China)	1.30	NA	$\times 10^{14}$, <65 3.19×10^{-5}	-7	-40	-3.4	Li et al., 2016; Ritts & Biffi, 2000; Stir- ling et al., 1996; Zhang & Ge, 2017
/04/13 M_W 6.9 Yushu (China)	1.00	-5	$\times 10^{14}$, ~60 1.42×10^{-5}	-5	-10	-2	Li et al., 2012; Lin et al., 2011; Wang & Mori, 2012; Yan & Lin, 2015; Yokota et al., 2012

/03/24 M_W 6.9 Tar- lay (Myan- mar)	1.63	-3.5	$\times 10^{14}$, -30 1.28×10^{-5}	-4	-20	-3	Feng et al., 2013; La- cassin et al., 1998; Orn- tham- marath, 2013; Tun et al., 2014
/01/24 M_W 6.7 Sivrice (Turkey)	1.26	-2.2	$\times 10^{14}$, -22 2.48×10^{-5}	-4	-10	NA	Bayrak & Ozer, 2021; Gallovic et al., 2020; Mel- gar et al., 2020; Tatar et al., 2020
/26 M_W 6.6 Bam (Iran)	0.59	~2.8	$\times 10^{14}$, -12 1.50×10^{-5}	-5	-10	NA	Jackson et al., 2006; Maleki Asayesh et al., 2020; Naka- mura et al., 2005; Walker & Jack- son, 2004

/11/24 M_W 6.6 Su- per- sti- tion Hills (United States)	0.59	~2.5	NA, NA	-43	-5	-20	-0.6	Hwang et al., 1990; Klinger, 2010; Stir- ling et al., 1996; Wes- nousky, 2006
/03/31 M_W 6.5 Stan- ley (United States)	0.25	-4	$\times 10^{14}$, ~1 1.55×10^{-5}		-4	~6	~10	Liberty et al., 2021; Yang et al., 2021
/08/08 M_W 6.5 Ji- uzhaigou (China)	0.99	~2.4	$\times 10^{13}$, ~1 1.29×10^{-5}		~2	~21	~4	Li et al., 2018; Y. Li et al., 2020; Zhang et al., 2021
/05/15 M_W 6.5 Monte Cristo Range (United States)	3.72	-2.6	$\times 10^{14}$, ~1 1.98×10^{-5}		-3	~23	NA	Li et al., 2021; Liu et al., 2021; Zheng et al., 2020

/12/29 M_W 6.4 Petrinja (Croatia)	0.94	-2	$\times 10^{14}$, -1.4 2.19×10^{-5}	-5	-70	NA	Baize et al., 2022; Markušić et al., 2021; Tondi et al., 2021
/07/04 M_W 6.4 Ridge-crest Fore-shock (United States)	1.56	-2	$\times 10^{13}$, -0.1 1.08×10^{-5}	-10	~85	-1.6	Amos et al., 2013; DuRoss et al., 2020; Goldberg et al., 2020; Thompson Jobe et al., 2020
/10/15 M_W 6.4 Imperial Valley (United States)	2.81	-3.1	$\times 10^{14}$, -43 2.59×10^{-5}	-6	-50	-0.9	Archuleta, 1984; Powers & Jordan, 2010; Stirling et al., 1996; Wesnousky, 2006

/08/24	0	-3	$\times 10^{13}$, -175	-7	-30	-1.2	Dreger et al., 2015; Ji et al., 2015; Lan- gen- heim et al., 2010
M_W			1.85×10^{-5}				
6.02							
Napa							
(United							
States)							
/09/28	1.66	-3.1	$\times 10^{13}$, -315	-5	-10	-1.5	Allmann & Shearer, 2007; Ma et al., 2008; Pow- ers & Jor- dan, 2010
M_W			9.69×10^{-6}				
5.97							
Park-							
field							
(United							
States)							

We now assess whether there are any trends between the seismic attributes (relative aftershock productivity, rupture velocity and moment-scaled radiated energy) and the geological fault complexity measurements in Figures 4 and 5, including the ranges on the parameters. Circular symbols represent the average value spanning the minimum to maximum range of each measurement.

Figure 4 shows cumulative fault displacement determined from previous geological studies versus the seismic variables. Several earthquakes on short faults among our 34 cases do not have clear documentation of the total slip along the fault. Specifically, the two Ridgecrest earthquakes (event ID 16&31), Stanley earthquake (event ID 27), Jiuzhaigou earthquake (event ID 28), and Monte Cristo Range earthquake (event ID 29) occurred on newly mapped faults without extensive prior seismicity (Goldberg et al., 2020; Liu et al., 2019; Sun et al., 2018; Yang et al., 2021; Zheng et al., 2020). We assume that these earthquakes nucleated on young faults for which the total slip is relatively small. Although no systematic approach to assess the regional fault activity for the rupture area of the 2019 Ridgecrest earthquakes had been completed at the time of the earthquakes, previous studies have mapped the right-lateral displacement of the faults at the southern end of the rupture area to be tens of meters to hundreds of meters (Amos et al., 2013; Thompson Jobe et al., 2020). Therefore, we estimated the cumulative slip of the faults nucleating the two Ridgecrest

earthquakes to be ~ 100 m. As there are no robust total fault slip values for other fault systems listed above, we approximate their total slip to be ~ 1 km. To visually distinguish these events from other events in the figure, we depict them in gray.

Apart from the Stanley earthquake, cumulative fault displacement shows scattered, but systematic trends with relatively aftershock productivity and rupture velocity. Larger cumulative fault displacement is accompanied with relatively lower aftershock productivity and higher rupture velocity. Data for the variation with radiated energy in Figure 4c is yet more scattered, with the group of very new fault ruptures deviating from a reduction in energy with increasing slip. While there is not a clear reason for any of these trends to be linear, one interpretation is that the very new ruptures of unmapped faults have particularly strong energy dissipation (high fracture energy), which evolves quickly with modest cumulative slip, and then increasing smoothness of the fault results in decreasing radiation of short period energy.

In order to quantify the strength of the trends, we use p-values, which measure the probability that the observed correlation can be created by a random trend in uncorrelated datasets. A low p-value implies a strong significance to the result. We recognize that the use of p-values in this way does not rigorously correspond to a probability of correlation, but rather merely provides a convenient tool to quantify and compare the visually apparent trends in the data.

We bootstrap 1000 times to determine the p-value ranges for a linear model in log scale using datasets with and without the gray dots. Cumulative fault displacement for data with error bars are randomly selected between the lower and upper bounds in log scale for each bootstrap. The p-values determined from red dots (excluding outliers with no measured total slip) in Figure 4a-4c suggest the rupture velocity ($p = 0.0024$) and the moment-scaled radiated energy ($p = 0.041$) yield statistically significant loglog fits to the cumulative fault displacement. Relative aftershock productivity ($p = 0.082$) has a modestly significant trend with total slip.

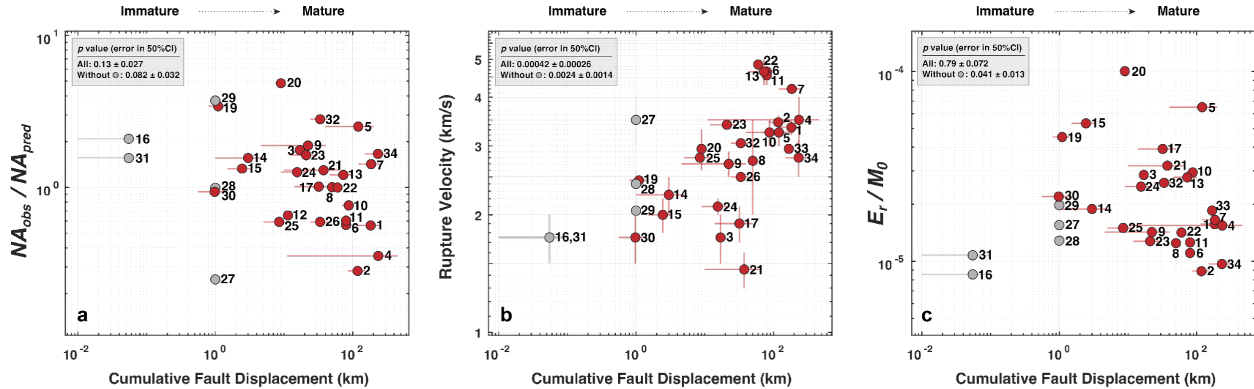


Figure 4. Cumulative fault displacement versus three seismic attributes of the

strike-slip event population. Event ID is used to identify events in Table 1 and Figure 1. Gray circles indicate ruptures of previously unmapped faults for which the cumulative displacement is set to 1 km, while other events with measured fault displacement estimates are marked in red. The strength of the trend in each panel is quantified with p-values, which are calculated both from the full dataset and the dataset without faults that do not have a total displacement.

Figure 5 shows comparisons between seismic parameters and the geological measurements of the segmentation. We generally need to be cautious with the segmentation estimates for smaller earthquakes ($M_W < 6.5$) when there is limited, or no available surface rupture measured in the field. Among the 34 studied events, the Haiti earthquake (event ID 20), Sivrice earthquake (event ID 24), Stanley earthquake (event ID 27) and Jiuzhaigou earthquake (event ID 28) do not have clear surface deformation or recognized slip (Hayes et al., 2010; Poltitz et al., 2020; Sun et al., 2018; Taymaz et al., 2021), so their segmentation estimates are from geophysical inversions and are correspondingly uncertain.

We mark the smaller events ($M_W < 6.5$) and the events without observable surface rupture in gray, so they can be visually down-weighted in Figure 5 to better detect any trend between the segmentation factors and the seismic attributes. The number of segments has a clear trend with aftershock productivity (Figure 5a) which matches the expectation that a fault with lots of segments and stress concentrations may generate more aftershocks. The number of segments also shows a trend with rupture velocity in Figure 5d where more segments correspond to lower rupture velocity, as might be expected by the difficulty in rupturing through a highly segmented system. The maximum azimuth between segments (Figure 5b, e, h) only appears to show a weak trend when the less robust data (gray dots) are neglected. The offset of stepover between segments has some relationship with rupture velocity (Figure 5f), but in general visually appears to be the weakest predictor of seismic behavior. None of the fault geometry factors are simply related to the moment-scaled radiated energy (Figure 5g-i). This last result echoes the same lack of clear correlation between moment-scaled radiated energy and total fault displacement when very immature faults are included (Figure 4c).

Our analysis suggests that correlations of the number of segments with the relative aftershock productivity ($p=0.014$) and the rupture velocity ($p=0.00022$) are significant. In addition, the maximum azimuth change shows moderately significant relation with the relative aftershock productivity ($p=0.033$) and the rupture velocity ($p=0.0024$) while the p-values for the stepover offset comparisons are too large to resolve any correlation.

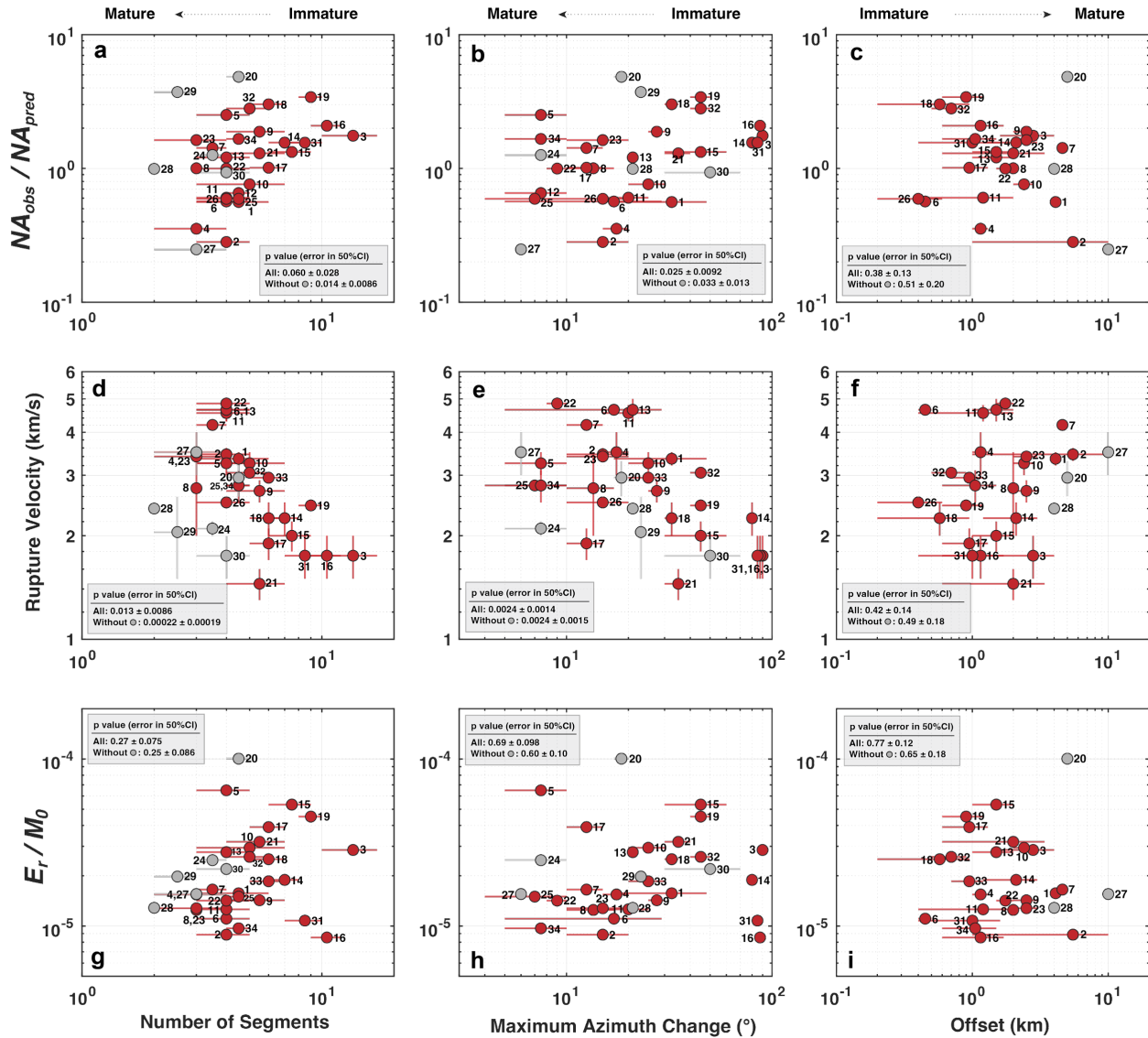


Figure 5. Estimated number of segments, azimuth changes and stepover offset between segments versus the three seismic attributes. Event ID is used corresponding to Table 1 and Figure 1. Gray circles indicate that these earthquakes either do not have documented surface rupture or the magnitudes are smaller than M_W 6.5. Other events are marked in red.

Table 2 P-values reported in Figure 4 and Figure 5

Cumulative fault displacement (Figure 4)	Number of Segments
All	Most Robust Data

Relative Aftershock Productivity	0.13±0.027	0.082±0.032
Rupture Velocity	4.2×10⁻⁴ ±2.6×10⁻⁴	0.0024±0.0014
Moment-scaled Radiated Energy	0.79±0.072	<i>0.041±0.013</i>

- a. Earthquakes with measurable cumulative fault displacement.
- b. Earthquakes with documented segmentation of the surface rupture.

Bolds indicate p-values less than 0.01, i.e., very significant. *Italics* indicate p-values between 0.01 and 0.05, i.e., marginally significant.

We summarize p-values in Table 2 and present their distributions in Figure S23. In general, rupture velocity shows the most robust behavior with the geological parameters, which suggests that it might be appropriate to use as a preliminary representation of fault maturity. The main exception is stepover width, which has no relationship with rupture velocity or anything else in this study. The correlation between the relative aftershock productivity and cumulative fault displacement is moderately significant, and there is a relationship with two of the surface rupture parameters related to segmentation: the segment number and maximum azimuth change. It is reasonable that segmentation affects aftershock production, perhaps through increasing the availability of activated faults and local stress concentrations at the ends of segments (Dascher-Cousineau et al., 2020). The moment-scaled radiated energy is relatively uncorrelated with the geological measurements from both the p-value statistical analysis and visual inspection.

4. Composite Measures of Maturity

As this discussion makes clear, fault maturity is difficult to quantify by any single measurement of a fault system. Therefore, it is also useful to consider alternative, composite approaches that combine information from more than one indicator of maturity. One such approach is to simply classify each fault system as either mature or immature based on a qualitative reading of all available data. We reach such a judgment for the fault involved in each earthquake in the supplementary text based on a reading of the available literature for each case (See first section of supplementary text). Given that maturity is intrinsically a continuous rather than binary property of fault systems, this qualitative approach must be limited in its scope, but it lends itself to a simple distinction of mature versus immature.

Figure 6 shows the resulting relationship between the qualitatively defined maturity and each seismic parameter. The result reinforces the trends noted in individual comparisons above, with higher aftershock productivity and lower rupture velocity for less mature systems.

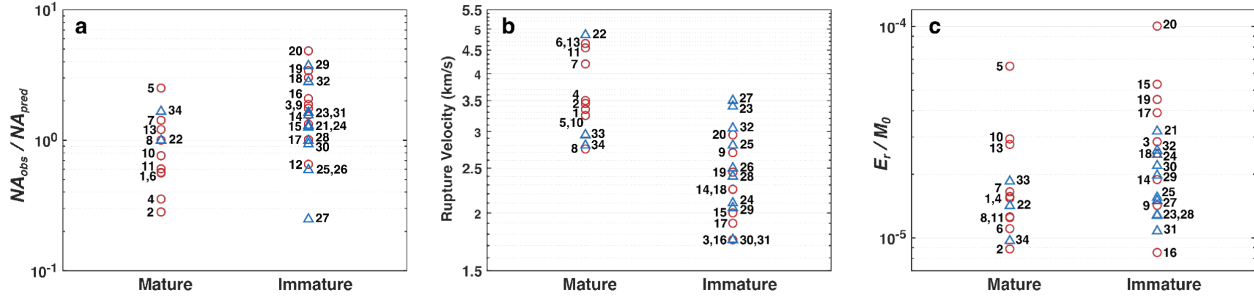


Figure 6. Qualitative bimodal fault zone maturity categorization compared with seismic parameters: (a) relative aftershock productivity, (b) rupture velocity, and (c) radiated energy normalized by moment. Red circles represent earthquakes with $M_W > 7$ while blue triangles are smaller events. Event ID is used for each individual event corresponding to Table 1 and Figure 1.

We also consider a more quantitative combination of the three field measurements that individually showed promising trends with seismic observables: cumulative fault displacement, number of segments and azimuth changes between segments. Here we define maturity based on a particular weighted linear combination of the three measures that is guided by our understanding thus far. Given that the cumulative fault displacement estimates are independent of the other two measurements and do not have a problem of lacking sufficient data, we assign the cumulative displacement values twice the weight of the other two measurements. Mature faults in our parameterization generally have larger net slip, relatively simple ruptures with few major segments and little variation in the along-strike azimuth. Immature faults have only a few kilometers of total slip and the ruptures occur on several segments with complex surface rupture traces.

This weighted combination of the fault maturity parameters gives a relative distribution from mature to immature systems that we can now compare with the seismic parameters (Figure 7). Note that p-values are provided again to help quantify the relative degree of correlation, but should not be interpreted as probabilities as the composite measure was designed to incorporate the parameters previously established to be most correlated. We see that once again mature faults again correspond to high rupture velocity and to a lesser degree high aftershock productivity while immature faults tend to have low rupture velocity and high aftershock productivity.

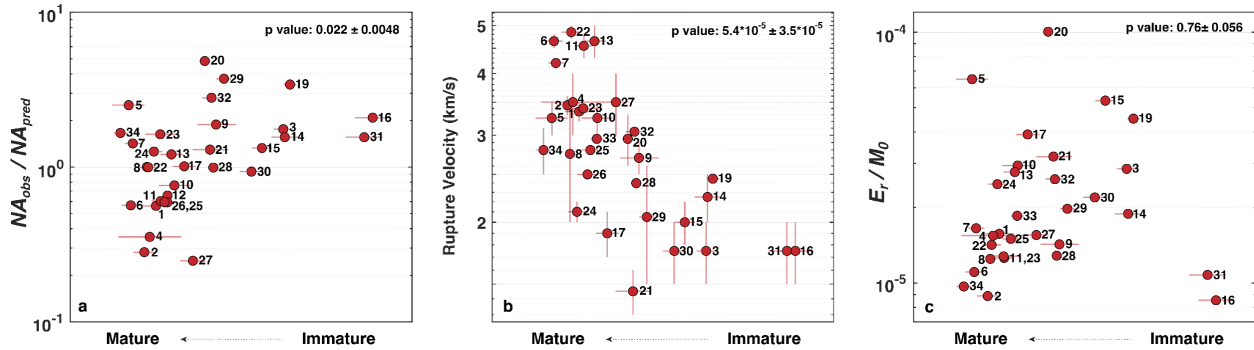


Figure 7. The linear composite measure of relative maturity from field measurements compared to (a) relative aftershock productivity, (b) rupture velocity, and (c) moment-scaled radiated energy. Event ID is used for each individual event corresponding to the legends in Figure 1.

As in the analysis of individual measures, scaled radiated energy has a high p-value and no clear correlation with maturity as quantified by the composite measure. However, there are two conspicuous outliers in the lower right-corner of Figure 7c, which are the two Ridgecrest earthquakes and without those outliers a visual trend seems evident. This is a problematic situation given that the Ridgecrest earthquakes are exceptionally well-mapped and documented and there is no reason to exclude them. They are also likely among the most extreme examples of very immature faults. This raises the intriguing possibility that the evolution of seismic radiated energy with maturity is non-monotonic.

The schematic model in Figure 8 illustrates a scenario that could lead to a non-monotonic trend in radiated energy. Fractures are relatively unaligned and distributed on very immature faults and a large earthquake in this system must dissipate more energy in breaking through to form a more continuous rupture surface. With evolution of maturity, faults become more localized and dissipation of strain energy in generating new cracks is reduced, allowing more short period energy to be radiated. For well-developed maturity faults become smooth enough that through-going ruptures have smoother moment rate-functions and comparatively little energy is radiated during the rupture process (Madariaga, 1977; Fang & Dunham, 2013). As a result, the maximum in radiated energy occurs for fault zones with intermediate maturity.



Figure 8. Schematic surface pattern of cracks in a fault system with evolving structural maturity with time or cumulative fault slip. When a large earthquake occurs in these systems, there is strong energy dissipation in the very immature case due to forming connecting cracks and overcoming stepovers; there is less consumption of fracture energy and strong radiation in the intermediate state where segments are localizing, and there is little reduced radiation from the smoother, localized mature case.

5. Summary and Conclusions

This study evaluates the degree of empirical correlation between the remotely measurable source parameters of large shallow strike-slip events and field-based estimates of maturity of the fault zone environment where these events occur. We collect geologic field measurements for 34 inland strike-slip earthquakes (M_W

6) indicative of fault system maturity from prior work to assess whether these properties are related with relative aftershock productivity, average rupture velocity, or moment-scaled radiated energy. Rupture complexity measurements are also made using a surface rupture digital dataset with an automatic segmentation procedure to provide consistency on the collected geological measurements.

We find that the cumulative fault displacement, number of rupture segments, and surface rupture azimuth changes correlate with rupture velocity. Number of segments and azimuth change also correspond to a lesser degree of aftershock productivity. Another measure of geological rupture, segment offset width, has no such correlation with any seismic parameter. No simple trend is found with moment-scaled radiated energy, but there may be distinct behavior of very immature events with no prior mapped fault and very small cumulative displacement having depressed radiated energy in addition to a separate trend of radiated energy decreasing with maturity once a through-going fault has been developed. We also explored composite measures of maturity both qualitatively

and quantitatively. A weighted linear combination of the three most important geological measurements reinforces the inference that mature faults are prone to relatively low aftershock productivity and high rupture velocity.

The empirical relationships found here provide a better understanding of variations in seismic hazard attributes of events in different fault systems. For example, less mature ruptures with lower overall rupture velocity may produce lower ground vibrations but more aftershocks than ruptures on more localized, larger-slip faults. In addition, if remote inferences of fault zone maturity are sufficiently reliable, they provide a means by which to characterize fault system complexity when there is a lack of accessible surface measurements. For oceanic, blind faulting, or isolated events in areas with poor instrument distributions, the empirical relations may improve our understanding of the evolutionary state of causal fault systems.

Acknowledgments

We thank members of the UCSC Seismology Lab for discussions. Surface rupture data can be downloaded from Natural Hazards Risk and Resiliency Research Center (<https://www.risksciences.ucla.edu/nhr3/fdhi/databases>). A MATLAB-based solver by K. Koh et al. (2008) to do the l_1 trend filtering analysis used in the systematic segmentation section is available at http://www.stanford.edu/~boyd/l1_tf/. Earthquake catalogs are downloaded from ANSS Comprehensive Earthquake Catalog (<https://earthquake.usgs.gov/earthquakes/search/>). Radiated energy values are from IRIS EQEnergy (<http://ds.iris.edu/spud/eqenergy>). This work was supported in part by the Southern California Earthquake Center Award 21175. T. Lay's research on earthquake processes is also supported by NSF grant EAR-1802364.

Open Research

All data used in this study are provided in the text in summary form, with references to the original sources.

References

- Akbayram, K., Sorlien, C. C., & Okay, A. I. (2016). Evidence for a minimum 52 ± 1 km of total offset along the northern branch of the North Anatolian Fault in northwest Turkey. *Tectonophysics*, 668–669, 35–41. <https://doi.org/10.1016/j.tecto.2015.11.026>
- Allmann, B. P., & Shearer, P. M. (2007). A high-frequency secondary event during the 2004 Parkfield Earthquake. *Science*, 318(5854), 1279–1283. <https://doi.org/10.1126/science.1146537>
- Amand, P. S. (1957). Geological and Geophysical Synthesis of the tectonics of portions of British Columbia, the Yukon Territory, and Alaska. *GSA Bulletin*, 68(10), 1343–1370. [https://doi.org/10.1130/0016-7606\(1957\)68\[1343:GAGSOT\]2.0.CO;2](https://doi.org/10.1130/0016-7606(1957)68[1343:GAGSOT]2.0.CO;2)

Amos, C. B., Brownlee, S. J., Rood, D. H., Fisher, G. B., Bürgmann, R., Renne, P. R., & Jayko, A. S. (2013). Chronology of tectonic, geomorphic, and volcanic interactions and the tempo of fault slip near Little Lake, California. *GSA Bulletin*, 125(7–8), 1187–1202. <https://doi.org/10.1130/B30803.1>

Ansari, S. (2021). Structural and stress heterogeneities along the 1997 Zirkuh earthquake fault, Eastern Iran. *Bulletin of Engineering Geology and the Environment*, 80(11), 8319–8337. <https://doi.org/10.1007/s10064-021-02436-7>

Archuleta, R. J. (1984). A faulting model for the 1979 Imperial Valley earthquake. *Journal of Geophysical Research: Solid Earth*, 89(B6), 4559–4585. <https://doi.org/10.1029/JB089iB06p04559>

Arefiev, S., Rogozhin, E., Tatevossian, R., Rivera, L., & Cisternas, A. (2000). The Neftegorsk (Sakhalin Island) 1995 earthquake: A rare interplate event. *Geophysical Journal International*, 143(3), 595–607. <https://doi.org/10.1046/j.1365-246X.2000.00234.x>

Asano, K., & Iwata, T. (2016). Source rupture processes of the foreshock and mainshock in the 2016 Kumamoto earthquake sequence estimated from the kinematic waveform inversion of strong motion data. *Earth, Planets and Space*, 68(1), 147. <https://doi.org/10.1186/s40623-016-0519-9>

Avouac, J.-P., Ayoub, F., Wei, S., Ampuero, J.-P., Meng, L., Leprince, S., Jolivet, R., Duputel, Z., & Helmberger, D. (2014). The 2013, Mw 7.7 Balochistan earthquake, energetic strike-slip reactivation of a thrust fault. *Earth and Planetary Science Letters*, 391, 128–134. <https://doi.org/10.1016/j.epsl.2014.01.036>

Baize, S., Amoroso, S., Belić, N., Benedetti, L., Boncio, P., Budić, M., Cinti, F. R., Henriquet, M., Jamšek Rupnik, P., Kordić, B., Markušić, S., Minarelli, L., Pantosti, D., Pucci, S., Špelić, M., Testa, A., Valkaniotis, S., Vukovski, M., Atanackov, J., ... Ricci, T. (2022). Environmental effects and seismogenic source characterization of the December 2020 earthquake sequence near Petrinja, Croatia. *Geophysical Journal International*, 230(2), 1394–1418. <https://doi.org/10.1093/gji/ggac123>

Bao, H., Ampuero, J.-P., Meng, L., Fielding, E. J., Liang, C., Milliner, C. W. D., Feng, T., & Huang, H. (2019). Early and persistent supershear rupture of the 2018 magnitude 7.5 Palu earthquake. *Nature Geoscience*, 12(3), Article 3. <https://doi.org/10.1038/s41561-018-0297-z>

Barrier, E., Huchon, P., & Aurelio, M. (1991). Philippine fault: A key for Philippine kinematics. *Geology*, 19(1), 32–35. [https://doi.org/10.1130/0091-7613\(1991\)019<0032:PFAKFP>2.3.CO;2](https://doi.org/10.1130/0091-7613(1991)019<0032:PFAKFP>2.3.CO;2)

Bayrak, E., & Ozer, C. (2021). The 24 January 2020 (Mw 6.8) Sivrice (Elazig, Turkey) earthquake: A first look at spatiotemporal distribution and triggering of aftershocks. *Arabian Journal of Geosciences*, 14(22), 2445. <https://doi.org/10.1007/s12517-021-08756-y>

Ben-Zion, Y., & Sammis, C. G. (2003). Characterization of fault zones. *Pure and Applied Geophysics*, 160(3), 677–715. <https://doi.org/10.1007/PL00012554>

- Berberian, M., Jackson, J. A., Qorashi, M., Khatib, M. M., Priestley, K., Talebian, M., & Ghafuri-Ashtiani, M. (1999). The 1997 May 10 Zirkuh (Qa'enat) earthquake (M_W 7.2): Faulting along the Sistan suture zone of eastern Iran. *Geophysical Journal International*, *136*(3), 671–694. <https://doi.org/10.1046/j.1365-246x.1999.00762.x>
- Bhat, H. S., Dmowska, R., King, G. C. P., Klinger, Y., & Rice, J. R. (2007). Off-fault damage patterns due to supershear ruptures with application to the 2001 Mw 8.1 Kokoxili (Kunlun) Tibet earthquake. *Journal of Geophysical Research: Solid Earth*, *112*(B6). <https://doi.org/10.1029/2006JB004425>
- Bilham, R., & Williams, P. (1985). Sawtooth segmentation and deformation processes on the southern San Andreas Fault, California. *Geophysical Research Letters*, *12*(9), 557–560. <https://doi.org/10.1029/GL012i009p00557>
- Birgören, G., Sekiguchi, H., & Irikura, K. (2004). Rupture model of the 1999 Düzce, Turkey, earthquake deduced from high and low frequency strong motion data. *Geophysical Research Letters*, *31*(5). <https://doi.org/10.1029/2003GL019194>
- Bouchon, M., & Karabulut, H. (2008). The aftershock signature of supershear earthquakes. *Science*, *320*, 1323–1325. <https://doi.org/10.1126/science.1155030>
- Bouchon, M., & Vallée, M. (2003). Observations of long supershear rupture during the magnitude 8.1 Kunlunshan earthquake. *Science*, *301*, 824–826.
- Bouchon, M., Bouin, M.-P., Karabulut, H., Toksöz, M. N., Dietrich, M., & Rosakis, A. J. (2001). How fast is rupture during an earthquake? New insights from the 1999 Turkey Earthquakes. *Geophysical Research Letters*, *28*(14), 2723–2726. <https://doi.org/10.1029/2001GL013112>
- Bruhat, L., Fang, Z., & Dunham, E. M. (2016). Rupture complexity and the supershear transition on rough faults. *Journal of Geophysical Research: Solid Earth*, *121*(1), 210–224. <https://doi.org/10.1002/2015JB012512>
- Cesca, S., Zhang, Y., Mouslopoulou, V., Wang, R., Saul, J., Savage, M., Heimann, S., Kufner, S.-K., Oncken, O., & Dahm, T. (2017). Complex rupture process of the Mw 7.8, 2016, Kaikoura earthquake, New Zealand, and its aftershock sequence. *Earth and Planetary Science Letters*, *478*, 110–120. <https://doi.org/10.1016/j.epsl.2017.08.024>
- Cohee, B. P., & Beroza, G. C. (1994). Slip distribution of the 1992 Landers earthquake and its implications for earthquake source mechanics. *Bulletin of the Seismological Society of America*, *84*(3), 692–712. <https://doi.org/10.1785/BSSA0840030692>
- Cowan, H., Nicol, A., & Tonkin, P. (1996). A comparison of historical and paleoseismicity in a newly formed fault zone and a mature fault zone, North Canterbury, New Zealand. *Journal of Geophysical Research: Solid Earth*, *101*(B3), 6021–6036. <https://doi.org/10.1029/95JB01588>

Dascher-Cousineau, K., Brodsky, E. E., Lay, T., & Goebel, T. H. W. (2020). What controls variations in aftershock productivity? *Journal of Geophysical Research: Solid Earth*, *125*(2), e2019JB018111. <https://doi.org/10.1029/2019JB018111>

Der Woerd, J. V., Tapponnier, P., J. Ryerson, F., Meriaux, A.-S., Meyer, B., Gaudemer, Y., Finkel, R. C., Caffee, M. W., Guoguan, Z., & Zhiqin, X. (2002). Uniform postglacial slip-rate along the central 600 km of the Kunlun Fault (Tibet), from ²⁶Al, ¹⁰Be, and ¹⁴C dating of riser offsets, and climatic origin of the regional morphology. *Geophysical Journal International*, *148*(3), 356–388. <https://doi.org/10.1046/j.1365-246x.2002.01556.x>

Dolan, J. F., & Haravitch, B. D. (2014). How well do surface slip measurements track slip at depth in large strike-slip earthquakes? The importance of fault structural maturity in controlling on-fault slip versus off-fault surface deformation. *Earth and Planetary Science Letters*, *388*, 38–47. <https://doi.org/10.1016/j.epsl.2013.11.043>

Dreger, D. S. (1994). Investigation of the rupture process of the 28 June 1992 Landers earthquake utilizing TERRAscope. *Bulletin of the Seismological Society of America*, *84*(3), 713–724. <https://doi.org/10.1785/BSSA0840030713>

Dreger, D., Huang, M.-H., Rodgers, A., Taira, T., & Wooddell, K. (2015). Kinematic finite-source model for the 24 August 2014 South Napa, California, Earthquake from joint inversion of seismic, GPS, and InSAR Data. *Seismological Research Letters*, *86*. <https://doi.org/10.1785/0220140244>

Duman, T. Y., Emre, O., Dogan, A., & Ozalp, S. (2005). Step-over and bend structures along the 1999 Duzce earthquake surface rupture, North Anatolian Fault, Turkey. *Bulletin of the Seismological Society of America*, *95*(4), 1250–1262. <https://doi.org/10.1785/0120040082>

Dunham, E. M., & Archuleta, R. J. (2004). Evidence for a supershear transient during the 2002 Denali Fault earthquake. *Bulletin of the Seismological Society of America*, *94*(6B), S256–S268. <https://doi.org/10.1785/0120040616>

DuRoss, C. B., Gold, R. D., Dawson, T. E., Scharer, K. M., Kendrick, K. J., Akciz, S. O., Angster, S. J., Bachhuber, J., Bacon, S., Bennett, S. E. K., Blair, L., Brooks, B. A., Bullard, T., Burgess, W. P., Chupik, C., DeFrisco, M., Delano, J., Dolan, J. F., Frost, E., ... Zinke, R. (2020). Surface displacement distributions for the July 2019 Ridgecrest, California, earthquake ruptures. *Bulletin of the Seismological Society of America*, *110*(4), 1400–1418. <https://doi.org/10.1785/0120200058>

Elliott, A., Elliott, J., Hollingsworth, J., Kulikova, G., Parsons, B., & Walker, R. (2020). Satellite imaging of the 2015 M7.2 earthquake in the Central Pamir, Tajikistan, elucidates a sequence of shallow strike-slip ruptures of the Sarez-Karakul fault. *Geophysical Journal International*, *221*(3), 1696–1718. <https://doi.org/10.1093/gji/ggaa090>

Elliott, J. R., Nissen, E. K., England, P. C., Jackson, J. A., Lamb, S., Li, Z.,

- Oehlers, M., & Parsons, B. (2012). Slip in the 2010–2011 Canterbury earthquakes, New Zealand. *Journal of Geophysical Research: Solid Earth*, 117(B3). <https://doi.org/10.1029/2011JB008868>
- Fang, Z., & Dunham, E. M. (2013). Additional shear resistance from fault roughness and stress levels on geometrically complex faults. *Journal of Geophysical Research: Solid Earth*, 118, 3642–3654. <https://doi.org/10.1002/jgrb.50262>
- Feng, W., Li, Z., Elliott, J. R., Fukushima, Y., Hoey, T., Singleton, A., Cook, R., & Xu, Z. (2013). The 2011 MW 6.8 Burma earthquake: Fault constraints provided by multiple SAR techniques. *Geophysical Journal International*, 195(1), 650–660. <https://doi.org/10.1093/gji/ggt254>
- Fletcher, J. M., Teran, O. J., Rockwell, T. K., Oskin, M. E., Hudnut, K. W., Mueller, K. J., Spelz, R. M., Akciz, S. O., Masana, E., Faneros, G., Fielding, E. J., Leprince, S., Morelan, A. E., Stock, J., Lynch, D. K., Elliott, A. J., Gold, P., Liu-Zeng, J., González-Ortega, A., ... González-García, J. (2014). Assembly of a large earthquake from a complex fault system: Surface rupture kinematics of the 4 April 2010 El Mayor–Cucapah (Mexico) M_W 7.2 earthquake. *Geosphere*, 10(4), 797–827. <https://doi.org/10.1130/GES00933.1>
- Fournier, M., Jolivet, L., Huchon, P., Sergeev, K. F., & Ostorbin, L. S. (1994). Neogene strike-slip faulting in Sakhalin and the Japan Sea opening. *Journal of Geophysical Research: Solid Earth*, 99(B2), 2701–2725. <https://doi.org/10.1029/93JB02026>
- Frankel, A. (2004). Rupture Process of the M 7.9 Denali Fault, Alaska, Earthquake: Subevents, directivity, and scaling of high-frequency ground motions. *Bulletin of the Seismological Society of America*, 94(6B), S234–S255. <https://doi.org/10.1785/0120040612>
- Fu, B., Awata, Y., Du, J., Ninomiya, Y., & He, W. (2005). Complex geometry and segmentation of the surface rupture associated with the 14 November 2001 great Kunlun earthquake, northern Tibet, China. *Tectonophysics*, 407(1), 43–63. <https://doi.org/10.1016/j.tecto.2005.07.002>
- Gallovič, F., Zahradník, J., Plicka, V., Sokos, E., Evangelidis, C., Fountoulakis, I., & Turhan, F. (2020). Complex rupture dynamics on an immature fault during the 2020 M_W 6.8 Elazığ earthquake, Turkey. *Communications Earth & Environment*, 1(1), Article 1. <https://doi.org/10.1038/s43247-020-00038-x>
- Gaudermer, Y., Tapponnier, P., & Turcotte, D. L. (1989). River offsets across active strike-slip faults. *River Offsets across Active Strike-Slip Faults*, 3(2), 55–76.
- Goldberg, D. E., Melgar, D., Sahakian, V. J., Thomas, A. M., Xu, X., Crowell, B. W., & Geng, J. (2020). Complex rupture of an immature fault zone: A simultaneous kinematic model of the 2019 Ridgecrest, CA earthquakes. *Geophysical Research Letters*, 47(3), e2019GL086382. <https://doi.org/10.1029/2019GL086382>

- Gong, W., Ye, L., Qiu, Y., Lay, T., & Kanamori, H. (2022). Rupture directivity of the 2021 M_W 6.0 Yangbi, Yunnan Earthquake. *Journal of Geophysical Research: Solid Earth*, 127(9), e2022JB024321. <https://doi.org/10.1029/2022JB024321>
- Grantz, A. (1966). Strike-slip faults in Alaska. *U. S. Geol. Serv. Open File Rep.*, 82, 66–53.
- Haeussler, P. J., Schwartz, D. P., Dawson, T. E., Stenner, H. D., Lienkaemper, J. J., Sherrod, B., Cinti, F. R., Montone, P., Craw, P. A., Crone, A. J., & Personius, S. F. (2004). Surface rupture and slip distribution of the Denali and Totschunda Faults in the 3 November 2002 M 7.9 Earthquake, Alaska. *Bulletin of the Seismological Society of America*, 94(6B), S23–S52. <https://doi.org/10.1785/0120040626>
- Hayes, G. P., Briggs, R. W., Sladen, A., Fielding, E. J., Prentice, C., Hudnut, K., Mann, P., Taylor, F. W., Crone, A. J., Gold, R., Ito, T., & Simons, M. (2010). Complex rupture during the 12 January 2010 Haiti earthquake. *Nature Geoscience*, 3(11), Article 11. <https://doi.org/10.1038/ngeo977>
- Hetland, E. A., & Hager, B. H. (2006). Interseismic strain accumulation: Spin-up, cycle invariance, and irregular rupture sequences. *Geochemistry, Geophysics, Geosystems*, 7(5). <https://doi.org/10.1029/2005GC001087>
- Huang, Y., Ampuero, J.-P., & Helmberger, D. V. (2016). The potential for supershear earthquakes in damaged fault zones – theory and observations. *Earth and Planetary Science Letters*, 433, 109–115. <https://doi.org/10.1016/j.epsl.2015.10.046>
- Hudnut, K. W., Brooks, B. A., Scharer, K., Hernandez, J. L., Dawson, T. E., Oskin, M. E., Ramon Arrowsmith, J., Goulet, C. A., Blake, K., Boggs, M. L., Bork, S., Glennie, C. L., Fernandez-Diaz, J. C., Singhanian, A., Hauser, D., & Sorhus, S. (2020). Airborne Lidar and Electro-Optical Imagery along Surface Ruptures of the 2019 Ridgecrest Earthquake Sequence, Southern California. *Seismological Research Letters*, 91(4), 2096–2107. <https://doi.org/10.1785/0220190338>
- Hwang, L. J., Magistrale, H., & Kanamori, H. (1990). Teleseismic source parameters and rupture characteristics of the 24 November 1987, Superstition Hills earthquake. *Bulletin of the Seismological Society of America*, 80(1), 43–56. <https://doi.org/10.1785/BSSA0800010043>
- Jachens, R. C., Langenheim, V. E., & Matti, J. C. (2002). Relationship of the 1999 Hector Mine and 1992 Landers Fault Ruptures to Offsets on Neogene Faults and Distribution of Late Cenozoic Basins in the Eastern California Shear Zone. *Bulletin of the Seismological Society of America*, 92(4), 1592–1605. <https://doi.org/10.1785/0120000915>
- Jackson, J., Bouchon, M., Fielding, E., Funning, G., Ghorashi, M., Hatzfeld, D., Nazari, H., Parsons, B., Priestley, K., Talebian, M., Tatar, M., Walker, R., & Wright, T. (2006). Seismotectonic, rupture process, and earthquake-hazard aspects of the 2003 December 26 Bam,

Iran, earthquake. *Geophysical Journal International*, 166(3), 1270–1292. <https://doi.org/10.1111/j.1365-246X.2006.03056.x>

Ji, C., Archuleta, R. J., & Twardzik, C. (2015). Rupture history of 2014 M_W 6.0 South Napa earthquake inferred from near-fault strong motion data and its impact to the practice of ground strong motion prediction. *Geophysical Research Letters*, 42(7), 2149–2156. <https://doi.org/10.1002/2015GL063335>

Ji, C., Wald, D. J., & Helmberger, D. V. (2002). Source description of the 1999 Hector Mine, California, Earthquake, Part II: Complexity of Slip History. *Bulletin of the Seismological Society of America*, 92(4), 1208–1226. <https://doi.org/10.1785/0120000917>

Jiao, L., Klinger, Y., & Scholtés, L. (2021). Fault segmentation pattern controlled by thickness of brittle crust. *Geophysical Research Letters*, 48, e2021GL093390. <https://doi.org/10.1029/2021GL093390>

Kaverina, A., Dreger, D., & Price, E. (2002). The combined inversion of seismic and geodetic data for the source process of the 16 October 1999 Mw 7.1 Hector Mine, California, Earthquake. *Bulletin of the Seismological Society of America*, 92(4), 1266–1280. <https://doi.org/10.1785/0120000907>

King, G., & Nábělek, J. (1985). Role of fault bends in the initiation and termination of earthquake rupture. *Science*, 228(4702), 984–987. <https://doi.org/10.1126/science.228.4702.984>

King, G., Klinger, Y., Bowman, D., & Tapponnier, P. (2005). Slip-partitioned surface breaks for the M_W 7.8 2001 Kokoxili Earthquake, China. *Bulletin of the Seismological Society of America*, 95(2), 731–738. <https://doi.org/10.1785/0120040101>

Klinger, Y. (2010). Relation between continental strike-slip earthquake segmentation and thickness of the crust. *Journal of Geophysical Research: Solid Earth*, 115(B7). <https://doi.org/10.1029/2009JB006550>

Klinger, Y., Okubo, K., Vallage, A., Champenois, J., Delorme, A., Rougier, E., Lei, Z., Knight, E. E., Munjiza, A., Satriano, C., Baize, S., Langridge, R., & Bhat, H. S. (2018). Earthquake damage patterns resolve complex rupture processes. *Geophysical Research Letters*, 45(19), 10,279–10,287. <https://doi.org/10.1029/2018GL078842>

Kobayashi, H., Koketsu, K., & Miyake, H. (2017). Rupture processes of the 2016 Kumamoto earthquake sequence: Causes for extreme ground motions. *Geophysical Research Letters*, 44(12), 6002–6010. <https://doi.org/10.1002/2017GL073857>

Koehler, R. D., Mann, P., Prentice, C. S., Brown, L., Benford, B., & Wiggins-Grandison, M. (2013). Enriquillo–Plantain Garden Fault Zone in Jamaica: Paleoseismology and seismic hazard. *Bulletin of the Seismological Society of America*, 103(2A), 971–983. <https://doi.org/10.1785/0120120215>

Kraeva, N. (2004). Tikhonov’s regularization for deconvolution in the empirical

- Green function method and vertical directivity effect. *Tectonophysics*, 383(1), 29–44. <https://doi.org/10.1016/j.tecto.2004.02.003>
- Lacassin, R., Replumaz, A., & Hervé Leloup, P. (1998). Hairpin river loops and slip-sense inversion on southeast Asian strike-slip faults. *Geology*, 26(8), 703–706. [https://doi.org/10.1130/0091-7613\(1998\)026<0703:HRLASS>2.3.CO;2](https://doi.org/10.1130/0091-7613(1998)026<0703:HRLASS>2.3.CO;2)
- Langenheim, V. E., Graymer, R. W., Jachens, R. C., McLaughlin, R. J., Wagner, D. L., & Sweetkind, D. S. (2010). Geophysical framework of the northern San Francisco Bay region, California. *Geosphere*, 6(5), 594–620. <https://doi.org/10.1130/GES00510.1>
- Langridge, R. M., Stenner, H. D., Fumal, T. E., Christofferson, S. A., Rockwell, T. K., Hartleb, R. D., Bachhuber, J., & Barka, A. A. (2002). Geometry, slip distribution, and kinematics of surface rupture on the Sakarya Fault Segment during the 17 August 1999 İzmit, Turkey, Earthquake. *Bulletin of the Seismological Society of America*, 92(1), 107–125. <https://doi.org/10.1785/0120000804>
- Li, C., Pang, J., & Zhang, Z. (2012). Characteristics, geometry, and segmentation of the surface rupture associated with the 14 April 2010 Yushu Earthquake, Eastern Tibet, China. *Bulletin of the Seismological Society of America*, 102(4), 1618–1638. <https://doi.org/10.1785/0120110261>
- Li, H., Pan, J., Lin, A., Sun, Z., Liu, D., Zhang, J., Li, C., Liu, K., Chevalier, M.-L., Yun, K., & Gong, Z. (2016). Coseismic surface ruptures associated with the 2014 M_W 6.9 Yutian Earthquake on the Altyn Tagh Fault, Tibetan Plateau. *Bulletin of the Seismological Society of America*, 106(2), 595–608. <https://doi.org/10.1785/0120150136>
- Li, Q., Tan, K., Wang, D. Z., Zhao, B., Zhang, R., Li, Y., & Qi, Y. J. (2018). Joint inversion of GNSS and teleseismic data for the rupture process of the 2017 M_W 6.5 Jiuzhaigou, China, earthquake. *Journal of Seismology*, 22(3), 805–814. <https://doi.org/10.1007/s10950-018-9733-1>
- Li, S., Tao, T., Chen, Y., He, P., Gao, F., Qu, X., & Zhu, Y. (2021). Geodetic observation and modeling of the coseismic and postseismic deformations associated with the 2020 M_W 6.5 Monte Cristo Earthquake. *Earth and Space Science*, 8(6), e2021EA001696. <https://doi.org/10.1029/2021EA001696>
- Li, Y., Bürgmann, R., & Zhao, B. (2020). Evidence of fault immaturity from shallow slip deficit and jack of postseismic deformation of the 2017 M_W 6.5 Jiuzhaigou Earthquake. *Bulletin of the Seismological Society of America*, 110(1), 154–165. <https://doi.org/10.1785/0120190162>
- Liberty, L. M., Lifton, Z. M., & Dylan Mikesell, T. (2021). The 31 March 2020 Mw 6.5 Stanley, Idaho, Earthquake: Seismotectonics and preliminary aftershock analysis. *Seismological Research Letters*, 92(2A), 663–678. <https://doi.org/10.1785/0220200319>
- Lin, A., Rao, G., Jia, D., Wu, X., Yan, B., & Ren, Z. (2011). Co-seismic strike-slip surface rupture and displacement produced by the 2010 M_W 6.9 Yushu

earthquake, China, and implications for Tibetan tectonics. *Journal of Geodynamics*, 52(3), 249–259. <https://doi.org/10.1016/j.jog.2011.01.001>

Litchfield, N. J., Villamor, P., Dissen, R. J. V., Nicol, A., Barnes, P. M., Barrell, D. J. A., Pettinga, J. R., Langridge, R. M., Little, T. A., Mountjoy, J. J., Ries, W. F., Rowland, J., Fenton, C., Stirling, M. W., Kearse, J., Berryman, K. R., Cochran, U. A., Clark, K. J., Hemphill-Haley, M., ... Zinke, R. (2018). Surface rupture of multiple crustal faults in the 2016 Mw 7.8 Kaikōura, New Zealand, earthquake. *Bulletin of the Seismological Society of America*, 108(3B), 1496–1520. <https://doi.org/10.1785/0120170300>

Liu, C., Lay, T., Brodsky, E. E., Dascher-Cousineau, K., & Xiong, X. (2019). Coseismic rupture process of the large 2019 Ridgecrest earthquakes from joint inversion of geodetic and seismological observations. *Geophysical Research Letters*, 46(21), 11820–11829. <https://doi.org/10.1029/2019GL084949>

Liu, C., Lay, T., Pollitz, F. F., Xu, J., & Xiong, X. (2021). Seismic and geodetic analysis of rupture characteristics of the 2020 M_W 6.5 Monte Cristo Range, Nevada, earthquake. *Bulletin of the Seismological Society of America*, 111(6), 3226–3236. <https://doi.org/10.1785/0120200327>

Ma, S., Custódio, S., Archuleta, R. J., & Liu, P. (2008). Dynamic modeling of the 2004 M_W 6.0 Parkfield, California, earthquake. *Journal of Geophysical Research: Solid Earth*, 113(B2). <https://doi.org/10.1029/2007JB005216>

Madariaga, R. (1977). High-frequency radiation from crack (stress drop) models of earthquake faulting. *Geophysical Journal of the Royal Astronomical Society*, 51, 625–651. <https://doi.org/10.1111/j.1365-246X.1977.tb04211.x>

Maleki Asayesh, B., Zafarani, H., & Tatar, M. (2020). Coulomb stress changes and secondary stress triggering during the 2003 (M_W 6.6) Bam (Iran) earthquake. *Tectonophysics*, 775, 228304. <https://doi.org/10.1016/j.tecto.2019.228304>

Manighetti, I., Mercier, A., & De Barros, L. (2021). Fault trace corrugation and segmentation as a measure of fault structural maturity. *Geophysical Research Letters*, 48, 32021GL095372. <https://doi.org/10.1029/2021GL095372>

Manighetti, I., Campillo, M., Bouley, S., & Cotton, F. (2007). Earthquake scaling, fault segmentation, and structural maturity. *Earth and Planetary Science Letters*, 253(3), 429–438. <https://doi.org/10.1016/j.epsl.2006.11.004>

Marchandon, M., Vergnolle, M., Sudhaus, H., & Cavalié, O. (2018). Fault geometry and slip distribution at depth of the 1997 M_W 7.2 Zirkuh Earthquake: Contribution of near-field displacement data. *Journal of Geophysical Research: Solid Earth*, 123(2), 1904–1924. <https://doi.org/10.1002/2017JB014703>

Markušić, S., Stanko, D., Penava, D., Ivančić, I., Bjelotomić Oršulić, O., Korbar, T., & Sarhosis, V. (2021). Destructive M6.2 Petrinja Earthquake (Croatia) in 2020—Preliminary multidisciplinary research. *Remote Sensing*, 13(6), Article 6. <https://doi.org/10.3390/rs13061095>

- Maurer, J., Dutta, R., Vernon, A., & Vajedian, S. (2022). Complex rupture and triggered aseismic creep during the 14 August 2021 Haiti Earthquake from satellite geodesy. *Geophysical Research Letters*, *49*(11), e2022GL098573. <https://doi.org/10.1029/2022GL098573>
- Melgar, D., Ganas, A., Taymaz, T., Valkaniotis, S., Crowell, B. W., Kapetanidis, V., Tsironi, V., Yolsal-Çevikbilen, S., & Öcalan, T. (2020). Rupture kinematics of 2020 January 24 M_W 6.7 Doğanyol-Sivrice, Turkey earthquake on the East Anatolian Fault Zone imaged by space geodesy. *Geophysical Journal International*, *223*(2), 862–874. <https://doi.org/10.1093/gji/ggaa345>
- Meng, L., Ampuero, J.-P., Sladen, A., & Rendon, H. (2012). High-resolution backprojection at regional distance: Application to the Haiti M7.0 earthquake and comparisons with finite source studies. *Journal of Geophysical Research: Solid Earth*, *117*(B4). <https://doi.org/10.1029/2011JB008702>
- Mercier de Lépinay, B., Deschamps, A., Klingelhoefer, F., Mazabraud, Y., Delouis, B., Clouard, V., Hello, Y., Crozon, J., Marcaillou, B., Graindorge, D., Vallée, M., Perrot, J., Bouin, M.-P., Saurel, J.-M., Charvis, P., & St-Louis, M. (2011). The 2010 Haiti earthquake: A complex fault pattern constrained by seismologic and tectonic observations. *Geophysical Research Letters*, *38*(22). <https://doi.org/10.1029/2011GL049799>
- Metzger, S., Schurr, B., Ratschbacher, L., Sudhaus, H., Kufner, S.-K., Schöne, T., Zhang, Y., Perry, M., & Bendick, R. (2017). The 2015 M_W 7.2 Sarez strike-slip earthquake in the Pamir Interior: Response to the underthrusting of India’s western promontory. *Tectonics*, *36*(11), 2407–2421. <https://doi.org/10.1002/2017TC004581>
- Nakamura, T., Suzuki, S., Sadeghi, H., Fatemi Aghda, S. M., Matsushima, T., Ito, Y., Hosseini, S. K., Gandomi, A. J., & Maleki, M. (2005). Source fault structure of the 2003 Bam earthquake, southeastern Iran, inferred from the aftershock distribution and its relation to the heavily damaged area: Existence of the Arg-e-Bam fault proposed. *Geophysical Research Letters*, *32*(9). <https://doi.org/10.1029/2005GL022631>
- Natawidjaja, D. H., Daryono, M. R., Prasetya, G., Udrek, Liu, P. L.-F., Hananto, N. D., Kongko, W., Triyoso, W., Puji, A. R., Meilano, I., Gunawan, E., Supendi, P., Pamumpuni, A., Irsyam, M., Faizal, L., Hidayati, S., Sapiie, B., Kusuma, M. A., & Tawil, S. (2021). The 2018 M_W 7.5 Palu ‘supershear’ earthquake ruptures geological fault’s multisegment separated by large bends: Results from integrating field measurements, LiDAR, swath bathymetry and seismic-reflection data. *Geophysical Journal International*, *224*(2), 985–1002. <https://doi.org/10.1093/gji/ggaa498>
- Nicol, A., Khajavi, N., Pettinga, J. R., Fenton, C., Stahl, T., Bannister, S., Pedley, K., Hyland-Brook, N., Bushell, T., Hamling, I., Ristau, J., Noble, D., & McColl, S. T. (2018). Preliminary geometry, displacement, and kinematics of fault ruptures in the epicentral region of the 2016 M_W 7.8 Kaikōura, New

Zealand, earthquake. *Bulletin of the Seismological Society of America*, 108(3B), 1521–1539. <https://doi.org/10.1785/0120170329>

Ornthammarath, T. (2013). A note on the strong ground motion recorded during the M_W 6.8 earthquake in Myanmar on 24 March 2011. *Bulletin of Earthquake Engineering*, 11(1), 241–254. <https://doi.org/10.1007/s10518-012-9385-4>

Ozacar, A. A., & Beck, S. L. (2004). The 2002 Denali Fault and 2001 Kunlun Fault earthquakes: Complex rupture processes of two large strike-slip events. *Bulletin of the Seismological Society of America*, 94(6B), S278–S292. <https://doi.org/10.1785/0120040604>

Page, M. T., van der Elst, N., Hardebeck, J., Felzer, K., & Michael, A. J. (2016). Three ingredients for improved global aftershock Forecasts: Tectonic region, time-dependent catalog incompleteness, and intersequence variability. *Bulletin of the Seismological Society of America*, 106(5), 2290–2301. <https://doi.org/10.1785/0120160073>

Perrin, C., Manighetti, I., Ampuero, J.-P., Cappa, F., & Gaudemer, Y. (2016). Location of largest earthquake slip and fast rupture controlled by along-strike change in fault structural maturity due to fault growth. *Journal of Geophysical Research: Solid Earth*, 121(5), 3666–3685. <https://doi.org/10.1002/2015JB012671>

Perrin, C., Manighetti, I., & Gaudemer, Y. (2016). Off-fault tip splay networks: A genetic and generic property of faults indicative of their long-term propagation. *Comptes Rendus Geoscience*, 348(1), 52–60. <https://doi.org/10.1016/j.crte.2015.05.002>

Perrin, C., Waldhauser, F., & Scholz, C. H. (2021). The shear deformation zone and the smoothing of faults with displacement. *Journal of Geophysical Research: Solid Earth*, 126(5), e2020JB020447. <https://doi.org/10.1029/2020JB020447>

Pollitz, F. F., Hammond, W. C., & Wicks, C. W. (2020). Rupture process of the M 6.5 Stanley, Idaho, earthquake inferred from seismic waveform and geodetic data. *Seismological Research Letters*, 92(2A), 699–709. <https://doi.org/10.1785/0220200315>

Powers, P. M., & Jordan, T. H. (2010). Distribution of seismicity across strike-slip faults in California. *Journal of Geophysical Research: Solid Earth*, 115(B5). <https://doi.org/10.1029/2008JB006234>

Prentice, C. S., Mann, P., Crone, A. J., Gold, R. D., Hudnut, K. W., Briggs, R. W., Koehler, R. D., & Jean, P. (2010). Seismic hazard of the Enriquillo–Plantain Garden fault in Haiti inferred from paleoseismology. *Nature Geoscience*, 3(11), Article 11. <https://doi.org/10.1038/ngeo991>

Quigley, M. C., Jiménez, A., Duffy, B., & King, T. R. (2019). Physical and statistical behavior of multifault earthquakes: Darfield earthquake case study,

New Zealand. *Journal of Geophysical Research: Solid Earth*, 124(5), 4788–4810. <https://doi.org/10.1029/2019JB017508>

Quigley, M., Dissen, R. V., Litchfield, N., Villamor, P., Duffy, B., Barrell, D., Furlong, K., Stahl, T., Bilderback, E., & Noble, D. (2012). Surface rupture during the 2010 M_W 7.1 Darfield (Canterbury) earthquake: Implications for fault rupture dynamics and seismic-hazard analysis. *Geology*, 40(1), 55–58. <https://doi.org/10.1130/G32528.1>

Ren, J., Xu, X., Zhang, G., Wang, Q., Zhang, Z., Gai, H., & Kang, W. (2022). Coseismic surface ruptures, slip distribution, and 3D seismogenic fault for the 2021 M_W 7.3 Maduo earthquake, central Tibetan Plateau, and its tectonic implications. *Tectonophysics*, 827, 229275. <https://doi.org/10.1016/j.tecto.2022.229275>

Ritts, B. D., & Biffi, U. (2000). Magnitude of post–Middle Jurassic (Bajocian) displacement on the central Altyn Tagh fault system, northwest China. *GSA Bulletin*, 112(1), 61–74. [https://doi.org/10.1130/0016-7606\(2000\)112<61:MOPJBD>2.0.CO;2](https://doi.org/10.1130/0016-7606(2000)112<61:MOPJBD>2.0.CO;2)

Rodríguez Padilla, A. M., Oskin, M. E., Millineer, C. W. D., & Plesch, A. (2022). Accrual of widespread rock damage from the 2019 Ridgecrest earthquakes. *Nature Geoscience*, 15, 222–226. <https://doi.org/10.1038/s41561-021-00888-w>

Ross, Z. E., Idini, B., Jia, Z., Stephenson, O. L., Zhong, M., Wang, X., Zhan, Z., Simons, M., Fielding, E. J., Yun, S.-H., Hauksson, E., Moore, A. W., Liu, Z., & Jung, J. (2019). Hierarchical interlocked orthogonal faulting in the 2019 Ridgecrest earthquake sequence. *Science*, 366(6463), 346–351. <https://doi.org/10.1126/science.aaz0109>

Rutte, D., Ratschbacher, L., Khan, J., Stübner, K., Hacker, B. R., Stearns, M. A., Enkelmann, E., Jonckheere, R., Pfänder, J. A., Sperner, B., & Tichomirowa, M. (2017). Building the Pamir-Tibetan Plateau—Crustal stacking, extensional collapse, and lateral extrusion in the Central Pamir: 2. Timing and rates. *Tectonics*, 36(3), 385–419. <https://doi.org/10.1002/2016TC004294>

Saint Fleur, N., Klinger, Y., & Feuillet, N. (2020). Detailed map, displacement, paleoseismology, and segmentation of the Enriquillo-Plantain Garden Fault in Haiti. *Tectonophysics*, 778, 228368. <https://doi.org/10.1016/j.tecto.2020.228368>

Sangha, S., Peltzer, G., Zhang, A., Meng, L., Liang, C., Lundgren, P., & Fielding, E. (2017). Fault geometry of 2015, M_W 7.2 Murghab, Tajikistan earthquake controls rupture propagation: Insights from InSAR and seismological data. *Earth and Planetary Science Letters*, 462, 132–141. <https://doi.org/10.1016/j.epsl.2017.01.018>

Savage, H. M., & Brodsky, E. E. (2011). Collateral damage: Evolution with displacement of fracture distribution and secondary fault strands in fault damage zones. *Journal of Geophysical Research: Solid Earth*, 116(B3). <https://doi.org/10.1029/2010JB007665>

- Scott, C. P., Arrowsmith, J. R., Nissen, E., Lajoie, L., Maruyama, T., & Chiba, T. (2018). The M7 2016 Kumamoto, Japan, earthquake: 3-D deformation along the fault and within the damage zone constrained from differential lidar topography. *Journal of Geophysical Research: Solid Earth*, *123*(7), 6138–6155. <https://doi.org/10.1029/2018JB015581>
- Shelly, D. R. (2020). A high-resolution seismic catalog for the initial 2019 Ridgecrest earthquake sequence: Foreshocks, aftershocks, and faulting complexity. *Seismological Research Letters*, *91*(4), 1971–1978. <https://doi.org/10.1785/0220190309>
- Sibson, R. H. (1985). Stopping of earthquake ruptures at dilational fault jogs. *Nature*, *316*(6025), Article 6025. <https://doi.org/10.1038/316248a0>
- Socquet, A., Hollingsworth, J., Pathier, E., & Bouchon, M. (2019). Evidence of supershear during the 2018 magnitude 7.5 Palu earthquake from space geodesy. *Nature Geoscience*, *12*(3), Article 3. <https://doi.org/10.1038/s41561-018-0296-0>
- Stirling, M. W., Wesnousky, S. G., & Shimazaki, K. (1996). Fault trace complexity, cumulative slip, and the shape of the magnitude-frequency distribution for strike-slip faults: A global survey. *Geophysical Journal International*, *124*(3), 833–868. <https://doi.org/10.1111/j.1365-246X.1996.tb05641.x>
- Sun, J., Yue, H., Shen, Z., Fang, L., Zhan, Y., & Sun, X. (2018). The 2017 Jiuzhaigou earthquake: A complicated event occurred in a young fault system. *Geophysical Research Letters*, *45*(5), 2230–2240. <https://doi.org/10.1002/2017GL076421>
- Sunal, G., & Erturaç, M. K. (2012). Estimation of the pre-North Anatolian Fault Zone pseudo-paleo-topography: A key to determining the cumulative offset of major post-collisional strike-slip faults. *Geomorphology*, *159–160*, 125–141. <https://doi.org/10.1016/j.geomorph.2012.03.013>
- Tahir, M., Grasso, J.-R., & Amorèse, D. (2012). The largest aftershock: How strong, how far away, how delayed? *Geophysical Research Letters*, *39*(4). <https://doi.org/10.1029/2011GL050604>
- Tan, F., Ge, Z., Kao, H., & Nissen, E. (2019). Validation of the 3-D phase-weighted relative back projection technique and its application to the 2016 M_W 7.8 Kaikōura earthquake. *Geophysical Journal International*, *217*(1), 375–388. <https://doi.org/10.1093/gji/ggz032>
- Tatar, O., Sözbilir, H., Koçbulut, F., Bozkurt, E., Aksoy, E., Eski, S., Özmen, B., Alan, H., & Metin, Y. (2020). Surface deformations of 24 January 2020 Sivrice (Elazığ)–Doğanyol (Malatya) earthquake ($M_W = 6.8$) along the Pütürge segment of the East Anatolian Fault Zone and its comparison with Turkey’s 100-year-surface ruptures. *Mediterranean Geoscience Reviews*, *2*(3), 385–410. <https://doi.org/10.1007/s42990-020-00037-2>
- Taymaz, T., Ganas, A., Yolsal-Çevikbilen, S., Vera, F., Eken, T., Erman,

- C., Keleş, D., Kapetanidis, V., Valkaniotis, S., Karasante, I., Tsironi, V., Gaebler, P., Melgar, D., & Öcalan, T. (2021). Source mechanism and rupture process of the 24 January 2020 M_W 6.7 Doğanyol–Sivrice earthquake obtained from seismological waveform analysis and space geodetic observations on the East Anatolian Fault Zone (Turkey). *Tectonophysics*, *804*, 228745. <https://doi.org/10.1016/j.tecto.2021.228745>
- Teran, O. J., Fletcher, J. M., Oskin, M. E., Rockwell, T. K., Hudnut, K. W., Spelz, R. M., Akciz, S. O., Hernandez-Flores, A. P., & Morelan, A. E. (2015). Geologic and structural controls on rupture zone fabric: A field-based study of the 2010 M_W 7.2 El Mayor–Cucapah earthquake surface rupture. *Geosphere*, *11*(3), 899–920. <https://doi.org/10.1130/GES01078.1>
- Thakur, P., & Huang, Y. (2021). Influence of fault zone maturity on fully dynamic earthquake cycles. *Geophysical Research Letters*, *48*(17), e2021GL094679. <https://doi.org/10.1029/2021GL094679>
- Thakur, P., Huang, Y., & Kaneko, Y. (2020). Effects of low-velocity fault damage zones on long-term earthquake behaviors on mature strike-slip faults. *Journal of Geophysical Research: Solid Earth*, *125*(8), e2020JB019587. <https://doi.org/10.1029/2020JB019587>
- Thatcher W., & Bonilla, M.G. (1989). Earthquake fault slip estimation from geologic, geodetic and seismologic observations: Implications for earthquake mechanics and fault segmentation. *U. S. Geol. Serv. Open File Rep.*, *89*, 386–399.
- Thomas, M. Y., Mitchell, T. M., & Bhat, H. S. (2017). Fault zone dynamic processes: Evolution of fault properties during seismic rupture. *Science*, *317*(5840), 905–906.
- Thompson Jobe, J. A., Philibosian, B., Chupik, C., Dawson, T., K. Bennett, S. E., Gold, R., DuRoss, C., Ladinsky, T., Kendrick, K., Haddon, E., Pierce, I., Swanson, B., & Seitz, G. (2020). Evidence of Previous Faulting along the 2019 Ridgecrest, California, Earthquake Ruptures. *Bulletin of the Seismological Society of America*, *110*(4), 1427–1456. <https://doi.org/10.1785/0120200041>
- Tibi, R., Bock, G., Xia, Y., Baumbach, M., Grosser, H., Milkereit, C., Karakisa, S., Zünbül, S., Kind, R., & Zschau, J. (2001). Rupture processes of the 1999 August 17 Izmit and November 12 Düzce (Turkey) earthquakes. *Geophysical Journal International*, *144*(2), F1–F7. <https://doi.org/10.1046/j.1365-246x.2001.00360.x>
- Toda, S., Kaneda, H., Okada, S., Ishimura, D., & Mildon, Z. K. (2016). Slip-partitioned surface ruptures for the M_W 7.0 16 April 2016 Kumamoto, Japan, earthquake. *Earth, Planets and Space*, *68*(1), 188. <https://doi.org/10.1186/s40623-016-0560-8>
- Tondi, E., Blumetti, A. M., Čičak, M., Di Manna, P., Galli, P., Invernizzi, C., Mazzoli, S., Piccardi, L., Valentini, G., Vittori, E., & Volatili, T. (2021).

- ‘Conjugate’ coseismic surface faulting related with the 29 December 2020, M_W 6.4, Petrinja earthquake (Sisak-Moslavina, Croatia). *Scientific Reports*, 11(1), Article 1. <https://doi.org/10.1038/s41598-021-88378-2>
- Treiman, J. A., Kendrick, K. J., Bryant, W. A., Rockwell, T. K., & McGill, S. F. (2002). Primary surface rupture associated with the M_W 7.1 16 October 1999 Hector Mine earthquake, San Bernardino County, California. *Bulletin of the Seismological Society of America*, 92(4), 1171–1191. <https://doi.org/10.1785/0120000923>
- Tun, S. T., Wang, Y., Khaing, S. N., Thant, M., Htay, N., Htwe, Y. M. M., Myint, T., & Sieh, K. (2014). Surface Ruptures of the M_W 6.8 March 2011 Tarlay Earthquake, Eastern Myanmar. *Bulletin of the Seismological Society of America*, 104(6), 2915–2932. <https://doi.org/10.1785/0120130321>
- Uchide, T., Yao, H., & Shearer, P. M. (2013). Spatio-temporal distribution of fault slip and high-frequency radiation of the 2010 El Mayor-Cucapah, Mexico earthquake. *Journal of Geophysical Research: Solid Earth*, 118(4), 1546–1555. <https://doi.org/10.1002/jgrb.50144>
- Valdiya, K. S., & Sanwal, J. (2017). Chapter 4—Mountain Arcs and Festoons in Pakistan. In K. S. Valdiya & J. Sanwal (Eds.), *Developments in Earth Surface Processes* (Vol. 22, pp. 111–137). Elsevier. <https://doi.org/10.1016/B978-0-444-63971-4.00004-9>
- Wallée, M., & Dunham, E. M. (2012). Observation of far-field Mach waves generated by the 2001 Kokoxili supershear earthquake. *Geophysical Research Letters*, 39(5). <https://doi.org/10.1029/2011GL050725>
- Velasco, A. A., Ammon, C. J., Lay, T., & Hagerty, M. (1996). Rupture process of the 1990 Luzon, Philippines ($M_W = 7.7$), earthquake. *Journal of Geophysical Research: Solid Earth*, 101(B10), 22419–22434. <https://doi.org/10.1029/96JB02290>
- Walker, K. T., & Shearer, P. M. (2009). Illuminating the near-sonic rupture velocities of the intracontinental Kokoxili M_W 7.8 and Denali fault M_W 7.9 strike-slip earthquakes with global P wave back projection imaging. *Journal of Geophysical Research: Solid Earth*, 114(B2). <https://doi.org/10.1029/2008JB005738>
- Walker, R., & Jackson, J. (2004). Active tectonics and late Cenozoic strain distribution in central and eastern Iran. *Tectonics*, 23(5). <https://doi.org/10.1029/2003TC001529>
- Wang, D., & Mori, J. (2012). The 2010 Qinghai, China, Earthquake: A moderate earthquake with supershear rupture. *Bulletin of the Seismological Society of America*, 102(1), 301–308. <https://doi.org/10.1785/0120110034>
- Wang, D., Mori, J., & Koketsu, K. (2016). Fast rupture propagation for large strike-slip earthquakes. *Earth and Planetary Science Letters*, 440, 115–126. <https://doi.org/10.1016/j.epsl.2016.02.022>

- Wang, D., Kawakatsu, H., Mori, J., Ali, B., Ren, Z., & Shen, X. (2016). Backprojection analyses from four regional arrays for rupture over a curved dipping fault: The M_W 7.7 24 September 2013 Pakistan earthquake. *Journal of Geophysical Research: Solid Earth*, *121*(3), 1948–1961. <https://doi.org/10.1002/2015JB012168>
- Wei, S., Fielding, E., Leprince, S., Sladen, A., Avouac, J.-P., Helmberger, D., Hauksson, E., Chu, R., Simons, M., Hudnut, K., Herring, T., & Briggs, R. (2011). Superficial simplicity of the 2010 El Mayor–Cucapah earthquake of Baja California in Mexico. *Nature Geoscience*, *4*(9), Article 9. <https://doi.org/10.1038/ngeo1213>
- Wells, D. L., & Coppersmith, K. J. (1994). New empirical relationships among magnitude, rupture length, rupture width, rupture area, and surface displacement. *Bulletin of the Seismological Society of America*, *84*(4), 974–1002.
- Wen, Y.-Y., Ma, K.-F., Song, T.-R. A., & Mooney, W. D. (2009). Validation of the rupture properties of the 2001 Kunlun, China ($M_s = 8.1$), earthquake from seismological and geological observations. *Geophysical Journal International*, *177*(2), 555–570. <https://doi.org/10.1111/j.1365-246X.2008.04063.x>
- Wesnousky, S. G. (1988). Seismological and structural evolution of strike-slip faults. *Nature*, *335*(6188), Article 6188. <https://doi.org/10.1038/335340a0>
- Wesnousky, S. G. (2006). Predicting the endpoints of earthquake ruptures. *Nature*, *444*(7117), Article 7117. <https://doi.org/10.1038/nature05275>
- Wetzler, N., Brodsky, E. E., & Lay, T. (2016). Regional and stress drop effects on aftershock productivity of large megathrust earthquakes. *Geophysical Research Letters*, *43*(23), 12,012–12,020. <https://doi.org/10.1002/2016GL071104>
- Wetzler, N., Brodsky, E. E., Chaves, E. J., Goebel, T., & Lay, T. (2022). Regional characteristics of observable foreshocks. *Seismological Research Letters*, *xx*, xxx-xxx <https://doi.org/10.1785/0220220122>
- Wibberley, C. A. J., Yielding, G., & Di Toro, G. (2008). Recent advances in the understanding of fault zone internal structure: A review. *Geological Society, London, Special Publications*, *299*(1), 5–33. <https://doi.org/10.1144/SP299.2>
- Xu, W., Feng, G., Meng, L., Zhang, A., Ampuero, J. P., Bürgmann, R., & Fang, L. (2018). Transpressional rupture cascade of the 2016 M_W 7.8 Kaikoura earthquake, New Zealand. *Journal of Geophysical Research: Solid Earth*, *123*(3), 2396–2409. <https://doi.org/10.1002/2017JB015168>
- Xu, X., Yu, G., Klinger, Y., Tapponnier, P., & Woerd, J. V. D. (2006). Reevaluation of surface rupture parameters and faulting segmentation of the 2001 Kunlunshan earthquake (M_W 7.8), northern Tibetan Plateau, China. *Journal of Geophysical Research: Solid Earth*, *111*(B5). <https://doi.org/10.1029/2004JB003488>
- Xu, X., Tong, X., Sandwell, D. T., Milliner, C. W. D., Dolan, J. F., Hollingsworth, J., Leprince, S., & Ayoub, F. (2016). Refining the

- shallow slip deficit. *Geophysical Journal International*, 204, 1867–1886. <https://doi.org/10.1093/gji/ggv563>
- Yan, B., & Lin, A. (2015). Systematic deflection and offset of the Yangtze River drainage system along the strike-slip Ganzi-Yushu-Xianshuihe Fault Zone, Tibetan Plateau. *Journal of Geodynamics*, 87, 13–25. <https://doi.org/10.1016/j.jog.2015.03.002>
- Yang, J., Zhu, H., Lay, T., Niu, Y., Ye, L., Lu, Z., Luo, B., Kanamori, H., Huang, J., & Li, Z. (2021). Multifault opposing-dip strike-slip and normal-fault rupture during the 2020 M_W 6.5 Stanley, Idaho earthquake. *Geophysical Research Letters*, 48(10), e2021GL092510. <https://doi.org/10.1029/2021GL092510>
- Ye, L., Lay, T., & Kanamori, H. (2020). Anomalously low aftershock productivity of the 2019 M_W 8.0 energetic intermediate-depth faulting beneath Peru. *Earth and Planetary Science Letters*, 549, 116528. <https://doi.org/10.1016/j.epsl.2020.116528>
- Ye, L., Lay, T., Kanamori, H., & Rivera, L. (2016). Rupture characteristics of major and great (M_W 7.0) megathrust earthquakes from 1990 to 2015: 1. Source parameter scaling relationships. *Journal of Geophysical Research: Solid Earth*, 121(2), 826–844. <https://doi.org/10.1002/2015JB012426>
- Yokota, Y., Kawazoe, Y., Yun, S., Oki, S., Aoki, Y., & Koketsu, K. (2012). Joint inversion of teleseismic and InSAR datasets for the rupture process of the 2010 Yushu, China, earthquake. *Earth, Planets and Space*, 64(11), 1047–1051. <https://doi.org/10.5047/eps.2012.04.008>
- Yuan, Z., Li, T., Su, P., Sun, H., Ha, G., Guo, P., Chen, G., & Thompson Jobe, J. (2022). Large Surface-Rupture Gaps and Low Surface Fault Slip of the 2021 M_W 7.4 Maduo Earthquake Along a Low-Activity Strike-Slip Fault, Tibetan Plateau. *Geophysical Research Letters*, 49(6), e2021GL096874. <https://doi.org/10.1029/2021GL096874>
- Yue, H., Shen, Z.-K., Zhao, Z., Wang, T., Cao, B., Li, Z., Bao, X., Zhao, L., Song, X., Ge, Z., Ren, C., Lu, W., Zhang, Y., Liu-Zeng, J., Wang, M., Huang, Q., Zhou, S., & Xue, L. (2022). Rupture process of the 2021 M 7.4 Maduo earthquake and implication for deformation mode of the Songpan-Ganzi terrane in Tibetan Plateau. *Proceedings of the National Academy of Sciences*, 119(23), e2116445119. <https://doi.org/10.1073/pnas.2116445119>
- Zhang, H., & Chen, X. (2006). Dynamic rupture on a planar fault in three-dimensional half space—I. Theory. *Geophysical Journal International*, 164(3), 633–652. <https://doi.org/10.1111/j.1365-246X.2006.02887.x>
- Zhang, H., & Ge, Z. (2017). Steptover rupture of the 2014 M_W 7.0 Yutian, Xinjiang, Earthquake. *Bulletin of the Seismological Society of America*, 107(2), 581–591. <https://doi.org/10.1785/0120160099>
- Zhang, Y., Feng, W., Li, X., Liu, Y., Ning, J., & Huang, Q. (2021). Joint inversion of rupture across a fault steptover during the 8 August 2017 M_W 6.5

Jiuzhaigou, China, earthquake. *Seismological Research Letters*, 92(6), 3386–3397. <https://doi.org/10.1785/0220210084>

Zheng, A., Chen, X., & Xu, W. (2020). Present-day deformation mechanism of the northeastern Mina Deflection revealed by the 2020 M_W 6.5 Monte Cristo Range earthquake. *Geophysical Research Letters*, 47(22), e2020GL090142. <https://doi.org/10.1029/2020GL090142>

Zinke, R., Hollingsworth, J., & Dolan, J. F. (2014). Surface slip and off-fault deformation patterns in the 2013 M_W 7.7 Balochistan, Pakistan earthquake: Implications for controls on the distribution of near-surface coseismic slip. *Geochemistry, Geophysics, Geosystems*, 15(12), 5034–5050. <https://doi.org/10.1002/2014GC005538>

Figure 1. Maps showing locations and focal mechanisms of the 34 selected shallow strike-slip earthquakes, with the focal mechanisms color-coded by hypocentral depth. Events are sorted by magnitude and labeled with numbers used as their event ID (Table 1) in the following discussion.

Figure 2. Schematic model of some geologic field measurements for a surface-rupturing fault, including cumulative fault displacement and fault segmentation related parameters such as number of primary segments and surface stepover offsets between segments.

Figure 3. The l_t trend filtering analyses for events with digitized surface rupture data. The number of segments listed in the figure is determined from the main surface rupture following the systematic segmentation method, and distributed branches are not counted. Figures S1-S22 present the final parameterizations for the number of segments for each event.

Figure 4. Cumulative fault displacement versus three seismic attributes of the strike-slip event population. Event ID is used to identify events in Table 1 and Figure 1. Gray circles indicate ruptures of previously unmapped faults for which the cumulative offset is set to 1 km, while other events with measured fault displacement estimates are marked in red. The strength of the trend in each panel is quantified with p-values, which are calculated both from the full dataset and the dataset without faults that do not have a total displacement.

Figure 5. Estimated number of segments, azimuth changes and offset between segments versus the three seismic attributes. Event ID is used corresponding to Table 1 and Figure 1. Gray dots represent that these earthquakes do not have surface rupture or the magnitudes smaller than M_W 6.5 while other events are marked in red.

Figure 6. Qualitative bimodal fault zone maturity categorization compared with seismic parameters: (a) relative aftershock productivity, (b) rupture velocity, and (c) radiated energy normalized by moment. Red circles represent earthquakes with M_W 7 while blue triangles are smaller events. Event ID is used for each individual event corresponding to Table 1 and Figure 1.

Figure 7. The linear composite measure of relative maturity from field measurements compared to (a) relative aftershock productivity, (b) rupture velocity, and (c) moment-scaled radiated energy. Event ID is used for each individual event corresponding to the legends in Figure 1.

Figure 8. Schematic surface pattern of cracks in a fault system with evolving structural maturity with time or cumulative fault slip. When a large earthquake occurs in these systems, there is strong energy dissipation in the very immature case due to forming connecting cracks and overcoming stepovers; there is less consumption of fracture energy and strong radiation in the intermediate state where segments are localizing, and there is little reduced radiation from the smoother, localized mature case.

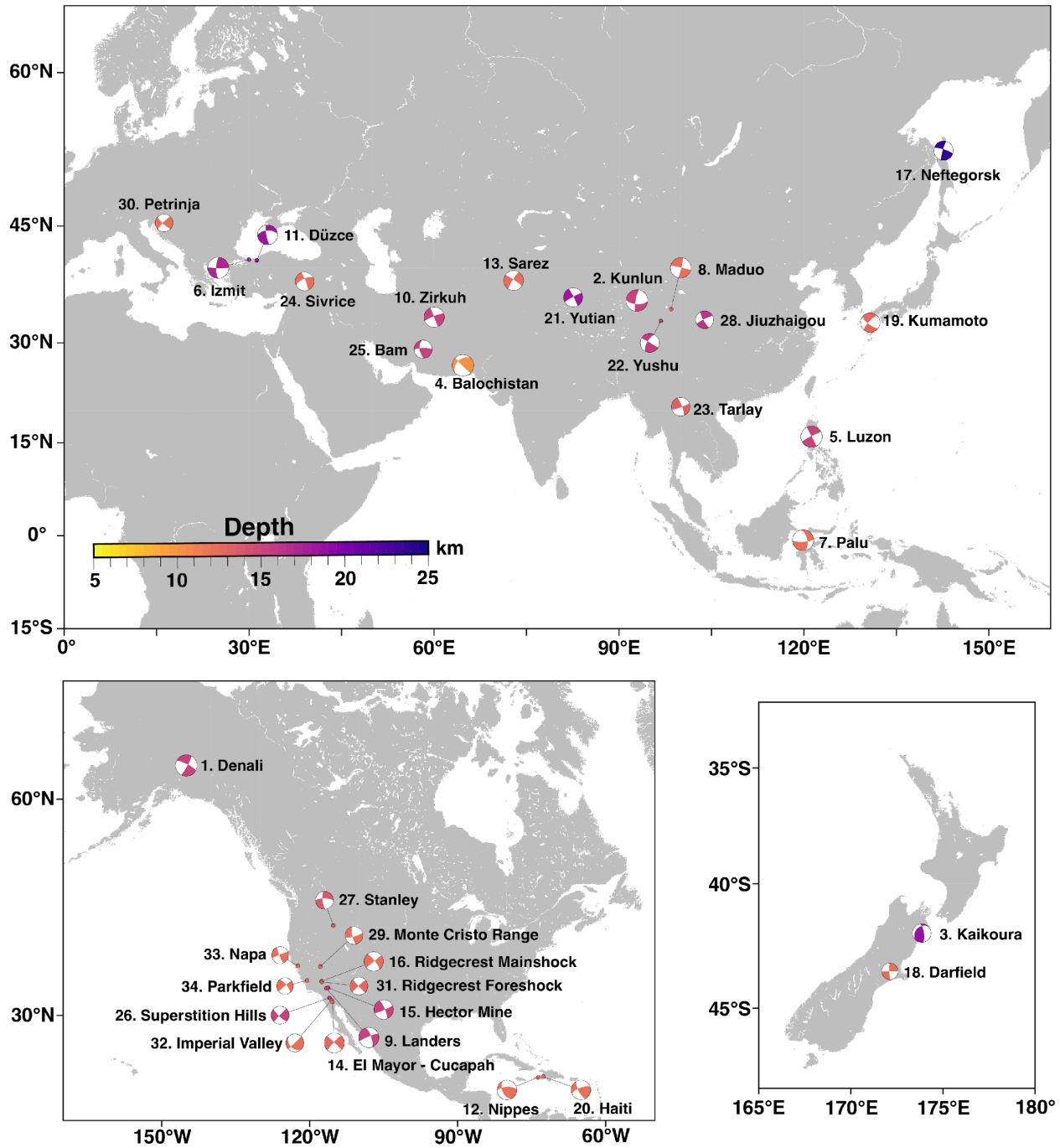


Figure 1. Maps showing locations and focal mechanisms of the 34 selected shallow strike-slip earthquakes, with the focal mechanisms color-coded by hypocen-

tral depth. Events are sorted by magnitude and labeled with numbers used as their event ID (Table 1) in the following discussion.

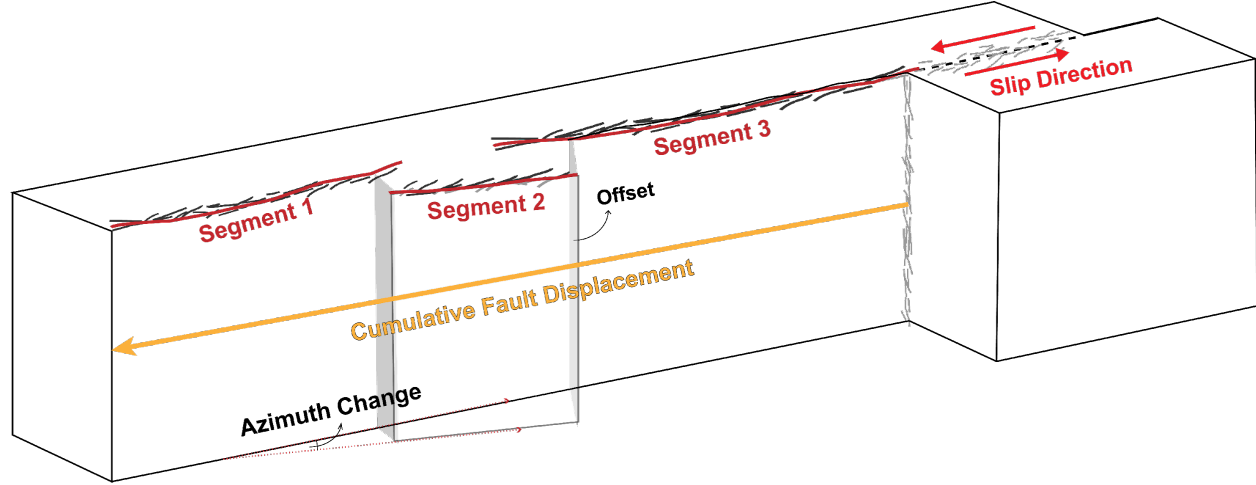


Figure 2. Schematic model of some geologic field measurements for a surface-rupturing fault, including cumulative fault displacement and fault segmentation related parameters such as number of primary segments and surface stepover offsets between segments.

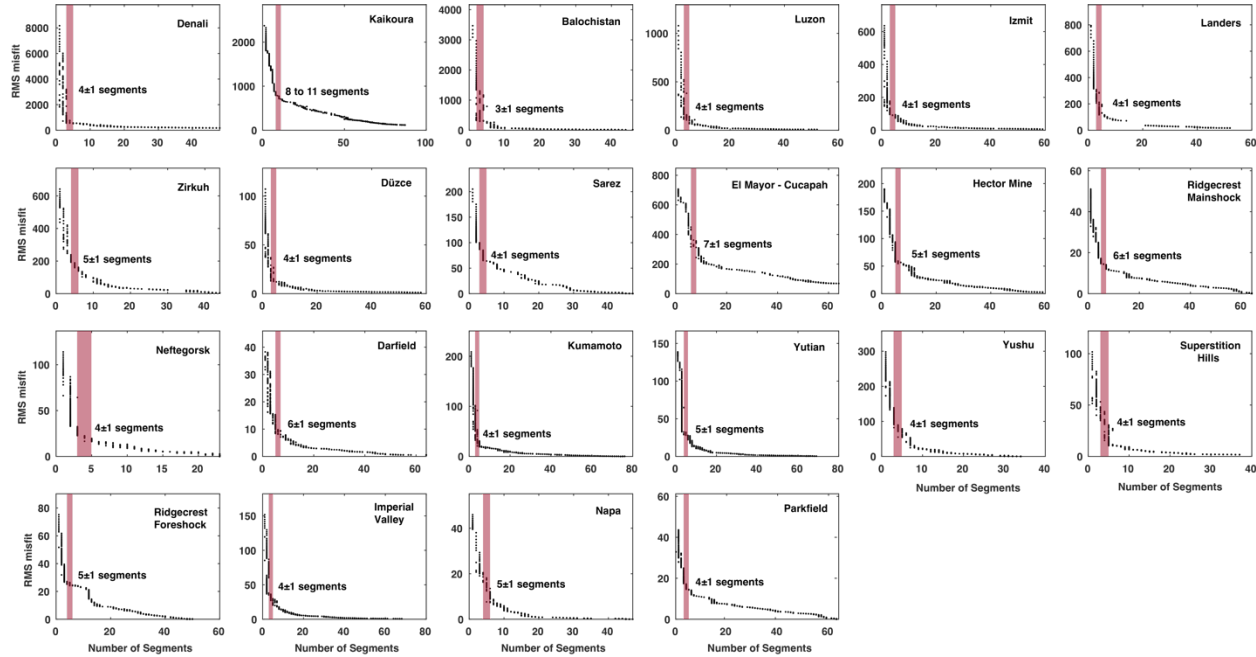


Figure 3. The l_1 trend filtering analyses for events with digitized surface rup-

ture data. The number of segments listed in the figure is determined from the main surface rupture following the systematic segmentation method, and distributed branches are not counted. Figures S1-S22 present the final parameterizations for the number of segments for each event.

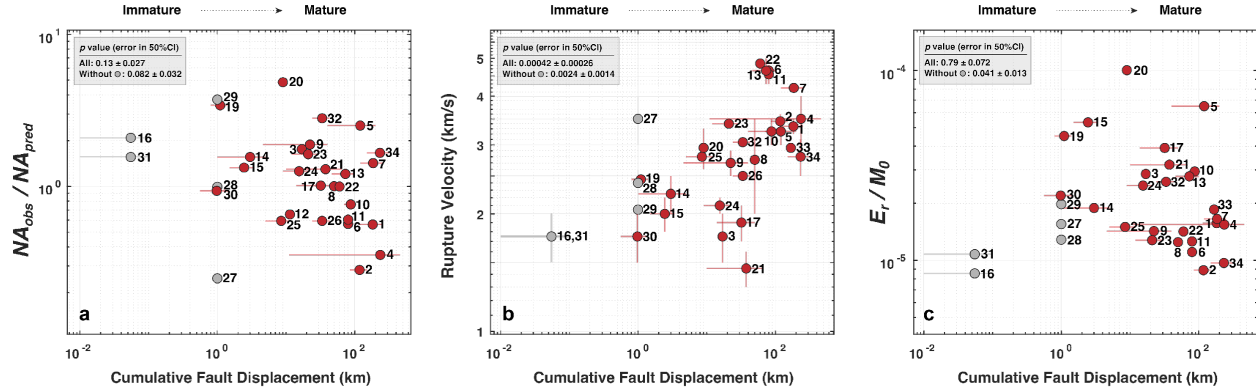


Figure 4. Cumulative fault displacement versus three seismic attributes of the strike-slip event population. Event ID is used to identify events in Table 1 and Figure 1. Gray circles indicate ruptures of previously unmapped faults for which the cumulative offset is set to 1 km, while other events with measured fault displacement estimates are marked in red. The strength of the trend in each panel is quantified with p-values, which are calculated both from the full dataset and the dataset without faults that do not have a total displacement.

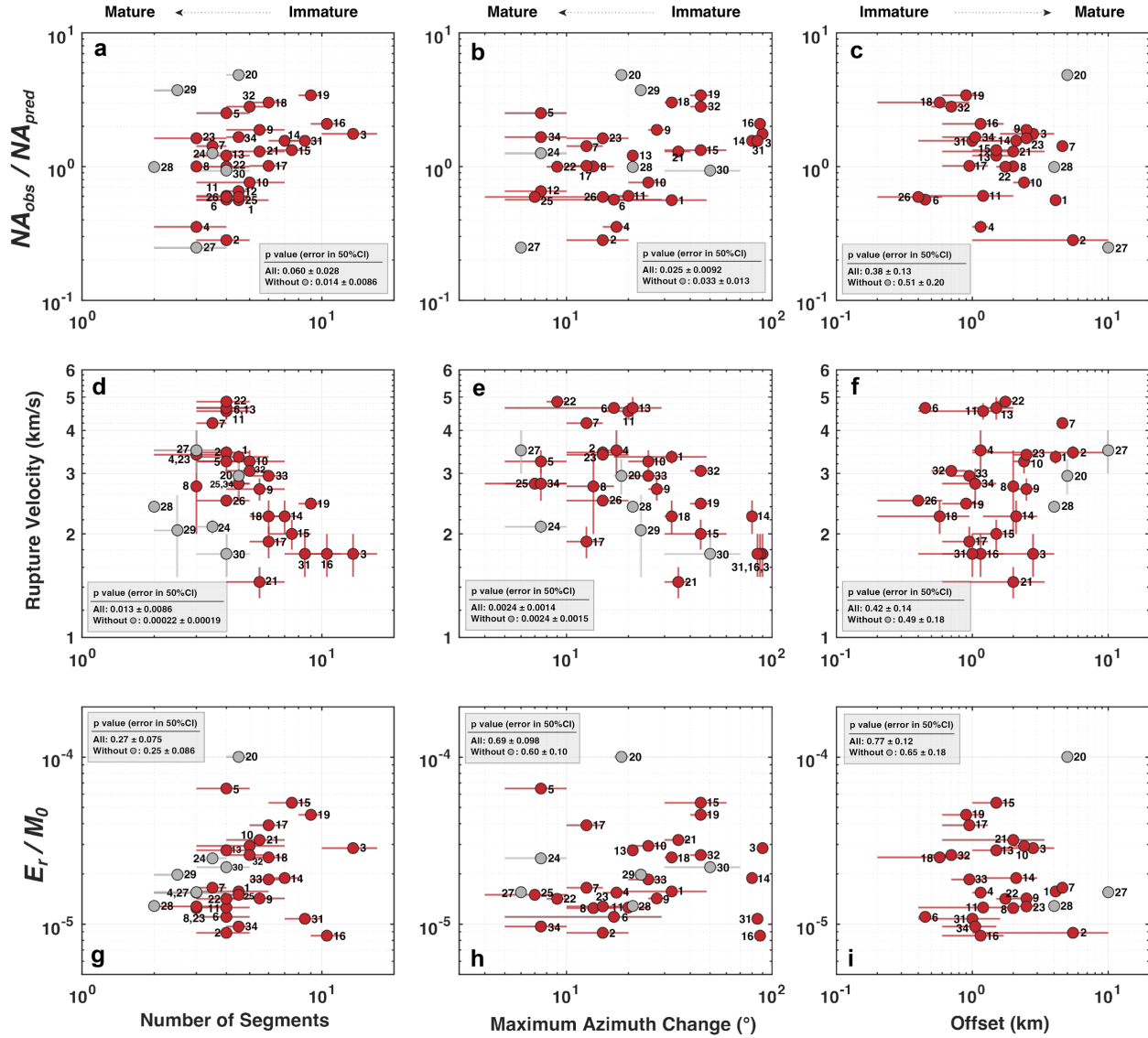


Figure 5. Estimated number of segments, azimuth changes and offset between segments versus the three seismic attributes. Event ID is used corresponding to Table 1 and Figure 1. Gray dots represent that these earthquakes do not have surface rupture or the magnitudes smaller than M_W 6.5 while other events are marked in red.

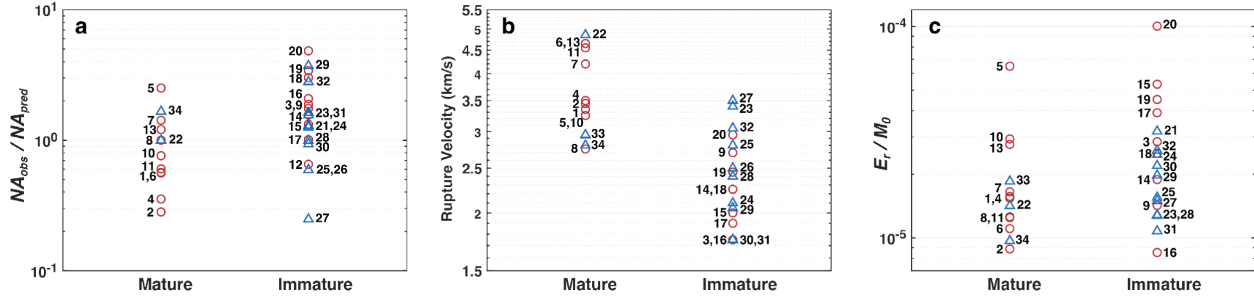


Figure 6. Qualitative bimodal fault zone maturity categorization compared with seismic parameters: (a) relative aftershock productivity, (b) rupture velocity, and (c) radiated energy normalized by moment. Red circles represent earthquakes with $M_W > 7$ while blue triangles are smaller events. Event ID is used for each individual event corresponding to Table 1 and Figure 1.

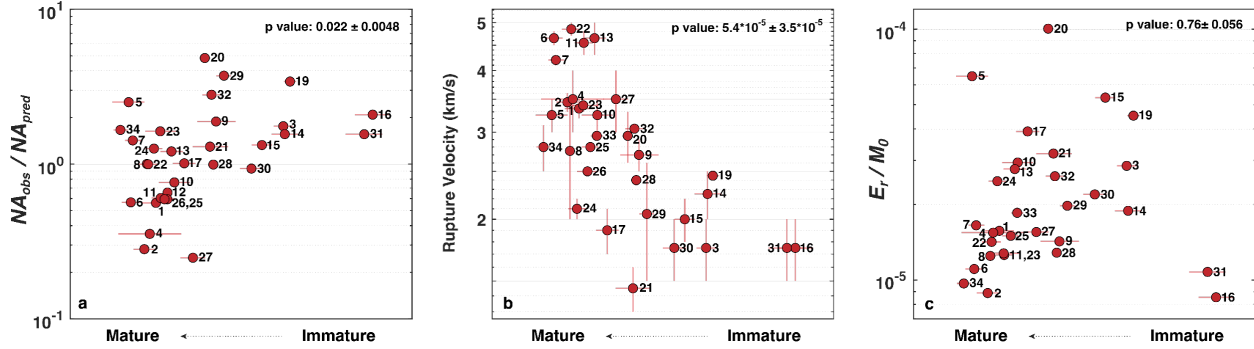


Figure 7. The linear composite measure of relative maturity from field measurements compared to (a) relative aftershock productivity, (b) rupture velocity, and (c) moment-scaled radiated energy. Event ID is used for each individual event corresponding to the legends in Figure 1.

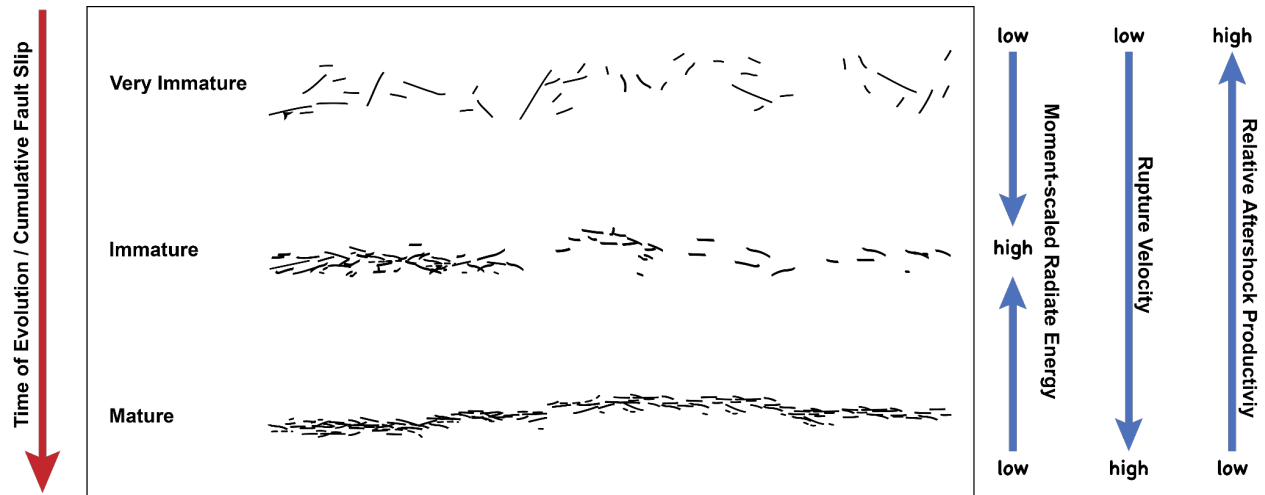


Figure 8. Schematic surface pattern of cracks in a fault system with evolving structural maturity with time or cumulative fault slip. When a large earthquake occurs in these systems, there is strong energy dissipation in the very immature case due to forming connecting cracks and overcoming stepovers; there is less consumption of fracture energy and strong radiation in the intermediate state where segments are localizing, and there is little reduced radiation from the smoother, localized mature case.



Journal of Geophysical Research: Solid Earth

Supporting Information for

Seismological Indicators of Geologically Inferred Fault Maturity

H. Guo¹, T. Lay¹, and E. E. Brodsky¹

¹Department of Earth & Planetary Sciences, University of California Santa Cruz, CA, USA

Contents of this file

Supplementary Text

Brief Description of Earthquakes in Order of Decreasing M_W

Figures S1 to S23

S1-S22: Surface rupture maps showing segmentation

S23: Distribution of p-values

SI References

Supplementary Text

The 3 November 2002 Denali Earthquake

The M_w 7.9 Denali earthquake in Alaska (Figure S1) produced 341 km of surface rupture on the Susitna Glacier, Denali, and Totschunda faults (Haeussler et al., 2004). Although the earthquake started on the Susitna Glacier which is determined to be a thrust fault, the main rupture is on the Denali fault which is a long, strike-slip fault with relatively large cumulative fault offset. Therefore, this event occurred on a mature fault system.

The 14 November 2001 Kunlun Earthquake

The Kunlun fault in east central Tibet, near the northern boundary of the Tibetan Plateau, extends ~1600 km along strike with high slip rate (Van Der Woerd et al., 2002). The total surface rupture length of the M_w 7.8 earthquake is ~430 km, which is the longest coseismic surface rupture recorded for a continental earthquake (Fu et al., 2005). Relatively simple fault traces and high cumulative offset make indicate that this fault is mature.

The 13 November 2016 Kaikōura Earthquake

The M_w 7.8 Kaikōura earthquake in New Zealand (Figure S2) ruptured across the northeastern part of the South Island. The complex surface rupture extended for approximately 165 km across the New Zealand plate boundary zone with more than 17 faults involved (Nicol et al., 2018), including many unmapped ones. Surface rupture clearly shows the intersection and bend of the fault traces. Due to the great variations in the distribution and the small cumulative offset of these faults, we consider this area to be immature.

The 24 September 2013 Balochistan Earthquake

The M_w 7.7 Balochistan earthquake (Figure S3) occurred in southern Pakistan and ruptured the Hoshab fault for ~200 km. Although the Hoshab fault had been mapped as a reverse fault, this event has dominantly left-lateral strike slip motion (Avouac et al., 2014; Barnhart et al., 2015). Although the cumulative strike-slip offset is estimated to be ~11 km from river drainages (Zinke et al., 2014), this measurement for the Chaman fault, a NS strike-slip fault connected with the northern end of the Hoshab fault, is ~460 km (Valdiya & Sanwal, 2017). Structurally mature strike-slip faults are thought to have less shallow slip deficit in the upper crust (Fialko et al., 2005). The surface rupture of this event is relatively simple with no geodetically observed shallow slip deficit and therefore, we follow the previous assessment by Zinke et al. (2014) to consider this fault as a mature fault system.

The 16 July 1990 Luzon Earthquake

The M_w 7.7 Luzon earthquake (Figure S4) has a surface rupture of at least 120 km along the left-lateral Philippine fault (Klinger, 2010). As the southern end of the rupture extended offshore, the total rupture length is uncertain. The strike of the surface rupture changed little along the propagation. No clear information on the cumulative offset of this region is documented, therefore, we estimated this measurement to be 40 to 100 km from the modelled slip rate and fault age by Barrier et al. (1991). This estimate by Klinger (2010) varies from 100 to 200 km

since the Miocene. In general, the Philippine fault has large total fault offset with no branches or large variations in azimuth and can be considered a mature fault.

The 17 August 1999 Izmit Earthquake

The M_w 7.6 Izmit earthquake (Figure S5) generated a total of 110 km of dextral surface rupture at the western end of the North Anatolian Fault Zone (Langridge et al., 2002). The NAFZ has little variation in strike angles for different segments and has relatively large cumulative fault offset estimated to be ~72 to 88 km (Sunal & Erturaç, 2012; Akbayram et al., 2016). Therefore, we consider this fault system to be mature.

The 28 September 2018 Palu Earthquake

The M_w 7.5 Palu earthquake occurred on an active strike-slip fault at the main plate boundary between the Makassar block and the North Sula block with geological offset estimated to be 120 to 250 km (Socquet et al., 2019). The large cumulative fault offset and the straight geological fault lines allow us consider this fault as mature (Natawidjaja et al., 2021). The northeast end of the surface rupture is thought to involve a less mature fault from the observed moderate deficit of slip near the surface (Socquet et al., 2019).

The 21 May 2021 Maduo Earthquake

The M_w 7.3 Maduo earthquake ruptured the internal Bayan Har Block in the central Tibetan Plateau and generated a ~154 km-long surface rupture (Ren et al., 2022). The earthquake activated on the Jiangcuo Fault, which is one of the eight subparallel left-lateral strike-slip faults that form a diffuse zone between the Eastern Kunlun Fault and the Ganzi-Yushu-Xianshuihe fault system (Yuan et al., 2022). This fault is a secondary fault with relatively low-activity and had not been well mapped in previous studies. Total fault offset of the Eastern Tibet is not well known so we estimate the cumulative fault offset of this region as a moderate value, much smaller than 150 km, the total offset for the Kunlun fault (Van Der Woerd et al., 2002). The shallow slip deficit of this event is measured to be 10% to 30 % (Yuan et al., 2022; Yue et al., 2022). We classify this fault as a mature to intermediate mature fault system.

The 28 June 1992 Landers Earthquake

The M_w 7.3 Landers earthquake (Figure S6) ruptured ~75 km along several right-lateral faults within the eastern California shear zone (ECSZ) (Klinger, 2010). Previous studies on this area have estimated the total offset across the ECSZ to be more than 40 km, whereas the cumulative strike-slip offset is ~4.6 km (Jachens et al., 2002). Considering the complex rupture traces and the moderate fault offset, we assess the Landers earthquake as occurring on a relatively immature or intermediate mature fault system.

The 10 May 1997 Zirkuh Earthquake

The M_w 7.2 Zirkuh earthquake (Figure S7) ruptured the northern part of the Abiz fault, which is the longest surface rupture in Iran and bounds the Luth block to the East. The total length of the surface rupture of this event is ~125 km (Ansari, 2021; Marchandon et al., 2018) with the cumulative offset for this region measured to be 70 to 105 km (Walker & Jackson, 2004). Ansari

(2021) suggested that the northern section of the Abiz fault has longer slip history without splay branches and is more mature than the southern section. However, considering there is no significant shallow slip deficit along the Abiz fault (Marchandon et al., 2018), we assess this fault system as mature.

The 12 November 1999 Düzce Earthquake

The M_w 7.2 Duzce earthquake (Figure S8) occurred on the North Anatolia Fault Zone (NAFZ) with the rupture length estimated to be ~40 km (Duman et al., 2005). The NAFZ has relatively large cumulative fault offset of ~72 to 88 km (Sunal & Erturaç, 2012; Akbayram et al., 2016) so the event generated on a mature fault system.

The 14 August 2021 Nippes Earthquake:

The M_w 7.2 Nippes earthquake initiated on a blind thrust fault and then jumped onto a strike-slip fault propagating westward from the epicenter accommodated by a network of segmented faults with diverse faulting conditions (Okuwaki & Fan, 2022). The main strike-slip fault across this region is the Enriquillo-Plantain Garden Fault which is a left-lateral strike-slip fault that extends over ~1100 km. The measured cumulative fault offset measured is moderate which suggests this is a relatively immature fault system.

The 7 December 2015 Sarez Earthquake

The M_w 7.2 Sarez earthquake (Figure S9) reactivated a ~79 km section of the Sarez-Karakul fault while the surface ruptures extend discontinuously for 37 km (Elliott et al., 2020; Sangha et al., 2017). The fault lines do not have large variations in strike or complex branches. Although there is no clear measurement of the total offset along this fault, the determined displacement for the strike-slip systems of the Pamir can be as large as 300 km (Schmidt et al., 2011), which indicates a mature fault system in this region.

The 4 April 2010 El Mayor- Cucapah Earthquake

The M_w 7.2 El Mayor- Cucapah earthquake (Figure S10) in 2010 ruptured for ~120 km from the northern tip of the Gulf of California to the U.S.–Mexico border. No cumulative fault offset is measured in this region. However, studies have shown that these faults are likely to have low total slip with many distributed small faults. Therefore, we infer that the faults in this region are immature.

The 16 October 1999 Hector Mine Earthquake

The M_w 7.1 Hector Mine (Figure S11) earthquake has a ~48 km-long dextral surface rupture within the eastern California shear zone (ECSZ) including various branches and segments. ECSZ have long-term displacements ranging from 1.5 to 14.4 km and a net total slip of about 65 km (Treiman et al., 2002). Most of the faults ruptured during this earthquake had prior late-Quaternary displacement while the evidence for Holocene displacement is limited. We infer that these faults can be categorized as immature.

The 6 July 2019 Ridgecrest Earthquake

The two large events in the Ridgecrest sequence (Figure S12) that occurred in the central eastern California shear zone (ECSZ) are both included in this study. Surface ruptures of both the foreshock and the mainshock show many previously unmapped orthogonal faults. These distributed strike-slip faults are young and have modest cumulative fault offset and are inferred to be immature due to the complex faulting.

The 27 May 1995 Neftegorsk Earthquake

The M_w 7.1 Neftegorsk earthquake (Figure S13) ruptured ~46 km at the northern end of Sakhalin Island, which is considered to be an inactive plate boundary between the North American and Eurasian plates (Arefiev et al., 2000). Dextral motion of the southern part of the strike-slip zone is related to the inception of subduction at the Japan arc during late Miocene. Although the main rupture is straight, there are several strands distributed at the end of the rupture. Considering the moderate cumulative fault offset, we infer this fault is immature.

The 3 September 2010 Darfield Earthquake

The M_w 7.0 Darfield earthquake (Figure S14) in New Zealand occurred on a previously unidentified fault system and ruptured the surface for ~29.5 km (Quigley et al., 2012). Although the surface rupture shows moderate variation in strike angle, the earthquake propagated across a structurally complex fault network including optimally oriented faults (M. C. Quigley et al., 2019), which suggests an immature fault system. Cumulative fault offset of this region is currently unknown.

The 14 April 2016 Kumamoto Earthquake

The M_w 7.0 Kumamoto earthquake (Figure S15) ruptured ~40 km of the Futagawa-Hinagu Fault Zone (FHFZ) on Kyushu Island, Japan (Scott et al., 2019). FHFZ activated around 0.7–0.5 Ma and may have generated a moderate cumulative displacement. The rupture involved many strands or branches scattering in space and varying in strike angle. We infer that the FHFZ is an immature fault system.

The 12 January 2010 Haiti Earthquake

The M_w 7.0 Haiti earthquake ruptured an unmapped north-dipping fault named as Léogâne fault, which is parallel to the Enriquillo–Plantain Garden fault (EPGF), one of two main strike-slip faults between the Caribbean and North American plates (Calais et al., 2010). Moderate cumulative offset for the eastern EPGF indicates that faults of this region are immature. Aftershocks of this earthquake are mainly thrust events, which occurred on an activated structure dipping to the south which might explain the relatively high productivity ratio of this event.

The 12 February 2014 Yutian Earthquake

The M_w 6.9 Yutian earthquake (Figure S16) ruptured for ~45 km while the mapped surface rupture is only 25 km and involves a big stepover. Although the event ruptured the western edge of the Altyn Tagh Fault which is a mature fault with hundreds of kilometers of total offset, its nucleation occurred at the eastern end of the South Xiaoerkule Fault which is one of the parallel

faults caused by the eastward extrusion of the Tibetan terrane relative to the Tianshuihai block. Earthquakes generated at fault ends with large stepovers are usually immature.

The existence of the large stepover slows down the rupture velocity and the bilateral propagation includes more error in determining the rupture velocity. Therefore, we do not the relation between geological measurements and rupture velocity for this specific event.

The 13 April 2010 Yushu Earthquake

The M_W 6.9 Yushu earthquake (Figure S17) occurred on the Ganzi–Yushu fault, forming part of the Yushu–Ganzi–Xianshuihe fault zone which is one of the most active fault zones in eastern Tibet. The surface rupture is separated by some stepovers a few kilometers wide and by small azimuth changes (Li et al., 2012). The cumulative fault offset of this fault is estimated from river drainage systems to be tens of kilometers. We assume this fault system is mature.

The 24 March 2011 Tarlay Earthquake

The M_W 6.8 Tarlay earthquake ruptured for ~30 km along the westernmost section of the left-lateral Nam Ma fault, Myanmar, with the coseismic surface rupture extending more than 17 km (Wang et al., 2014). The fault line is relatively straight without big bends or branches. However, the rupture occurred at the end of a fault with apparent shallow slip deficit and the relatively small cumulative fault offset indicates that this fault system is immature.

The 24 January 2020 Sivrice Earthquake

The M_W 6.7 Sivrice earthquake is the first earthquake providing rupture details of the East Anatolian Fault Zone (EAFZ) which is a major continental strike-slip fault between the Arabia plate and the Anatolian Block. Although no clear surface rupture was documented, small cracks occurred along a 48 km-long region (Çetin et al., 2020). This EAFZ event has significant slip deficit and a moderate total slip, which indicate that the EAFZ is likely to be an immature fault system.

The 26 December 2003 Bam Earthquake

The M_W 6.6 Bam earthquake occurred on a newly mapped fault at the southern end of the Nayband and Sarvestan fault located in western Dasht-e-Lut. There are no direct surface faulting features associated with this earthquake, but it produced some surface cracks which extend along a region with total length of 22.5 km (Maleki Asayesh et al., 2020). This fault system may be young and immature, accommodating reverse and strike-slip components of oblique convergence across the zone.

The 24 November 1987 Superstition Hills Earthquake

The M_W 6.6 Superstition Hills earthquake (Figure S18) ruptured a ~26 km-long section at the southern part of the right-lateral San Jacinto fault system with significant afterslip (Klinger, 2010). The cumulative offset along the Superstition Hills Fault is not well documented. The estimated moderate value indicates a fairly immature fault system.

The 31 March 2020 Stanley Earthquake

The M_W 6.5 Stanley earthquake occurred in the southern part of the Northern Rocky Mountains province, which is characterized by several active normal faults that have produced Pleistocene to Holocene ruptures. This event initiated on an unmapped strike-slip fault and traversed a 10-km-wide (at the surface) stepover. We infer that this new formed fault system is an immature one.

The 8 August 2017 Jiuzhaigou Earthquake

The M_W 6.5 Jiuzhaigou earthquake occurred on an unknown fault at the southern branch of Tazang Fault which is one of the tail structures at the easternmost Kunlun fault zone. This event has no surface rupture zones with a buried fault strand of the unmapped northern extension of the Huya fault with strong shallow slip deficit, which may reflect immaturity of this fault zone.

The 15 May 2020 Monte Cristo Range Earthquake

The M_W 6.5 Monte Cristo Range earthquake ruptured a previously unidentified fault system in the easternmost central Walker Lane Belt (WLB) which defines a complex shear zone in the Pacific-North America plate boundary. The rupture of this earthquake is segmented without prior mapped Quaternary faulting and has modest surface break, which indicates a relatively immature fault system that has not accumulated significant total slip.

The 4 July 2019 Ridgecrest Foreshock

The M_W 6.4 foreshock in the Ridgecrest sequence (Figure S19) occurred in the central eastern California shear zone (ECSZ). Surface ruptures of the foreshock and mainshock show many previously unmapped orthogonal faults. These distributed strike-slip faults are young and have very small cumulative fault offset and are inferred to be immature due to the complex faulting.

The 29 December 2020 Petrinja Earthquake

The M_W 6.4 Petrinja earthquake has a ~13 km-long rupture at conjugate faults dominated by the active Pokuplje Fault associated with the motion between Adria and the Eurasian Plate. Total offset of this fault system is few which suggests that the fault is immature.

The 15 October 1979 Imperial Valley Earthquake

The M_W 6.4 Imperial Valley earthquake (Figure S20) is the oldest event utilized in this study and ruptured ~30 km along the northern section of the Imperial fault at the US-Mexico border. The Imperial fault has the same slip rate as the San Jacinto fault with moderate cumulative fault slip (Lindsey & Fialko, 2016; Powers & Jordan, 2010; Stirling et al., 1996) and can be characterized as a relatively immature fault system.

The 24 August 2014 Napa Earthquake

The M_W 6.0 South Napa earthquake (Figure S21) occurred in the San Francisco Bay Area and produced a 12 km long surface rupture with right-lateral strike-slip displacement. The East Bay fault system has a relatively large right-lateral offset. Although there are many small fault lines

in the surface rupture, they are short compared to the main rupture and may not represent the fault distribution properly. We infer that the fault system in this region is moderately mature.

The 28 September 2004 Parkfield Earthquake

The M_W 6.0 Parkfield earthquake on the central San Andreas Fault has been documented to have large total offset at around 315 km. Surface rupture of this event is clear and straight without distributed branches. Therefore, this event occurred on a mature fault system.

Figures

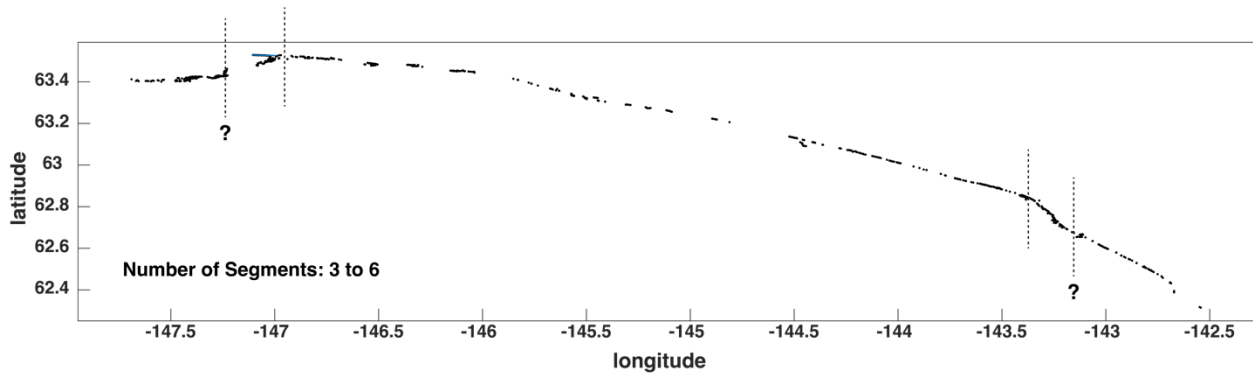


Figure S1. Surface rupture and segmentation results for the Denali earthquake. Dashed lines present the possible segment limits. Those with question markers are alternative possibilities that are uncertain.

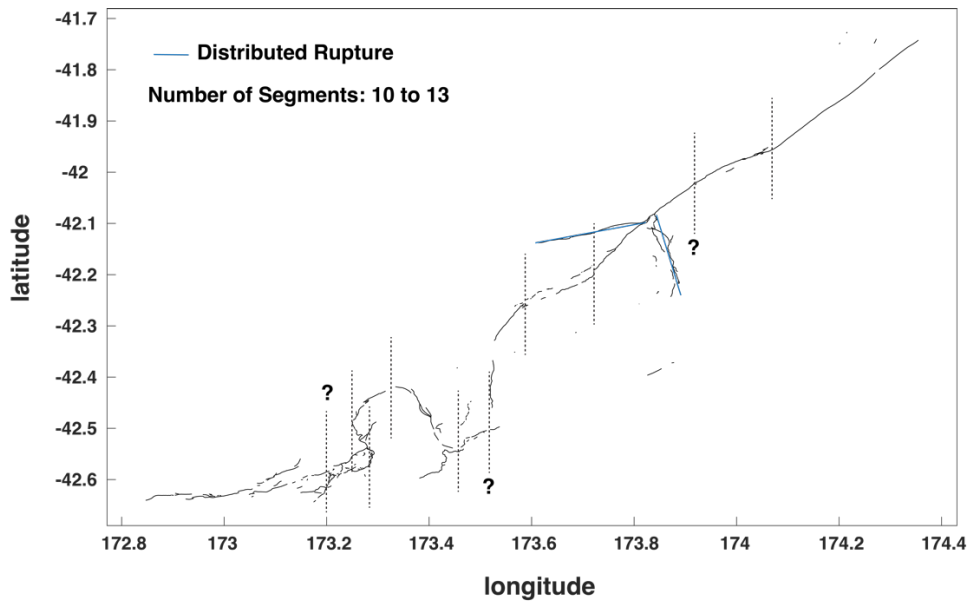


Figure S2. Surface rupture and segmentation results for the Kaikoura earthquake.

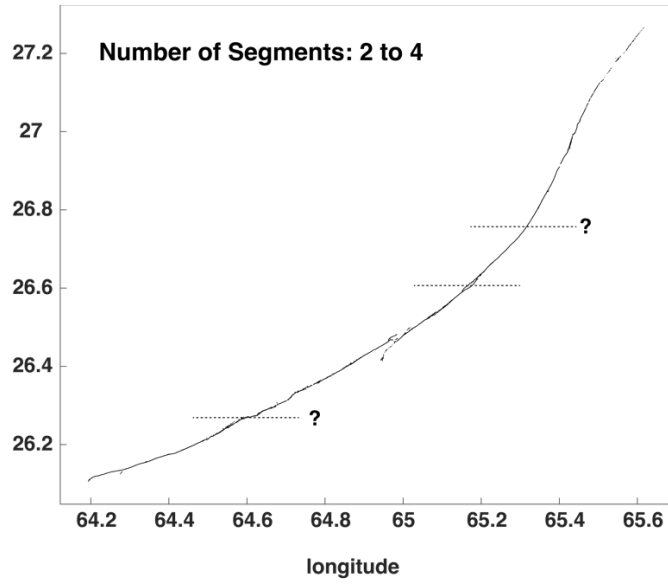


Figure S3. Surface rupture and segmentation results for the Balochistan earthquake.

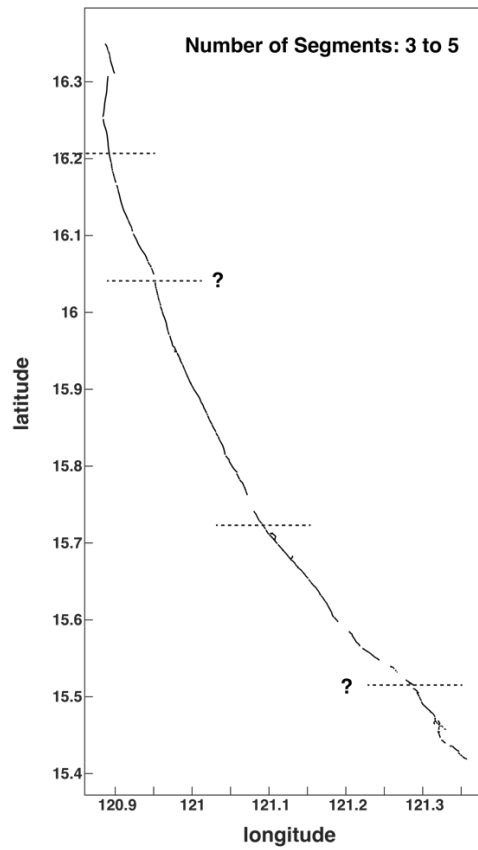


Figure S4. Surface rupture and segmentation results for the Luzon earthquake.

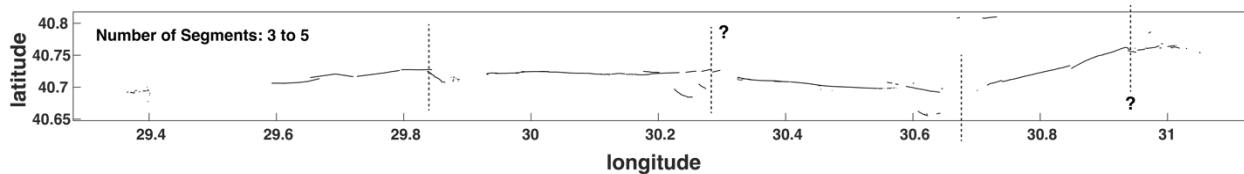


Figure S5. Surface rupture and segmentation results for the Izmit earthquake.

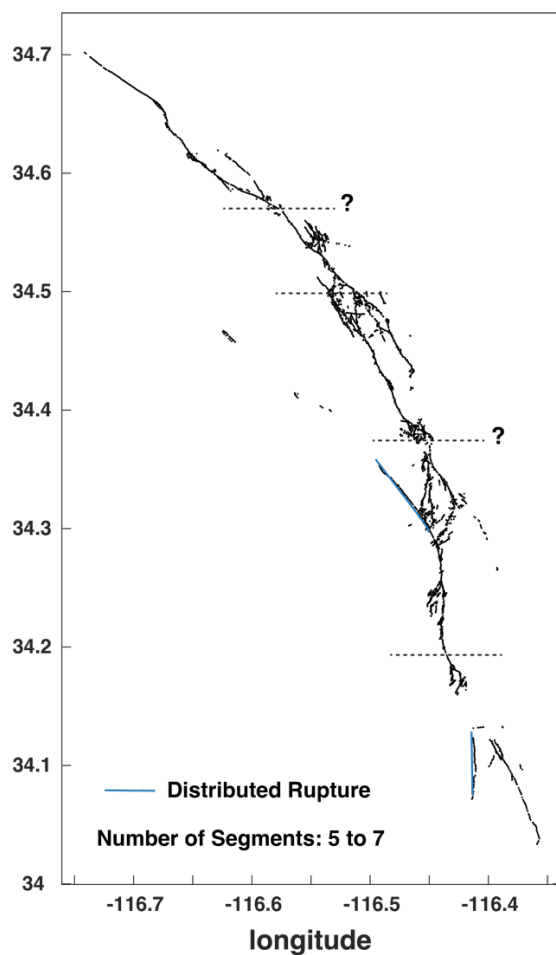


Figure S6. Surface rupture and segmentation results for the Landers earthquake.

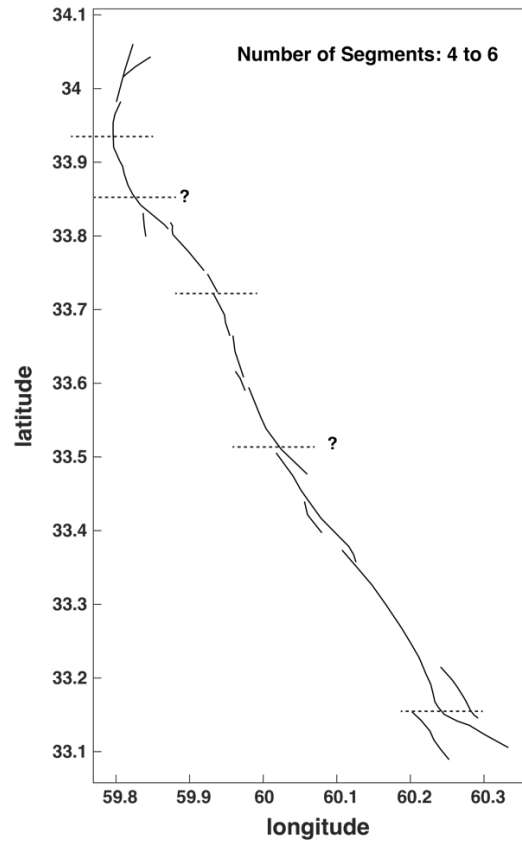


Figure S7. Surface rupture and segmentation results for the Zirkuh earthquake.

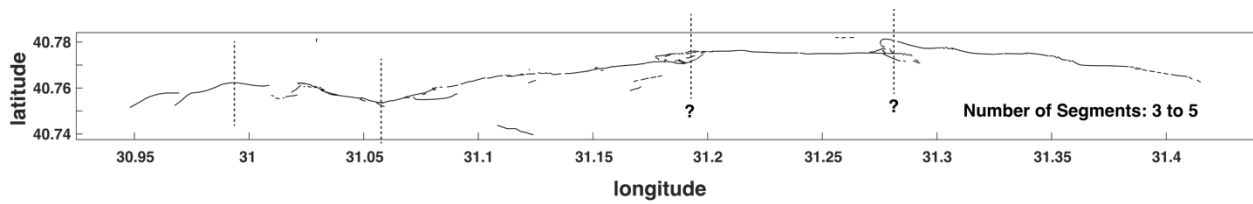


Figure S8. Surface rupture and segmentation results for the Düzce earthquake.

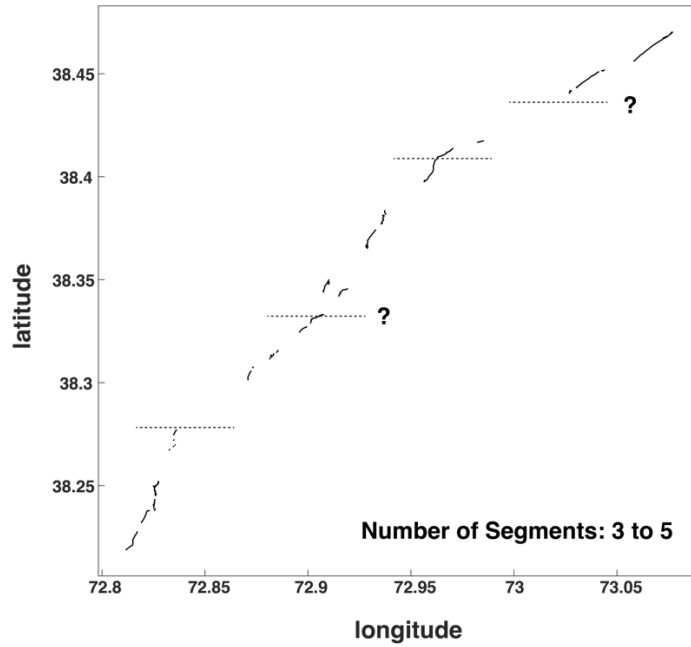


Figure S9. Surface rupture and segmentation results for the Sarez earthquake.

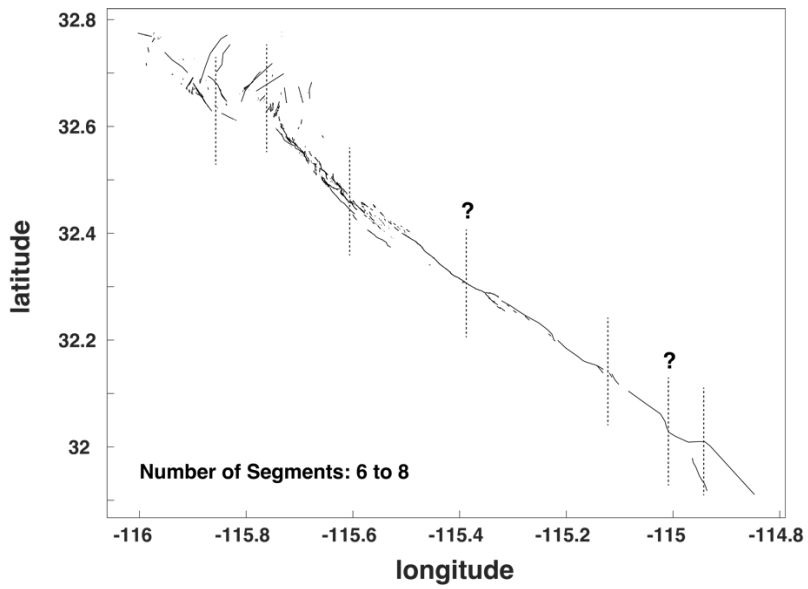


Figure S10. Surface rupture and segmentation results for the El Mayor - Cucapah earthquake.

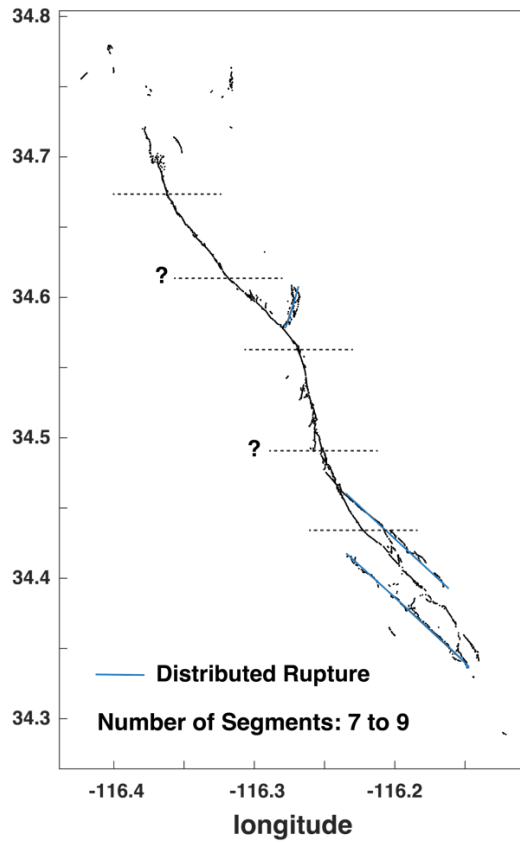


Figure S11. Surface rupture and segmentation results for the Hector Mine earthquake.

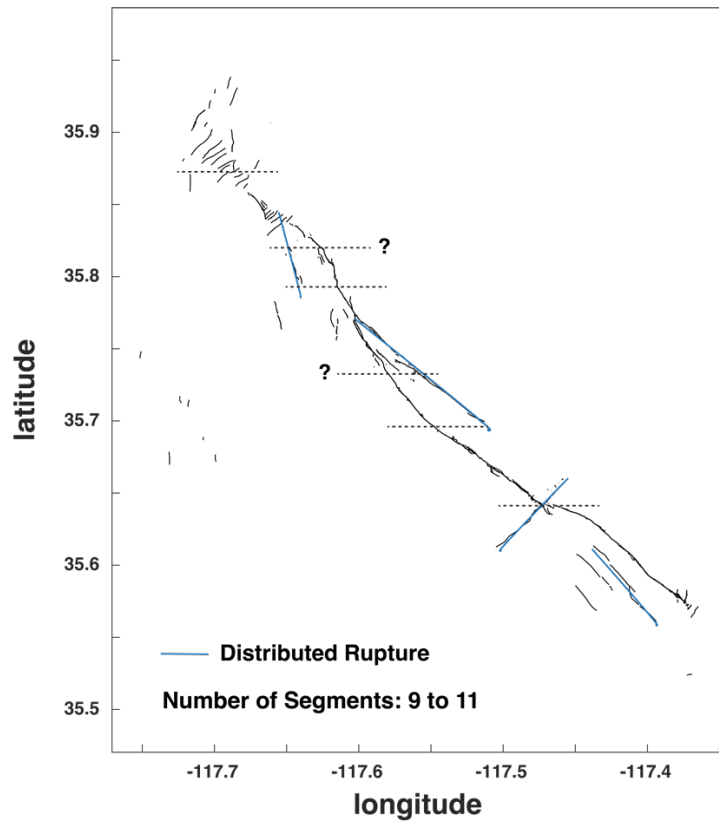


Figure S12. Surface rupture and segmentation results for the Ridgecrest mainshock.

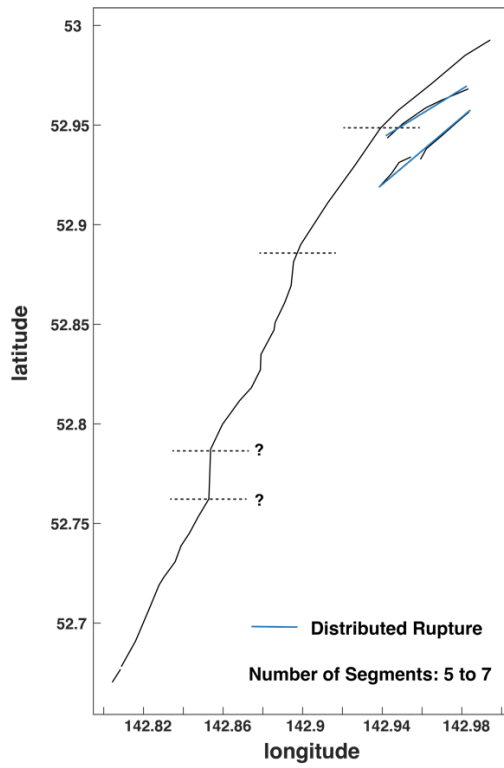


Figure S13. Surface rupture and segmentation results for the Neftegorsk earthquake.

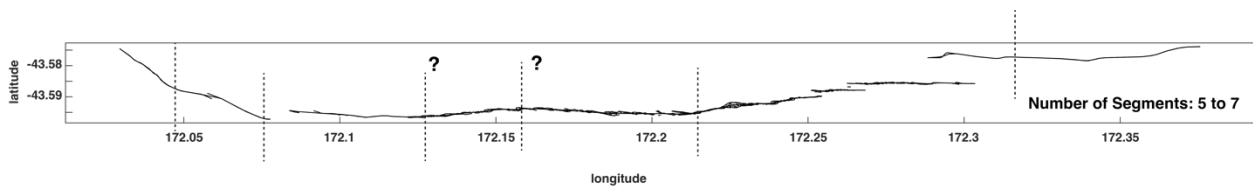


Figure S14. Surface rupture and segmentation results for the Darfield earthquake.

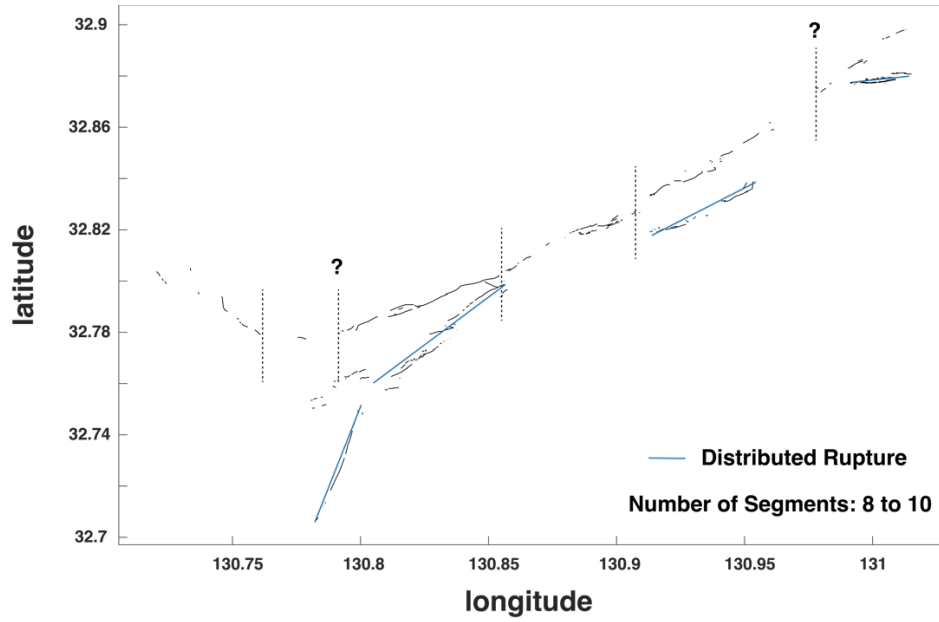


Figure S15. Surface rupture and segmentation results for the Kumamoto earthquake.

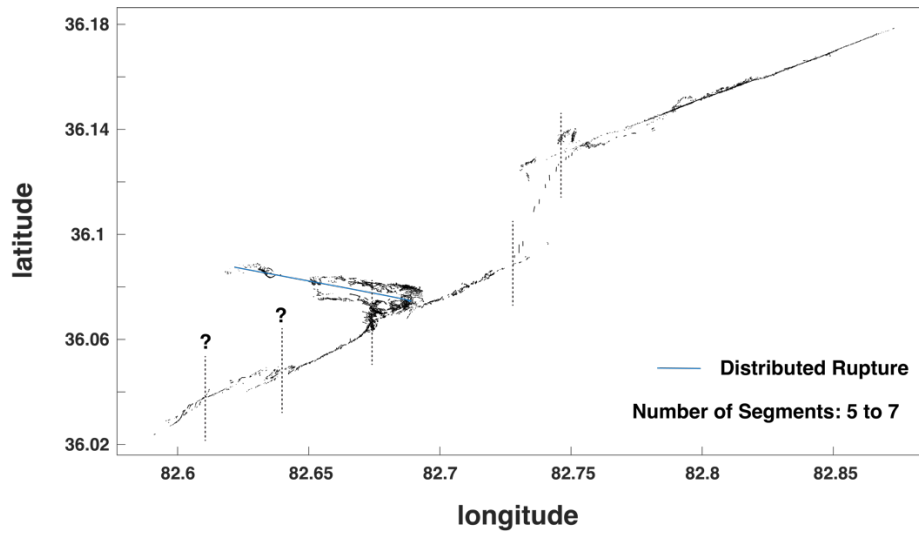


Figure S16. Surface rupture and segmentation results for the Yutian earthquake.

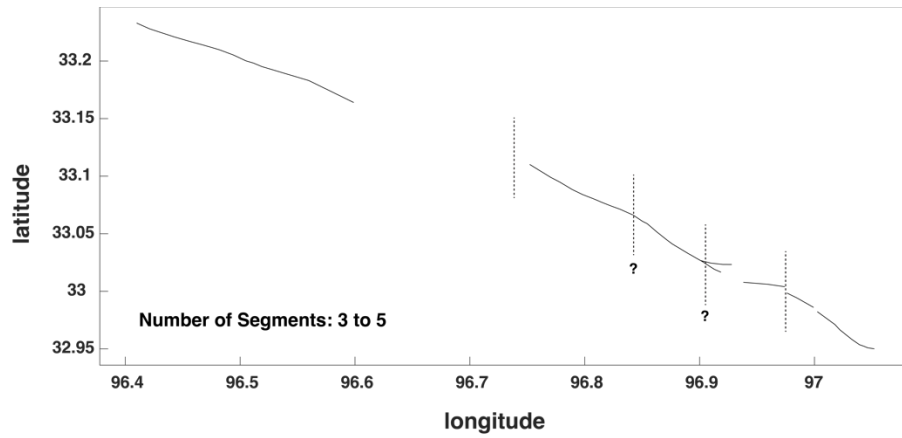


Figure S17. Surface rupture and segmentation results for the Yushu earthquake.

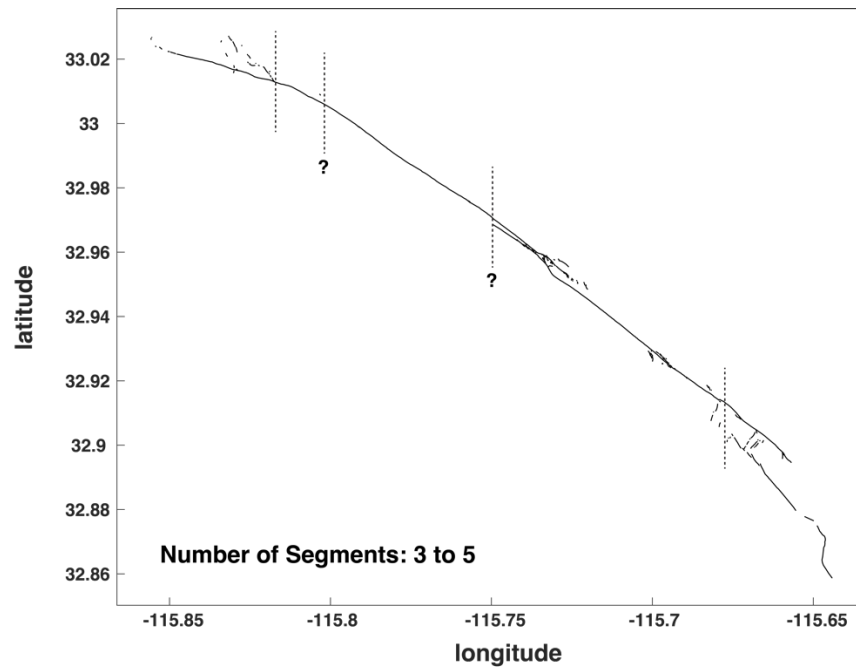


Figure S18. Surface rupture and segmentation results for the Superstition Hills earthquake.

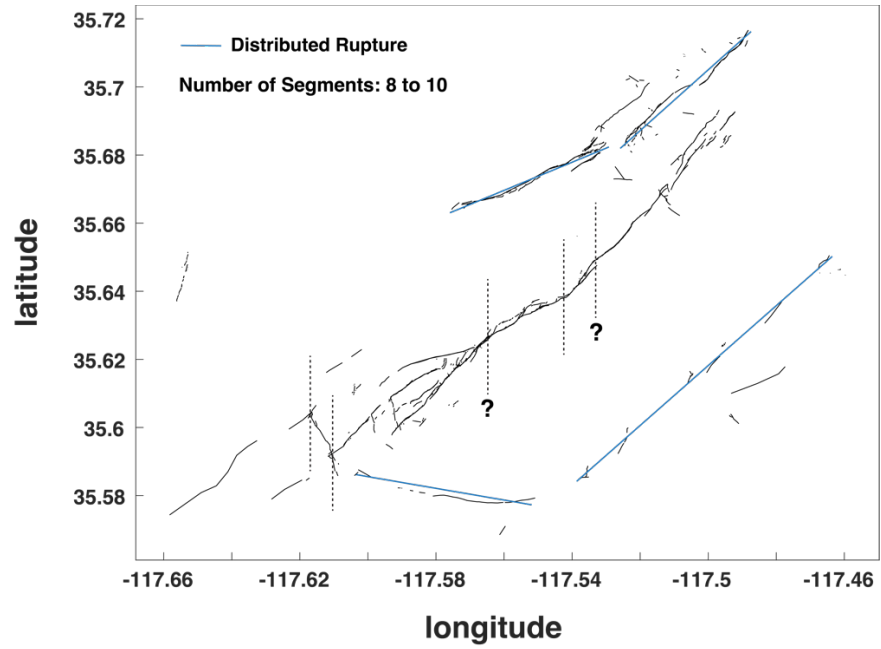


Figure 19. Surface rupture and segmentation results for the Ridgecrest foreshock.

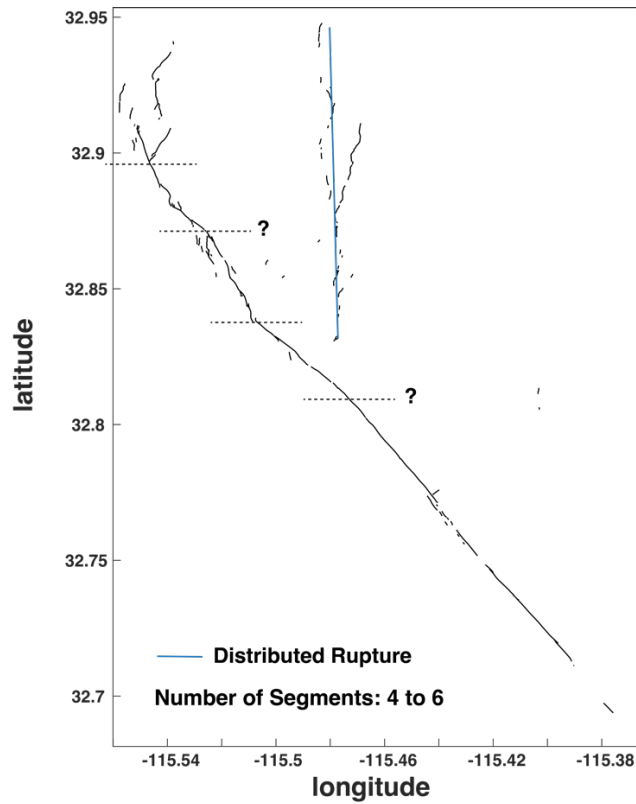


Figure S20. Surface rupture and segmentation results for the Imperial Valley earthquake.

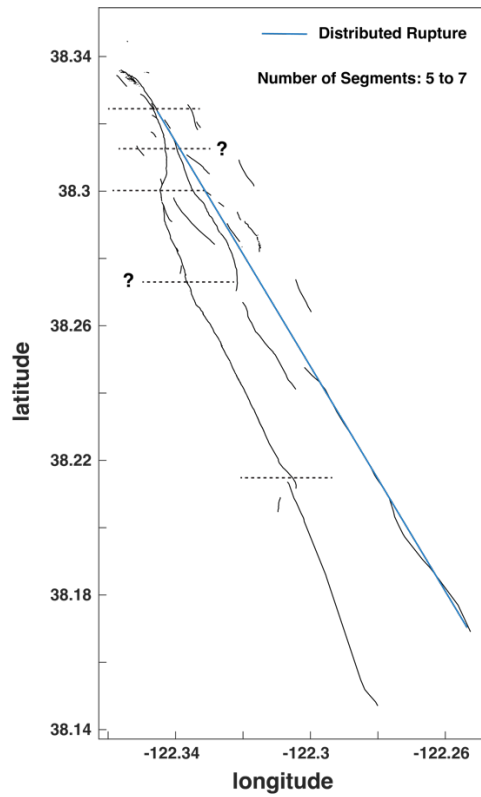


Figure S21. Surface rupture and segmentation results for the Napa earthquake.

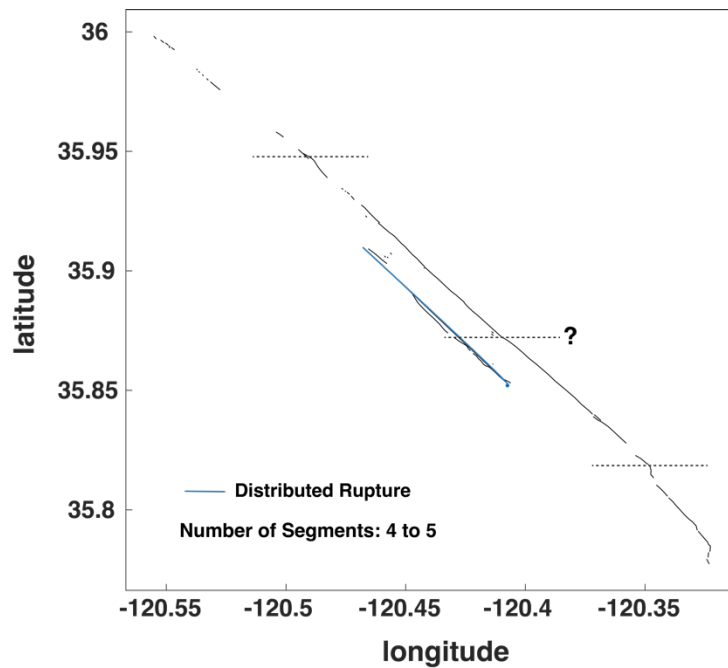


Figure S22. Surface rupture and segmentation results for the Parkfield earthquake.

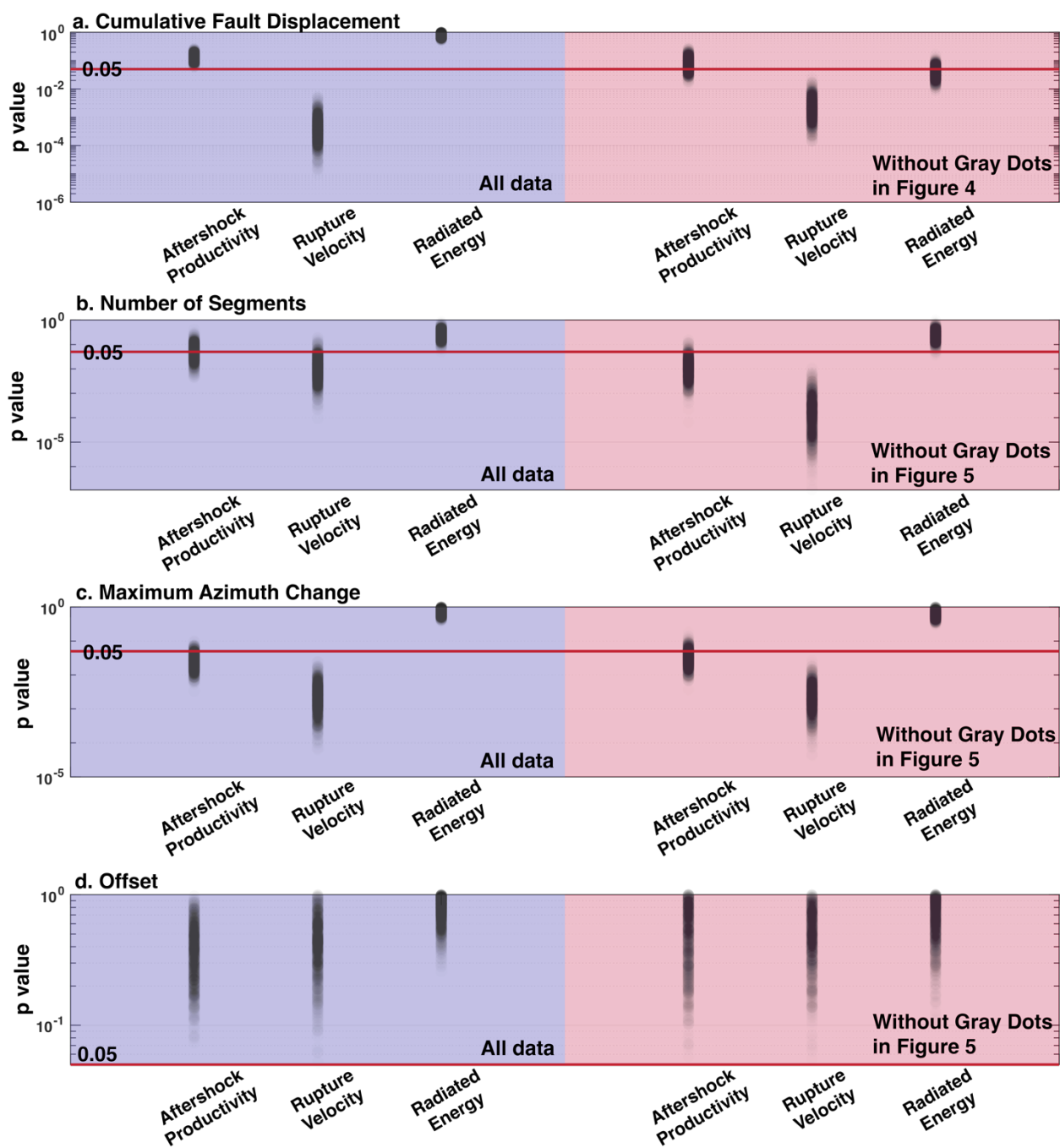


Figure S23. The P-value distributions for bootstrapped comparisons of seismic parameters and a) cumulative fault displacement, b) number of rupture segments, c) maximum change in azimuth between surface rupture traces, and d) steeper offsets between segments.

Supporting Information References

Akbayram, K., Sorlien, C. C., & Okay, A. I. (2016). Evidence for a minimum 52 ± 1 km of total offset along the northern branch of the North Anatolian Fault in northwest Turkey.

Tectonophysics, 668–669, 35–41. <https://doi.org/10.1016/j.tecto.2015.11.026>

Ansari, S. (2021). Structural and stress heterogeneities along the 1997 Zirkuh earthquake fault, Eastern Iran. *Bulletin of Engineering Geology and the Environment*, 80(11), 8319–8337.

<https://doi.org/10.1007/s10064-021-02436-7>

Arefiev, S., Rogozhin, E., Tatevossian, R., Rivera, L., & Cisternas, A. (2000). The Neftegorsk (Sakhalin Island) 1995 earthquake: A rare interplate event. *Geophysical Journal International*, 143(3), 595–607. <https://doi.org/10.1046/j.1365-246X.2000.00234.x>

Avouac, J.-P., Ayoub, F., Wei, S., Ampuero, J.-P., Meng, L., Leprince, S., Jolivet, R., Duputel, Z., & Helmberger, D. (2014). The 2013, M_w 7.7 Balochistan earthquake, energetic strike-slip reactivation of a thrust fault. *Earth and Planetary Science Letters*, 391, 128–134.

<https://doi.org/10.1016/j.epsl.2014.01.036>

Barnhart, W. D., Briggs, R. W., Reitman, N. G., Gold, R. D., & Hayes, G. P. (2015). Evidence for slip partitioning and bimodal slip behavior on a single fault: Surface slip characteristics of the 2013 M_w 7.7 Balochistan, Pakistan earthquake. *Earth and Planetary Science Letters*, 420, 1–11.

<https://doi.org/10.1016/j.epsl.2015.03.027>

Barrier, E., Huchon, P., & Aurelio, M. (1991). Philippine fault: A key for Philippine kinematics. *Geology*, 19(1), 32–35. [https://doi.org/10.1130/0091-7613\(1991\)019<0032:PFAKFP>2.3.CO;2](https://doi.org/10.1130/0091-7613(1991)019<0032:PFAKFP>2.3.CO;2)

Calais, E., Freed, A., Mattioli, G., Amelung, F., Jónsson, S., Jansma, P., Hong, S.-H., Dixon, T., Prépetit, C., & Momplaisir, R. (2010). Transpressional rupture of an unmapped fault during the 2010 Haiti earthquake. *Nature Geoscience*, 3(11), Article 11. <https://doi.org/10.1038/ngeo992>

Çetin, K. Ö., İlgaç, M., Can, G., Çakır, E., & Söylemez, B. (2020). *Preliminary Report on Engineering and Geological Effects of the January 24, 2020 Magnitude 6.7 Earthquake in Elazığ, Turkey*. GEER. <https://open.metu.edu.tr/handle/11511/95146>

Der Woerd, J. V., Tapponnier, P., J. Ryerson, F., Meriaux, A.-S., Meyer, B., Gaudemer, Y., Finkel, R. C., Caffee, M. W., Guoguan, Z., & Zhiqin, X. (2002). Uniform postglacial slip-rate along the central 600 km of the Kunlun Fault (Tibet), from ^{26}Al , ^{10}Be , and ^{14}C dating of riser offsets, and climatic origin of the regional morphology. *Geophysical Journal International*, 148(3), 356–388. <https://doi.org/10.1046/j.1365-246x.2002.01556.x>

Duman, T. Y., Emre, O., Dogan, A., & Ozalp, S. (2005). Step-over and bend structures along the 1999 Duzce earthquake surface rupture, North Anatolian Fault, Turkey. *Bulletin of the Seismological Society of America*, 95(4), 1250–1262. <https://doi.org/10.1785/0120040082>

Elliott, A., Elliott, J., Hollingsworth, J., Kulikova, G., Parsons, B., & Walker, R. (2020). Satellite imaging of the 2015 $M7.2$ earthquake in the Central Pamir, Tajikistan, elucidates a sequence of

shallow strike-slip ruptures of the Sarez-Karakul fault. *Geophysical Journal International*, 221(3), 1696–1718. <https://doi.org/10.1093/gji/ggaa090>

Fialko, Y., Sandwell, D., Simons, M., & Rosen, P. (2005). Three-dimensional deformation caused by the Bam, Iran, earthquake and the origin of shallow slip deficit. *Nature*, 435(7040), Article 7040. <https://doi.org/10.1038/nature03425>

Fu, B., Awata, Y., Du, J., Ninomiya, Y., & He, W. (2005). Complex geometry and segmentation of the surface rupture associated with the 14 November 2001 great Kunlun earthquake, northern Tibet, China. *Tectonophysics*, 407(1), 43–63. <https://doi.org/10.1016/j.tecto.2005.07.002>

Haeussler, P. J., Schwartz, D. P., Dawson, T. E., Stenner, H. D., Lienkaemper, J. J., Sherrod, B., Cinti, F. R., Montone, P., Craw, P. A., Crone, A. J., & Personius, S. F. (2004). Surface Rupture and Slip Distribution of the Denali and Totschunda Faults in the 3 November 2002 $M 7.9$ Earthquake, Alaska. *Bulletin of the Seismological Society of America*, 94(6B), S23–S52. <https://doi.org/10.1785/0120040626>

Jachens, R. C., Langenheim, V. E., & Matti, J. C. (2002). Relationship of the 1999 Hector Mine and 1992 Landers fault ruptures to offsets on Neogene faults and distribution of Late Cenozoic Basins in the Eastern California Shear Zone. *Bulletin of the Seismological Society of America*, 92(4), 1592–1605. <https://doi.org/10.1785/0120000915>

Klinger, Y. (2010). Relation between continental strike-slip earthquake segmentation and thickness of the crust. *Journal of Geophysical Research: Solid Earth*, 115(B7). <https://doi.org/10.1029/2009JB006550>

Langridge, R. M., Stenner, H. D., Fumal, T. E., Christofferson, S. A., Rockwell, T. K., Hartleb, R. D., Bachhuber, J., & Barka, A. A. (2002). Geometry, slip distribution, and kinematics of surface rupture on the Sakarya Fault segment during the 17 August 1999 İzmit, Turkey, Earthquake. *Bulletin of the Seismological Society of America*, 92(1), 107–125. <https://doi.org/10.1785/0120000804>

Li, C., Pang, J., & Zhang, Z. (2012). Characteristics, geometry, and segmentation of the surface rupture associated with the 14 April 2010 Yushu Earthquake, Eastern Tibet, China. *Bulletin of the Seismological Society of America*, 102(4), 1618–1638. <https://doi.org/10.1785/0120110261>

Lindsey, E. O., & Fialko, Y. (2016). Geodetic constraints on frictional properties and earthquake hazard in the Imperial Valley, Southern California. *Journal of Geophysical Research: Solid Earth*, 121(2), 1097–1113. <https://doi.org/10.1002/2015JB012516>

Maleki Asayesh, B., Zafarani, H., & Tatar, M. (2020). Coulomb stress changes and secondary stress triggering during the 2003 ($M_W 6.6$) Bam (Iran) earthquake. *Tectonophysics*, 775, 228304. <https://doi.org/10.1016/j.tecto.2019.228304>

Marchandon, M., Vergnolle, M., Sudhaus, H., & Cavalié, O. (2018). Fault geometry and slip distribution at depth of the 1997 $M_W 7.2$ Zirkuh Earthquake: Contribution of near-field displacement data. *Journal of Geophysical Research: Solid Earth*, 123(2), 1904–1924. <https://doi.org/10.1002/2017JB014703>

Natawidjaja, D. H., Daryono, M. R., Prasetya, G., Udrek, Liu, P. L.-F., Hananto, N. D., Kongko, W., Triyoso, W., Puji, A. R., Meilano, I., Gunawan, E., Supendi, P., Pamumpuni, A., Irsyam, M., Faizal, L., Hidayati, S., Sapiie, B., Kusuma, M. A., & Tawil, S. (2021). The 2018 M_w 7.5 Palu ‘supershear’ earthquake ruptures geological fault’s multisegment separated by large bends: Results from integrating field measurements, LiDAR, swath bathymetry and seismic-reflection data. *Geophysical Journal International*, 224(2), 985–1002. <https://doi.org/10.1093/gji/ggaa498>

Nicol, A., Khajavi, N., Pettinga, J. R., Fenton, C., Stahl, T., Bannister, S., Pedley, K., Hyland-Brook, N., Bushell, T., Hamling, I., Ristau, J., Noble, D., & McColl, S. T. (2018). Preliminary Geometry, displacement, and kinematics of fault ruptures in the epicentral region of the 2016 M_w 7.8 Kaikōura, New Zealand, earthquake. *Bulletin of the Seismological Society of America*, 108(3B), 1521–1539. <https://doi.org/10.1785/0120170329>

Okuwaki, R., & Fan, W. (2022). Oblique convergence causes both thrust and strike-slip ruptures during the 2021 M 7.2 Haiti earthquake. *Geophysical Research Letters*, 49(2), e2021GL096373. <https://doi.org/10.1029/2021GL096373>

Powers, P. M., & Jordan, T. H. (2010). Distribution of seismicity across strike-slip faults in California. *Journal of Geophysical Research: Solid Earth*, 115(B5). <https://doi.org/10.1029/2008JB006234>

Quigley, M. C., Jiménez, A., Duffy, B., & King, T. R. (2019). Physical and statistical behavior of multifault earthquakes: Darfield earthquake case study, New Zealand. *Journal of Geophysical Research: Solid Earth*, 124(5), 4788–4810. <https://doi.org/10.1029/2019JB017508>

Quigley, M., Dissen, R. V., Litchfield, N., Villamor, P., Duffy, B., Barrell, D., Furlong, K., Stahl, T., Bilderback, E., & Noble, D. (2012). Surface rupture during the 2010 M_w 7.1 Darfield (Canterbury) earthquake: Implications for fault rupture dynamics and seismic-hazard analysis. *Geology*, 40(1), 55–58. <https://doi.org/10.1130/G32528.1>

Ren, J., Xu, X., Zhang, G., Wang, Q., Zhang, Z., Gai, H., & Kang, W. (2022). Coseismic surface ruptures, slip distribution, and 3D seismogenic fault for the 2021 M_w 7.3 Maduo earthquake, central Tibetan Plateau, and its tectonic implications. *Tectonophysics*, 827, 229275. <https://doi.org/10.1016/j.tecto.2022.229275>

Sangha, S., Peltzer, G., Zhang, A., Meng, L., Liang, C., Lundgren, P., & Fielding, E. (2017). Fault geometry of 2015, M_w 7.2 Murghab, Tajikistan earthquake controls rupture propagation: Insights from InSAR and seismological data. *Earth and Planetary Science Letters*, 462, 132–141. <https://doi.org/10.1016/j.epsl.2017.01.018>

Schmidt, J., Hacker, B. R., Ratschbacher, L., Stübner, K., Stearns, M., Kylander-Clark, A., Cottle, J. M., Alexander, A., Webb, G., Gehrels, G., & Minaev, V. (2011). Cenozoic deep crust in the Pamir. *Earth and Planetary Science Letters*, 312(3), 411–421. <https://doi.org/10.1016/j.epsl.2011.10.034>

Scott, C., Champenois, J., Klinger, Y., Nissen, E., Maruyama, T., Chiba, T., & Arrowsmith, R. (2019). The 2016 M 7 Kumamoto, Japan, earthquake slip field derived from a joint inversion of

differential Lidar topography, optical correlation, and InSAR surface displacements. *Geophysical Research Letters*, 46(12), 6341–6351. <https://doi.org/10.1029/2019GL082202>

Socquet, A., Hollingsworth, J., Pathier, E., & Bouchon, M. (2019). Evidence of supershear during the 2018 magnitude 7.5 Palu earthquake from space geodesy. *Nature Geoscience*, 12(3), Article 3. <https://doi.org/10.1038/s41561-018-0296-0>

Stirling, M. W., Wesnousky, S. G., & Shimazaki, K. (1996). Fault trace complexity, cumulative slip, and the shape of the magnitude-frequency distribution for strike-slip faults: A global survey. *Geophysical Journal International*, 124(3), 833–868. <https://doi.org/10.1111/j.1365-246X.1996.tb05641.x>

Sunal, G., & Erturaç, M. K. (2012). Estimation of the pre-North Anatolian Fault Zone pseudo-paleo-topography: A key to determining the cumulative offset of major post-collisional strike-slip faults. *Geomorphology*, 159–160, 125–141. <https://doi.org/10.1016/j.geomorph.2012.03.013>

Treiman, J. A., Kendrick, K. J., Bryant, W. A., Rockwell, T. K., & McGill, S. F. (2002). Primary surface rupture associated with the M_W 7.1 16 October 1999 Hector Mine earthquake, San Bernardino County, California. *Bulletin of the Seismological Society of America*, 92(4), 1171–1191. <https://doi.org/10.1785/0120000923>

Valdiya, K. S., & Sanwal, J. (2017). Chapter 4—Mountain arcs and festoons in Pakistan. In K. S. Valdiya & J. Sanwal (Eds.), *Developments in Earth Surface Processes* (Vol. 22, pp. 111–137). Elsevier. <https://doi.org/10.1016/B978-0-444-63971-4.00004-9>

Walker, R., & Jackson, J. (2004). Active tectonics and late Cenozoic strain distribution in central and eastern Iran. *Tectonics*, 23(5). <https://doi.org/10.1029/2003TC001529>

Wang, Y., Lin, Y. N., Simons, M., & Tun, S. T. (2014). Shallow rupture of the 2011 Tarlay earthquake (M_W 6.8), Eastern Myanmar. *Bulletin of the Seismological Society of America*, 104(6), 2904–2914. <https://doi.org/10.1785/0120120364>

Yuan, Z., Li, T., Su, P., Sun, H., Ha, G., Guo, P., Chen, G., & Thompson Jobe, J. (2022). Large surface-rupture gaps and low surface fault slip of the 2021 M_W 7.4 Maduo earthquake along a low-activity strike-slip fault, Tibetan Plateau. *Geophysical Research Letters*, 49(6), e2021GL096874. <https://doi.org/10.1029/2021GL096874>

Yue, H., Shen, Z.-K., Zhao, Z., Wang, T., Cao, B., Li, Z., Bao, X., Zhao, L., Song, X., Ge, Z., Ren, C., Lu, W., Zhang, Y., Liu-Zeng, J., Wang, M., Huang, Q., Zhou, S., & Xue, L. (2022). Rupture process of the 2021 $M7.4$ Maduo earthquake and implication for deformation mode of the Songpan-Ganzi terrane in Tibetan Plateau. *Proceedings of the National Academy of Sciences*, 119(23), e2116445119. <https://doi.org/10.1073/pnas.2116445119>

Zinke, R., Hollingsworth, J., & Dolan, J. F. (2014). Surface slip and off-fault deformation patterns in the 2013 M_W 7.7 Balochistan, Pakistan earthquake: Implications for controls on the distribution of near-surface coseismic slip. *Geochemistry, Geophysics, Geosystems*, 15(12), 5034–5050. <https://doi.org/10.1002/2014GC005538>